ISSN 2149-2123

JOURNAL OF SCIENCE & ENGINEERING HITTITE

Volume 2, Issue 1, 2015

www.hjse.hitit.edu.tr

HJSE Official Journal of Graduate School of Natural & Applied Sciences, Hitit University www.hjse.hitit.edu.tr

Ultrasonic Treatment of Biologically Treated Baker's Yeast Effluent

59-63

by Emine Yilmaz

The effect of the amount of catalyst on color and COD removal was investigated. According to results, by using ultrasound and TiO_2/ZnO composite, decolorization increases until the optimum of the catalyst amount. The highest decolorization was obtained at 0.15 g/L of catalyst concentration.

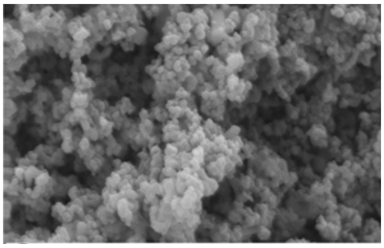

Hillock Formation by Surface Drift-Diffusion Driven by the Gradient of Elastic Dipole Interaction Energy Under Compressive Stresses in Bi-Crystalline Thin Films

65-76

by Tarik Omer Ogurtani

This analysis implies that the ridge growth stage is not controlled by Ziegler's 'maximum entropy production principle' but rather Prigogine's 'minimum entropy production hypothesis' for the stationary non-equilibrium states in complex systems.

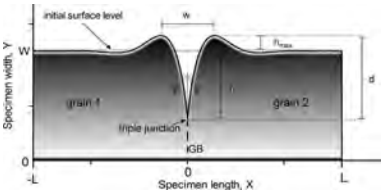

Recent Tectonic Features of the Central Part (Bolu-Corum) of the North Anatolian Fault

77-83

by Hakan Yavasoglu

The rate of conversion and how it varies along strike are not known due to the sparsely distributed GPS benchmarks in the region. At the same time, the aseismic fault creep determined using InSAR has needed to proof and improve by other techniques and tools. For this propose the new project has been started to determine quantitatively the rate of convergence and its variation along segment of the NAF between Bolu and Çorum.

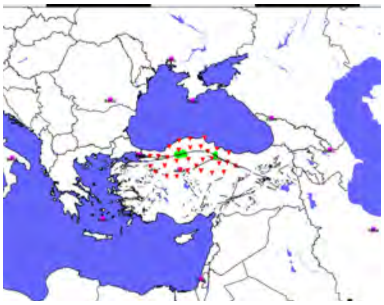

A New Generation, Promising Engineering Material: Cubic Boron Nitride (c-BN)

85-90

by Baris Cetin

In this context, cubic boron nitride (c-BN), which is a special polymorph of boron nitride, seems to be a high-potential candidate for engineering solutions due to its great mechanical and chemical properties. In this article, advantages and disadvantages of c-BN material system are presented with respect to our ongoing research efforts.

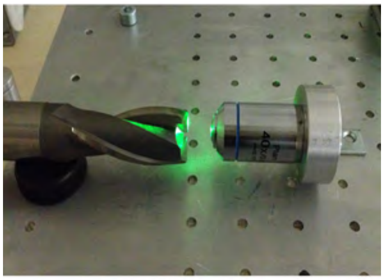

Synthesis, Spectroscopic and Thermal Characterization of Non-Metal Cation (NMC) Pentaborates Salts Containing 2-amino-5-nitropyridine and 2-amino-6-methylpyridine as Cation

91-96

by Ümit Sizir

The trigonal (BO_3) and tetragonal (BO_4^-) moities were determined in ^{11}B NMR spectrums. According to P-XRD methods each of the compound structures are in crystalline form. The peaks of pentaborate anion $[B_5O_6(OH)_4]^-$ were seen in FT-IR spectra.

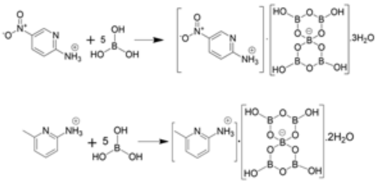

Monitoring of Waste Gasification Products: Solid, Liquid and Syngas

97-102

by Atakan Ongen

In this study, biomass and waste gasification efficiencies were investigated in a lab-scale fixed bed reactor by the use of cyclone separator. Solid, liquid and gas products were monitored both during and after the completion of the process.

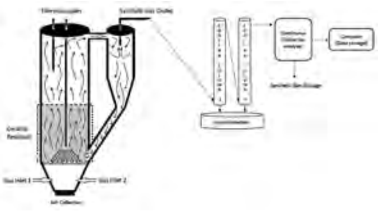

Improving Fundamental Values and Environmental Awareness in Sustainable Engineering Education through Laboratory and Design Experiments

103-114

by Nihan Kaya

It is of the essence of this paper to attach importance to enabling prospective engineers to learn about simple and plain techniques and technologies of the past, while learning about the most up-to-date ones. .

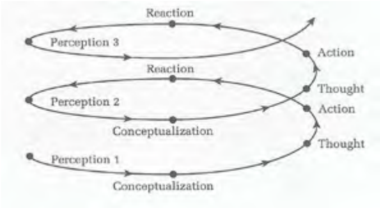

A Second Degree Newton Method for an Inverse Scattering Problem for a Dielectric Cylinder

115-125

by Ahmet Altundag

The inverse obstacle scattering problem we are interested is to reconstruct the image of an infinitely long homogeneous dielectric cylinder from the far field pattern for scattering of a time-harmonic E-polarized electromagnetic plane wave.

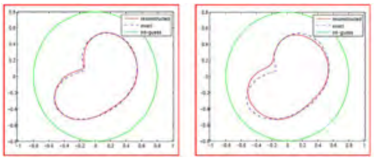

Owner
Prof. Dr. Reha Metin ALKAN
on behalf of Hitit University

Editor-in-chief
Prof. Dr. Ali Kılıçarslan

Associate Editors
Assoc. Prof. Dr. D.Ali Köse
Asst. Prof. Dr. Öncü Akyıldız

Production
Dr. Kazım Köse

Editor’s Office
Tel: +90 364 227 45 33 / 12 36
Fax: +90 364 227 45 35
Email: alikilicarslan@hitit.edu.tr

Subscription Service:
Tel: +90 364 227 45 33 / 12 82
Fax: +90 364 227 45 35
Email: hjse@hitit.edu.tr

EDITORIAL BOARD

Dr. Mike Beckett	Bangor University, Bangor, UK.
Dr. İbrahim Dinçer	Uoit Ontario University, Ontario, Canada.
Dr. Mohamad S. Quato	Central Michigan University, Michigan, USA.
Dr. Saffa Riffat	University of Nottingham, UK.
Dr. Thanos Salifoglou	Aristotle University of Thessaloniki, Thessaloniki, Greece.
Dr. Wojciech Nogala	Polish Academy of Sciences, Poland
Dr. Yusuf Ayvaz	Süleyman Demirel University, Isparta, Turkey.
Dr. Adil Denizli	Hacettepe University, Ankara, Turkey.
Dr. Ali Gencer	Ankara University, Ankara, Turkey.
Dr. Metin Gürü	Gazi University, Ankara, Turkey.
Dr. Murat Hoşöz	Kocaeli University, Kocaeli, Turkey.
Dr. Sadık Kakaç	TOBB University of Economics and Technology, Ankara, Turkey
Dr. Tarık Ömer Oğurtanı	Middle East Technical University, Ankara, Turkey
Dr. Ender Suvacı	Anadolu University, Eskişehir, Turkey
Dr. Ali Topçu	Hacettepe University, Ankara, Turkey
Dr. Ali Kılıçarslan	Hitit University, Çorum, Turkey
Dr. Satılmış Basan	Hitit University, Çorum, Turkey
Dr. Vedat Deniz	Hitit University, Çorum, Turkey
Dr. Aydın Özlük	Hitit University, Çorum, Turkey
Dr. Menderes Suiçmez	Hitit University, Çorum, Turkey
Dr. Seçil Şatır	Hitit University, Çorum, Turkey
Dr. Abdurrahman Asan	Hitit University, Çorum, Turkey
Dr. Kazım Savaş Bahçeci	Hitit University, Çorum, Turkey
Dr. Naki Çolak	Hitit University, Çorum, Turkey
Dr. Faruk Gökmeşe	Hitit University, Çorum, Turkey
Dr. Hakan Güngüneş	Hitit University, Çorum, Turkey
Dr. Bülent Kabak	Hitit University, Çorum, Turkey
Dr. Dursun Ali Köse	Hitit University, Çorum, Turkey
Dr. İrfan Kurtbaş	Hitit University, Çorum, Turkey
Dr. Uğur Adnan Sevil	Hitit University, Çorum, Turkey
Dr. İbrahim Sönmez	Hitit University, Çorum, Turkey
Dr. Fatma Muazzez Şimşir	Hitit University, Çorum, Turkey
Dr. Dilber Esra Yıldız	Hitit University, Çorum, Turkey

Journal Name : HITTITE JOURNAL OF SCIENCE AND ENGINEERING
Year : 2014
Managing Editor : Prof. Dr. Ali KILIÇARSLAN
Managing Office : Hitit University Graduate School of Natural and Applied Sciences
Managing Office Tel : +90 364 666 11 11
Publication Language : English
Publication Type : International Article
Delivery Format : 2 times a year (semi-annually)
Print ISSN : 2149-2123
Publisher : Bir Medya
Publisher Address : Yeniyol Mah. Gazi 12. Sok. No:9/13 ÇORUM
Publisher Tel : +90 364 225 66 64

I am excited to announce the new issue of Hittite Journal of Science and Engineering (HJSE) which started to publish in December 2014. As we mention earlier in the previous issue, our ultimate goal is to provide a medium for the exchange and dissemination of new ideas, technological developments and research results as an abstracted and indexed journal. We believe that we are one step closer to this goal with this issue.

The issue contains eight manuscripts from the disciplines of chemistry, applied mathematics, materials science and engineering, chemical engineering, geomatics engineering, and environmental engineering. These manuscripts was first screened by Section Editors using plagiarism prevention software and then reviewed and corrected according to the reviewer's comments. I would like to express my gratitude to all our authors and contributing reviewers.

Meantime we set our policies of retraction and correction. Accordingly, HJSE will publish corrections for errors, made by the journal or authors, of a scientific nature that do not alter the overall basic results or conclusions of a published article. HJSE articles may be retracted by their authors or by the editor because of pervasive error or unsubstantiated or irreproducible data. Articles may be retracted, for example, because of honest error, scientific misconduct, or plagiarism. Errata are published at the discretion of the editors and appear as formal notices in the journal.

I would like to thank to the President of Hitit University, Prof. Dr. Reha Metin Alkan, for his constant interest in HJSE and also to the Associate Editors of HJSE, namely Dr. Dursun Ali Kose and Dr. Oncu Akyildiz, as well as our Production Editor, Dr. Kazim Kose for their invaluable efforts in making of the journal.

I invite the researchers and scientists from all branches of science and engineering to join us by sending their best papers for publication in Hittite Journal of Science and Engineering.

Dr. Ali Kılıçarslan

Editor-in-Chief

Director of Graduate School of Natural and Applied Sciences of Hitit University

Hittite Journal of Science and Engineering, 2015, 2 (1) 59-63
ISSN NUMBER: 2149-2123
DOI: 10.17350/HJSE19030000009

Ultrasonic Treatment of Biologically Treated Baker's Yeast Effluent

Emine Yilmaz and Serap Findik
Hitit University, Department of Chemical Engineering, Corum, TURKEY

Article History:
Received: 2015/01/04
Accepted: 2015/05/08
Online: 2015/07/01

***Correspondence to**: Serap Fındık,*
Hitit University, Faculty of Engineering,
Department of Chemical Engineering,
Corum, Turkey
Tel: +90 (364) 227-4533
Fax: +90 (364) 227-4535
E-Mail: serapfindik@hitit.edu.tr

ABSTRACT

The aim of this study was to examine the removal of color and chemical oxygen demand (COD) of biologically treated baker's yeast effluent with ultrasonic irradiation. An ultrasonic homogenizator with 20 kHz frequency was used for this purpose. TiO_2/ZnO composite was used as a sonocatalyst. The effect of the amount of catalyst on color and COD removal was investigated. According to results, by using ultrasound and TiO_2/ZnO composite, decolorization increases until the optimum of the catalyst amount. The highest decolorization was obtained at 0.15 g/L of catalyst concentration. COD removal was 17% with ultrasonic irradiation and increased to 33% when using ultrasound along with the catalyst at the optimum amount. The effect of the solution pH on ultrasonic decolorization was also investigated in this study.

Key Words:
Baker's Yeast Effluent; Decolarization; Sonocatalyst; Ultrasonic Irradiation.

INTRODUCTION

Melanoidins are dark brown to black colored natural condensation products of sugar and amino acids produced by non-enzymatic browning reactions called Maillard reactions. Naturally melanoidins are widely distributed in food, drinks and widely discharged in huge amount by various agro-based industries especially from cane molasses based distilleries and fermentation industries as environmental pollutants [1].

Wastewater containing molasses has high chemical oxygen demand (COD) and biochemical oxygen demand (BOD), producing a strong odor and a dark brown color. If these wastewaters are discharged to water sources, the dissolved oxygen level decreases. Dark colors prevent sunlight penetration so, the photosynthesis activity decreases [2].

Biological treatment methods of a combination of anaerobic and aerobic processes are normally effective in removing the high organic load from molasses wastewater. However, degradation of melanoidins is about 6% to 7% after biological treatment so wastewater has still color [3]. Melanoidins have antioxidant properties which render them recalcitrant to biodegradation [4]. This means that there is strong resistance to microbiological degradation. To improve the efficiency of the biological treatment, other treatment methods such as adsorption [1], ozonation [3] coagulation [4] and sonolysis [1] can be used as a pre-treatment or a post treatment step.

Sonolysis or sonochemical process uses ultrasound waves in the range of 20-1000 kHz. Ultrasound is transmitted throughout an aqueous solution to create acoustic cavitation. Micro-sized bubbles readily form, grow and subsequently collapse in split seconds, releasing extremely large magnitude of energy. Because of this energized water decomposes into hydrogen atoms and hydroxyl (•OH) radicals [5]. Sonochemical reactions can occur in three different regions: in the interior of the collapsing bubbles, at the interfacial region being the thin shell of fluid surrounding the collapsing cavitation bubble, and in the bulk solution [6].

However, in actual applications, the efficiency of using ultrasound alone to degrade organic compounds is relatively low. Many recent studies have been focused on the ultrasonic irradiation in combination with photocatalyst [7-12]. Most of studies on sonocatalytic degradation of water pollutant are made using TiO_2 and ZnO catalyst mainly due to its wide availability, stability of the chemical structure, non-toxicity and reactivity, optical and electrical properties. TiO_2 and ZnO have the fast recombination rate of electron and whole pairs and they can only absorb the ultraviolet light because of the relative broad band-gap. Therefore, to improve catalyst performance, the electron hole pair recombination must be strained [8, 11, 12].

Biologically treated baker's yeast effluent was used in this study. This treated wastewater meets environmental regulations, but its limitations in the treated wastewater may change and strong restrictions can be performed to protect environment. For this reason, an integrated treatment process can be used to improve existing properties of treated wastewater. In this study, sonolysis was used as a post-treatment step for biologically treated baker's yeast effluent. In the previous literature ultrasound was used as a pre-treatment step for the treatment of molasses wastewater [13-15]. However, no study on sonocatalytic treatment of biologically treated baker's yeast effluent was previously reported.

The purpose of this study is to remove color and COD from the biologically treated baker's yeast effluent using ultrasound. TiO_2/ZnO composite has been used as sonocatalyst. The effect of catalyst amount of removal of color and COD was investigated for biologically treated baker's yeast effluent. The effect of pH on decolorization was also investigated.

MATERIALS AND METHODS

Materials

Biologically treated baker's yeast effluent was obtained from Baker's yeast factory located in the North of Turkey. The wastewater was collected after anaerobic-aerobic treatment plants and kept in a refrigerator at 4°C. The characteristics of the biologically treated wastewater used in this study are given in Table 1. TiO_2 and ZnO were supplied from Merck. To investigate the pH effect on ultrasonic irradiation, the pH of the wastewater was adjusted by using NaOH and HCl.

Apparatus

Ultrasonic irradiation was introduced using a probe type processor. It was supplied from Bandelin (HD2200). Its operating frequency is 20 kHz and power is 200 W. An ultrasonic bath (DSA50-SK) with 42 kHz frequency and 1600 mL volume was used for the preparation of catalyst. A spectrophotometer of Hach-Lange DR2400 was used to measure COD and absorbance. COD measurement was done by using COD tubes with 0-1500 ppm concentration.

Table 1. Characterization of biologically treated baker's yeast wastewater

Parameter	*Value*
Color	*100-200 Pt-Co*
pH	*6.5-8.0*
COD	*50-100 mg/L*

Catalyst Preparation

For the preparation of TiO_2/ZnO catalyst, 4 mole TiO_2 and 1 mole ZnO were mixed, and then distilled water was added until wet the surface of the mixture. The mixture was sonicated in an ultrasonic bath for 6 min. in order to improve dispersion of TiO_2 and ZnO. After completion of mixing, the mixture was dried at 100°C for 10h and calcined at 700°C for 60 min. [16, 17].

Procedure

A schematic diagram of the ultrasonic reaction system is given in Figure 1. Biologically treated wastewater was filtered before use. The reactor used in this study was a cylindrical glass vessel with 500 mL volume. This reactor was filled with 500 mL biologically treated wastewater and TiO_2/ZnO catalyst was added. Then an ultrasonic probe was inserted into the reactor. The distance from the probe to the bottom of the reactor was 3 cm. The power of the ultrasonic probe was adjusted to 80 W and the pulsed cycle at 30%. Then the wastewater was irradiated by ultrasound for 60 min. The samples were withdrawn from the reaction mixture periodically and the centrifuge operated at 4000 rpm for 10 min. was used to remove any suspended particles and catalyst. After that, the absorbance and the COD of the sample was recorded using a spectrophotometer. Absorbance measurement was made at a wavelength of 400 nm. The absorbance of the effluent was evaluated to calculate decolorization.

The reaction was performed at an uncontrolled temperature. This means that there was no external cooling mechanism to control the bulk solution temperature in the reactor. Due to dissipation of ultrasonic energy in the liquid, temperature of the reaction mixture may increase gradually as the ultrasonic irradiation time increases. Experiments started at ambient temperature about 20°C

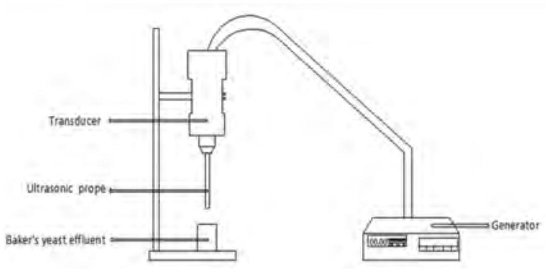

Figure 1. Schematic diagram of the ultrasonic reaction system

and reached to 40°C at the end of 1 hour. Similar results have been reported in literature for ultrasonic treatment of distillery wastewater [13, 14]. Yilmaz [18] has obtained the highest decolorization at uncontrolled temperature for ultrasonic treatment of baker's yeast effluent.

RESULTS AND DISCUSSIONS

Effect of pH on ultrasonic decolorization of biologically treated baker's yeast effluent

The pH of wastewater plays an important role in the degradation of organic pollutants by sonolysis. The pH of the biologically treated baker's yeast wastewater used in this study was 7.4. To investigate the pH effect on ultrasonic irradiation, the pH of the wastewater was adjusted to 5.3 and 9. Figure 2 shows the effect of pH on ultrasonic decolorization of biologically treated wastewater. As shown from Figure 2 there was no response at 5.3 and 7.4 pH value. The 8.6% decolorization was obtained at the end of one hour when the pH of the solution was 9.

In the case of molecules with ionisable functional groups, the rate of degradation under ultrasonic irradiation would be affected by the solution pH in view of the fact that negative charges exist near the periphery of cavitational bubbles. In addition, the gas-bubble interfaces are highly hydrophobic and the ionic state of contaminants may affect their tendency to partition into this hydrophobic region. Hydrophilic compounds are oxidized by the •OH radicals in bulk solution and/or at the interface of liquid gas bubbles depending on the substrate concentration. Hydrophobic compounds are destroyed by pyrolysis in the bubble [19]. The properties of intermediate products may determine the effect of pH on ultrasonic decolorization of biologically treated wastewater.

SEM and surface analysis of TiO_2/ZnO composite

In this study, a TiO_2/ZnO composite with 4:1 molar ratio was used. It was calcined at 700°C for 60 min. The typical SEM image of TiO_2/ZnO is shown in Figure 3. As shown in Figure 3, the composite consists of spherical particles, many mesopores and particles aggregated to form larger particles. Table 2 shows the results of surface analysis.

Effect of TiO_2/ZnO composite amount on ultrasonic decolorization of biologically treated baker's yeast effluent

There was no decolorization by using only ultrasound at the original pH value of the baker's yeast effluent. To ensure sonolytic degradation of organic compounds, TiO_2/ZnO composite was prepared. The molar ratio of the TiO_2/ZnO composite was 4:1 and calcined at 700°C for 60 min. The presence of a catalyst can enhance the dissociation reaction of H_2O molecules to increase the number of free radicals generated, thereby increases the number of free radicals [20].

Table 2. Surface analysis of prepared composite TiO_2/ZnO

Calcination temperature (°C)	*BET surface area (m^2/g)*	*Pore volume (cm^3/g)*	*Pore diameter (nm)*
700	*8.6141*	*0.013036*	*5.7960*

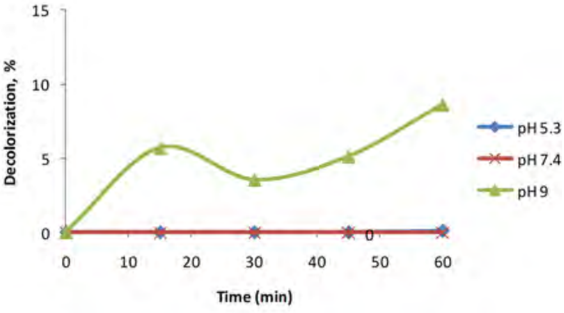

Figure 2. Effect of pH on ultrasonic decolorization of biologically treated baker's yeast effluent

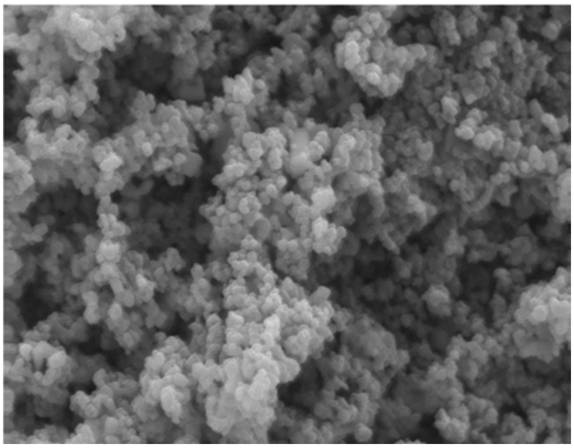

Figure 3. SEM images of prepared TiO_2/ZnO composite.

Before ultrasonic irradiation, 500 mL biologically treated baker's yeast effluent and desired amount of TiO_2/ZnO composite were put into the reaction vessel and magnetically stirred for 60 min. without any irradiation to show the adsorption capacity of the composite. Then the sample was taken out and centrifuged. The absorbance of the sample was measured. It was found to be no change in absorbance value compared with wastewater at the beginning. Then ultrasonic irradiation was applied.

Experiments were done by adding different amounts of TiO_2/ZnO composite and the original pH value of the wastewater. As shown from Figure 4, addition of catalyst ensured decolorization. As the catalyst ratio increases from 0.1 to 0.15 g/L, the decolorization increases. Increase in catalyst amount provides an increase in total surface area of catalyst, so the generation of •OH radicals intensifies. After the optimum catalyst amount decolorization decreases, because excessive amounts of catalyst may inhibit dissipation of the ultrasound and the generation of radicals. Accordingly, sonocatalytic activity decreases.

Similar results were reported in literature. Abdullah and Liang [7] investigated the effect of TiO_2 loading on sonocatalytic degradation of organic dyes. The degradation efficiency of organic dyes rose when the TiO_2 loading was increased from 1 to 1.5 g/L. The effect was attributed to the increasing sites to generate free radicals with increasing sonocatalyst loading. The removal efficiency began to decline at higher loadings. The lower removal at high loadings of the catalyst could be explained by the fact that excessive TiO_2 particles would cause mutual screening effects of the particles that shield congo red molecules from receiving sonic waves. In another study, Jamalluddin and Abdullah [10], the effect of catalyst ratios on sonocatalytic degradation of reactive blue 4 was investigated. According to the results, too much of catalyst added into the reaction system would cause the mutual screening effect among the catalyst particles. Thus, the energy provided by the ultrasound could not reach the surface of the catalyst to consequently result in lower generation of active radicals.

COD removal

The samples withdrawn were analyzed for the changes in the COD. The effect of the ultrasound on COD removal of the biologically treated baker's yeast effluent is shown in Figure 5. COD removal was 17% and 33% by using only ultrasound and combination of ultrasound and 0.15 g/L TiO_2/ZnO composite respectively.

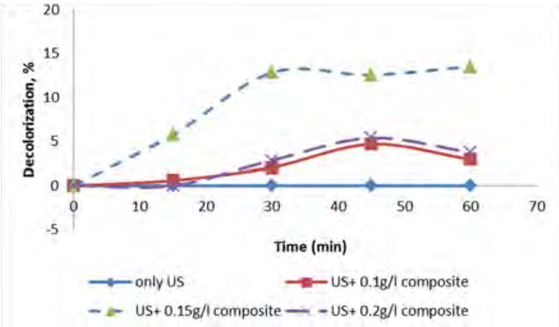

Figure 4. Effect of TiO_2/ZnO composite amount on ultrasonic decolorization of biologically treated baker's yeast effluent

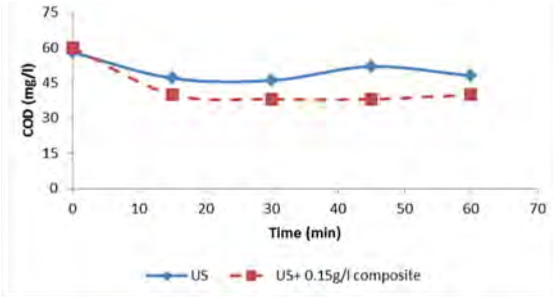

Figure 5. Effect of TiO_2/ZnO composite on ultrasonic COD removal of biologically treated baker's yeast effluent

Organic load of the biologically treated baker's yeast effluent was low. However, COD was not completely removed under the ultrasonic irradiation within the 60 min. reaction time. Degradation products are recalcitrant to ultrasonic irradiation. A similar result is obtained by Merouani et. al [21]. According to their results, intermediate products have very low probabilities of making contact with •OH radicals, which react mainly at the interface of the bubble. Thus the sonochemical action that gives rise to a product bearing more hydroxyl groups is of low efficiency toward COD abatement.

CONCLUSIONS

In the present study, ultrasonic decolorization and COD removal of biologically treated baker's yeast effluent were studied. The effect of pH and TiO_2/ZnO composite amount were investigated for ultrasonic treatment of baker's yeast effluent. According to the results, there was no decolorization of biologically treated baker's yeast effluent by using ultrasound solely. A combination of TiO_2/ZnO composite and ultrasonic irradiation improved decolorization of biologically treated baker's yeast effluent. Highest decolorization was obtained at 0.15 g/L composite amount. COD removal was 17% with ultrasound and 33% with the combination of ultrasound and 0.15 g/L composite.

ACKNOWLEDGEMENTS

The authors thank to the Hitit University for their financial support of this project under contract of MUH19004.13.002.

REFERENCES

1. Chandra R, Bharagava RN, Rai V. Melanoidins as major colourant in sugarcane molasses based distillery effluent and its degradation. Bioresource Technology 99 (2008) 4648–4660.
2. Satsawali Y, Balakrishnan N. Wastewater treatment in molasses–based alcohol distilleries for COD and color removal: A review. Journal of Environmental Management 86 (2008) 481–497.
3. Pena M, Coca M, Gonzalez G, Rioja R, Garcia MT. Chemical oxidation of wastewater from molasses fermentation with ozone. Chemosphere 51 (2003) 893–900.

4. Liang Z, Wang Y, Zhou Y, Liu H, Wu Z. Variables affecting melanoidins removal from molasses wastewater by coagulation/flocculation. Separation and Purification Technology 68 (2009) 382–389.
5. Joseph CG, Puma GL, Bono A, Krishnaiah D. Sonophoto–catalysis in advanced oxidation process: A short review. Ultrasonics Sonochemistry 16 (2009) 583–589.
6. Moumeni O, Hamdaoui O. Intensification of sonochemical degradation of malachite green by bromide ions. Ultrasonics Sonochemistry 19 (2012) 404–409.
7. Abdullah AZ, Liang PY. Heat treatment effects on the characteristics and sonocatalytic performance of TiO_2 in the degradation of organic dyes in aqueous solution. Journal of Hazardous Materials 173 (2010) 159–167.
8. Gao J, Jinag R, Wang J, Kang P, Wang B, Li Y, Li K, Zhang X. The investigation of sonocatalytic activity of Er^{3+}:$YAlO_3$/TiO_2–ZnO composite in azo dyes degradation. Ultrasonics Sonochemistry 18 (2011) 541–548.
9. Gao J, Jinag R, Wang J, Kang P, Wang B, Li Y, Li K, Zhang X. Sonocatalytic performance of Er^{3+}:$YAlO_3$/TiO_2-Fe_2O_3 in organic dye degradation. Chemical Engineering Journal 168 (2011)1041–1048.
10. Jamalluddin NA, Abdullah AZ. Reactive dye degradation by combined Fe(III)/TiO_2 catalyst and ultrasonic irradiation: Effect of Fe(III) loading and calcination temperature. Ultrasonics Sonochemistry 18 (2011) 669–678.
11. Anju SG, Jyothi KP, Joseph S, Suguna Y, Yesodharan EP. Ultrasound assisted semiconductor mediated catalytic degradation of organic pollutants in water: Comparative efficacy of ZnO, TiO_2 and ZnO–TiO_2. Research Journal of Recent Sciences 1 (2012) 191–201.
12. Ahmad M, Ahmed E, Hong ZL, Ahmed W, Elhissi A, Khalid NR. Photocatalytic, sonocatalytic and sonophotocatalytic degradation of Rhodamine B using ZnO/CNTs composites photocatalysts. Ultrasonics Sonochemistry 21 (2014) 761–773.
13. Sangave PC, Pandit AB, Ultrasound pre–treatment for enhanced biodegradability of the distillery wastewater. Ultrasonics Sonochemistry 11 (2004) 197–203.
14. Sangave PC, Gogate PR, Pandit AB. Ultrasound and ozone assisted biological degradation of thermally pretreated and anaerobically pretreated distillery wastewater. Chemosphere 68 (2007) 42–52.
15. Verma AK, Raghukumar C, Naik CG. A novel hybrid technology for remediation of molasses–based raw effluents. Bioresource Technology 102 (2011) 2411–2418.
16. Wang J, Jiang Z, Zhang L, Kang P, Xie Y, Lv Y, Xu R, Zhang X. Sonocatalytic degradation of some dyestuffs and comparison of catalytic activities of nano sized TiO_2, nano sized ZnO and composite TiO_2/ZnO powders under ultrasonic irradiation. Ultrasonics Sonochemistry 16 (2009) 225–231.
17. Wang J, Lv Y, Zhang L, Liu B, Jiang R, Han G, Xu R, X. Zhang X. Sonocatalytic degradation of organic dyes and comparison of catalytic activities of CeO_2/TiO_2, SnO_2/TiO_2 and ZrO_2/TiO_2 composites under ultrasonic irradiation. Ultrasonics Sonochemistry 17 (2010) 642–648.
18. Yılmaz E. Maya endüstrisi atıksuyunun ses ötesi dalgalarla arıtılması, Master Thesis, Hitit University, 2014.
19. Jiang Y, Petrier C, Waite TD. Effect of pH on the ultrasonic degradation of ionic aromatic compounds in aqueous solution. Ultrasonics Sonochemistry 9 (2002) 163–168.
20. Pang YL, Abdullah AZ, Bhatia S. Rewiev on sonochemical methods in the presence of catalyst and chemical additives for treatment of organic pollutants in wastewater. Desalination 277 (2011) 1–14.
21. Merouani S, Hamdaoui O, Saoudi F, Chiha M. Sonochemical degradation of Rhodamine B in aqueous phase: Effects of additives. Chemical Engineering Journal 158 (2010) 550–557.

Hittite Journal of Science and Engineering, 2015, 2 (1) 65-76
ISSN NUMBER: 2149-2123
DOI: 10.17350/HJSE19030000010

Hillock Formation by Surface Drift-Diffusion Driven by the Gradient of Elastic Dipole Interaction Energy Under Compressive Stresses in Bi-Crystalline Thin Films

Tarik Omer Ogurtani[1] and Oncu Akyildiz[2]
[1] Middle East Technical University, Department of Metallurgical and Materials Engineering, Ankara, TURKEY.
[2] Hitit University, Department of Metallurgical and Materials Engineering, Corum, TURKEY.

Article History:
Received: 2015/05/07
Accepted: 2014/06/15
Online: 2015/07/01

***Correspondence to**: Tarık Omer Ogurtanı,*
Middle East Technical University, Faculty of Engineering, Department of Metallurgical and Materials Engineering, Ankara, Turkey
Tel: +90 (312) 210-2512
Fax: +90 (312) 210-1267
E-Mail: ogurtani@metu.edu.tr

ABSTRACT

We investigated surface drift diffusion induced grain boundary (GB) grooving and ridge (hillock) formation and growth, under the combined actions of the capillary forces and applied uniaxial compressive stresses, in bi-crystal thin films with dynamical computer simulations. In the present theory, the generalized driving force for the stress induced surface drift diffusion includes not only the usual gradient of the elastic strain energy density, but also the elastic dipole tensor interaction energy. During the morphological evolution of GB ridge formation and growth, triple junction (TJ) displacement and its velocity are continuously tracked down in order to resolve precisely the crossover time and depth at which velocity sign inversion takes place. An incubation time for the onset of the ridge growth stage coupled to the GB-TJ displacement velocity inversion is defined and its dependence on the stress is investigated. This analysis implies that the ridge growth stage is not controlled by Ziegler's 'maximum entropy production principle' but rather Prigogine's 'minimum entropy production hypothesis' for the stationary non-equilibrium states in complex systems, which are exposed to external applied body forces and surface tractions.

Key Words:
Grain Boundary Grooving; Non-Equilibrium Thermodynamics; Surface/Grain Boundary Diffusion; Compressive Stresses; Thin Films.

INTRODUCTION

Abbreviations:

GB	: grain boundary;
TJ	: triple junction;
EDTI	: elastic dipole tensor interaction;
ESED	: elastic strain energy density

Grain boundary (GB) thermal grooving is a capillary driven surface morphological evolution, and observed in the vicinity of the grain boundary- free surface junctions in polycrystalline materials at rather elevated temperatures. When the underlying bulk system is exposed to the external and/or internal stress fields the problem becomes much more complicated. One of the most widely employed method to study the effects force fields on the GB grooving, is to couple the capillary-driven surface diffusion with the steady state atomic flux induced by the normal component of the surface traction acting on the GB layer.

Following this approach Genin et al. [1] extended Mullins' [2] classical theory of thermal grooving to study the development of an isolated groove with constant GB flux due to normal compressive stress gradients (i.e., Herrings' force) acting on the GB layer. They observed stagnation of the groove formation under compressive stresses.

In addition to GB grooving, the formation and development of ridges or hillocks is one of the most commonly observed surface reconstruction phenomena in polycrystalline thin films. *In situ* observations of thin films revealed that ridges generally form in the vicinity of GB TJs; and it is thought that they form under the influence of residual and/or thermo-mechanical compressive stresses, induced during the deposition and/or the thermal cycling processes, respectively [3–9].

One of the drawbacks of the study of Genin and coworkers [1, 6, 7] was the absence of long range surface diffusion into the ridge from the surroundings film area. Kim et al. [9] indicated the essence of long range diffusion by citing Chaudhari's [10] ridge model in which an analysis of the lattice diffusion (Nabarro – Herring creep) was presented. Presland et al. [11], on the other hand, provided the evidence for the surface diffusion controlled mechanism during ridge growth in silver thin films. These authors directly adopt the results of the Hull-Rimmer theory [12] by noting the similarity between the two problems, ridge growth and GB void growth, after making suitable arrangements. As a result, they obtained a ridge growth rate which is linearly proportional with the applied stresses. Gao et al. [13] and Zhang and Gao [14] have studied constrained grain boundary diffusion coupled with the surface diffusion, leading to formation of crack-type wedges via mass transfer between grain boundary region and the free surface of the film. The proposed coupling relies on the crack tip curvature and its higher derivatives (See: Eqs. 13 and 14 of reference 14) where, the surface drift diffusion considered in their treatment is of Mullins type, which is completely controlled by the capillary forces acting along the free surfaces and there was no attempt to consider the gradient of hydrostatic part of stress tensor as a driving force.

The elastic strain energy density (ESED) gradient driven instability is predicted to occur for stresses of either sign (quadratic stress dependence). However, for a kinetically driven instability, if the interface is unstable for a given stress state, then it should necessarily be stable for the opposite stress state or vice versa [15]. Lahiri [16] studied ridges on a Pb thin film and observed the effect of stress sign reversal: The ridges grow under compressive stresses and shrink in height under tensile stresses. Similarly, Barvosa-Carter et al. [15] demonstrated that the corrugated Si (001) interface is stable under tensile and roughens under compressive stresses. It is evident that ESED cannot play any role in the sign reversal behavior observed in surface morphological evolutions but a term with a linear stress dependence can.

In this paper, we considered the role of the gradient of the hydrostatic part the stress tensor generated by the applied uniaxial compressive stress system as a driving force on the surface drift diffusion (via isotropic surface point defects) through the elastic dipole tensor interaction (EDTI), which was proposed and elaborated by Ogurtani [22] and presented briefly in Appendix. The EDTI is accounted for the interactions in the bulk phases between the strain field of the mobile atomic carriers (mono-vacancies or paraelastic defects such as Frenkel defects) and the local stress fields. EDTI is also valid for the mobile defects 'ad atoms' lying at the surface layer as well as in the grain boundary region as demonstrated by Kirchheim [18] in his well-accepted classical work. Later, other authors also employed the concept for bulk [19] and grain boundary [20] diffusion. According to our best knowledge, excluding our recent work on the effects of applied uniaxial tension stresses on GB grooving [21], there exists neither gross scale simulation nor analytical work that reflects the dominant effect of long range surface drift-diffusion driven by the stress gradient in the literature. The main reason for this is that the surface is always assumed to be traction free, and thus the Herring's force vanishes identically (see Appendix).

The present computer simulation experiments emphasize the crucial role played by the EDTI as driving force for surface diffusion in explaining the GB grooving under compressive stresses as well as the ridge formation at the GBs. In these experiments, we did not take into account the particle flux coming from or going through the GB region (evaluated at the TJ) directly. In other words, we assumed that the material drainage at the GB-groove tip and transfer through the GB by the non-vanishing stress field gradients as well as by the concentration inhomogeneities of the mobile species is negligibly small compared to the material excavation and transport by the stress driven surface drift-diffusion operating along the groove surfaces via EDTI.

Physical and Mathematical Modeling

The thermodynamic composite system under consideration consists of two bulk regions, and a vapor phase. The bulk regions are connected by a GB, and the vapor phase is separated from the solid phase by a singly connected curved surface layer as illustrated in Figure 1. The surface layer and the GB region are both presumed to have finite and invariant thicknesses, denoted as h_s and h_g, respectively.

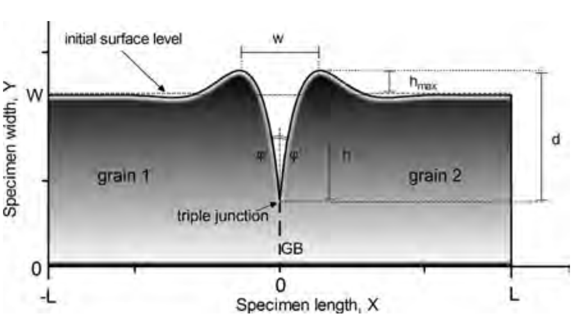

Figure 1. Sketch of a grain boundary groove, which evolves on the upper triple junction, illustrating its width (w), depth (h and d), maxima (hmax) and dihedral angle (φ). Here W and L denote the half film width and length, respectively. The grain boundary extends along the origin. .

a. The governing equation for the surface drift-diffusion and growth

According to the micro-discrete formulation of the irreversible thermodynamics of surfaces and interfaces [22, 23], the evolution kinetics of traction free surfaces exposed to the elastostatic fields in addition to the capillary forces, may be described in terms of surface normal displacement velocities $\bar{V}_{ord}$ by the following well-posed moving boundary value problem in 2D space for ordinary points. In the following expression, normalized and scaled parameters and variables are used, and they are indicated by the bar signs over the letters:

$$\bar{V}_{ord} = \frac{\partial^2}{\partial \bar{\ell}^2}\left(\Delta \bar{g}^o_{vb} + \bar{\kappa} + \Xi \bar{\sigma}_h + \Sigma \bar{\sigma}^2_h\right) - \bar{\mathrm{M}}_{vb}\left(\Delta \bar{g}^o_{vb} + \Sigma \bar{\sigma}^2_h + \bar{\kappa}\right) \tag{1}$$

In the above expression, $\bar{\ell} \equiv \ell / \ell_o$ is the normalized curvilinear coordinate along the surface (arc length) in 2D space. Here, ℓ_o is the arbitrary length scale, and is chosen as $\ell_o = h_o / 2 \Rightarrow 100$ nm for the present simulation studies, Here, h_o is the thickness of the thin film having a length designated by L_o, which is taken as equal to $L_o = 30\ell_o \Rightarrow 3.0$ µm . This choice implies that the aspect ratio of the test module, denoted by $\beta \equiv L_o / h_o$, is 15. $\Delta \bar{g}^o_{vb}$ denotes the normalized thermal part of the volumetric Gibbs free energy density difference $\breve{g}_{vb} = (\breve{g}^o_v - \breve{g}^o_b)$ between the realistic void phase (vacuum/vapor) and the bulk matrix ($\Delta \bar{g}^o_{vb}$<0 evaporation or void growth). This normalization is done with respect to the specific surface Gibbs free energy of the surface phase denoted by g_s, and it is given by $\Delta \bar{g}_{vb} = \breve{g}_{vb} \ell_o / g_s$, which also involves the length scale or the metric ℓ_o. Similarly, the second group of terms in Eq. (1) is related to the surface growth process, which will not be employed in the present simulation studies ($\Delta \bar{g}^o_{vb} = 0;\ \bar{\mathrm{M}}_{vb} = 0$) to avoid further complications in data interpretations.

In Eq. (1), $\bar{\kappa} = \kappa \ell_o$ is the local curvature and is taken to be positive for a concave solid surface (troughs). Similarly, the positive direction of the surface displacement is assumed to be towards the bulk (matrix) phase, which implies the growth of surface troughs or grooves, and the simultaneous shrinkage of crest regions.

The normalized hoop stress is denoted by, $\bar{\sigma}_h = \sigma_h / \sigma^o_h$, which was normalized with respect to the nominal stress applied at the edges of the specimen, σ_o. The hoop stress in plane strain condition may be defined by $\sigma_h = \hat{t}.\underline{\underline{\sigma}}.\hat{t}$, where $\hat{t}$ is the unit surface tangent vector, and $\underline{\underline{\sigma}}$ is 2D-stress tensor evaluated at the bulk region just adjacent to the surface layer. The hoop stress for the traction free surfaces may be given by the following exact connection: $\sigma_h = Tr\underline{\underline{\sigma}}$ since $\hat{n}.\underline{\underline{\sigma}}.\hat{n} = 0$ for traction free surfaces. The double under bars indicate tensor quantities. Ξ designates the elastic dipole tensor interaction (EDTI) parameter, which is given by the expression $\Xi = (1+\nu)\ell_o \sigma^o_h\ Tr\underline{\underline{\hat{\lambda}}}/3g_s$. Here, $Tr\underline{\underline{\hat{\lambda}}}$ is the trace of the elastic dipole tensor. For further applications of EDTI on the stress dependent surface growth mobility, one may refer to Ogurtani and Akyildiz [24], Ogurtani and Oren [23]. Similarly, the dimensionless parameter Σ corresponds to the relative value (referred to the capillarity) of the intensity of the elastic strain energy density (ESED) contribution on the stress-driven surface drift-diffusion. For plain strain condition, ESED takes the following form: $\left(\underline{\underline{\sigma}} : \underline{\underline{\varepsilon}} / 2 \rightarrow (1-\nu^2)\sigma^2_h / 2E\right)$. Here $\underline{\underline{\varepsilon}}$ is the strain tensor, E is the Young's modulus, and ν is the Poisson' ratio. Then one writes $\Sigma = (1-\nu^2)\ell_o \left(\sigma^o_h\right)^2 / 2Eg_s$.

The time and space variables $\{t, \ell\}$ are scaled in the following fashion: first of all, $\hat{\mathrm{M}}_s = (D_s h_s / \Omega_s kT)$, an atomic mobility associated with the mass flow at the surface layer is defined and then a new time scale is introduced by $\tau_o = \ell^4_o / (\Omega^2_s \hat{\mathrm{M}}_s g_s)$. Here, Ω_s and D_s are the mean atomic volume of chemical species in the surface layer and the isotropic part (*i.e.*, the minimum value) of the surface diffusion coefficient respectively. The generalized mobility, $\hat{\mathrm{M}}_{vb}$, associated with interfacial displacement reaction taking place during the surface growth process (adsorption or desorption) is also normalized with respect to the mobility of the surface diffusion, $\hat{\mathrm{M}}_s$, and is given by $\bar{\mathrm{M}}_{vb} = \hat{\mathrm{M}}_{vb} \ell^2_o / \hat{\mathrm{M}}_s$. The normalized time $\bar{t}$ and the test module thickness $\bar{h}_o$ used in the present simulations are defined by $\bar{t} = t / \tau_o$, and $\bar{h}_o = h_o / \ell_o$, respectively.

TJ drift velocity along the rigid GB can be represented by [22, 23]:

$$\bar{V}^{long}_g = \bar{\mathrm{M}}^{long} \frac{\Omega_g d_a}{2\Omega^2_s h_g}\left[2\lambda - \left(\cos\varphi^+ + \cos\varphi^-\right)\right] \tag{2}$$

Here, d_a, and Ω_g are the interatomic distance and mean atomic volumes of chemical species in the GB layer, respectively. $\bar{M}^{long}$ is the longitudinal generalized mobility of the TJ, which is defined below. φ^+ and φ^- are the dihedral angles as illustrated in Figure 1. λ is the wetting parameter associated with the TJ, which is assumed to be isotropic in the present case study. It may be given by $\lambda = g_g / 2g_s$, where g_g is the specific surface Gibbs free energy associated with the GB.

The following boundary conditions at the TJ in terms of right and left side fluxes associated with the surface layer may be written;

$$\bar{J}^{\mp}_o = \mp \bar{\mathrm{M}}^{long} \frac{\bar{d}_a}{2\bar{\Omega}^2_s}\left(\lambda - \cos\varphi^{\mp}\right) \mp \bar{J}_g / 2 + \bar{\mathrm{M}}^{trans} \frac{\bar{d}_a}{\bar{\Omega}^2_s}\left(\sin\varphi^+ - \sin\varphi^-\right) \tag{3}$$

In the above equation, the $(\mp)$ first group of terms represents the material lost from the TJ-edge of the GB layer due to shortening of its length caused by the GB-TJ longitudinal motion, and then injected equally into the both branches of the surface layer to extend its length (*in situ* 2D-phase transition). The last group of terms corresponds to the mass transfer from one side of the surface layer to another side through the GB-TJ region to compensate the asymmetry in the surface groove profile till the non-equilibrium stationary state having symmetrically disposed configuration is attained asymptotically. Here, the particular partition of the incoming GB flux $\bar{J}_g$ between $\bar{J}_o^+$ and $\bar{J}_o^-$ at the GB-TJ is a matter of convenience; otherwise it is completely arbitrary as long as one satisfies the generalized law of conservation of particles including the *in situ* phase transformation at the TJ. Here, the positive direction of the surface flux $\bar{J}_o^{\mp}$ is taken along the clock-wise direction enclosing sidewalls of the finite specimen in 2D space. Similarly, $\bar{J}_g$ denotes the normalized atomic flux associated with the incoming GB mass flow evaluated just at the GB-TJ. In the present simulation studies, the atomic grain boundary flux term $\bar{J}_g$ is not considered.

$\bar{\mathrm{M}}^{trans}$ corresponds to the normalized transverse mobility of the TJ with respect to $\hat{\mathrm{M}}_s$. The explicit expressions may be given by:

$$\hat{\mathrm{M}}^{long} = \frac{\Re^{long}}{kT}\frac{h_g}{\Omega_g}, \hat{\mathrm{M}}^{trans} = \frac{\Re^{trans}}{kT}\frac{h_s}{\Omega_s}, \hat{\mathrm{M}}_s = \frac{D_s}{kT}\frac{h_s}{\Omega_s} \qquad (4)$$

Where, $\Re^{long}$ and $\Re^{trans}$ are the transition rates associated with the longitudinal and transverse displacements of the TJ, which may be calculated by Eyring [26] transition rate theory.

b. Numerical methods

In the evaluation of the hoop stresses at the top and bottom free surfaces of the thin metallic bicrystal film including GB groove faces we utilize the simplest implementation of the indirect boundary element method (IBEM) [27] which utilizes the mid-positions of the straight line elements in two dimensional space as collocation points. This guarantees the surface smoothness conditions for the validity of the governing Fredholm integral equation of the second kind at the corners and edges. Neumann boundary conditions are employed along the top and bottom surfaces (i.e., surface tractions are zero, $\underline{\underline{\sigma}}.\hat{n} = 0$) and prescribed surface normal tractions (i.e., uniaxial compression defined as $\mp\sigma_{xx}\big|_{\pm L}\hat{x}$ at $\pm L$) at the specimen edges. The explicit Euler's method combined with the adaptive time step auto-control mechanism is employed in connection with Gear's stiff stable second-order time integration scheme [28] with the initial time step selected in the range of $\left(10^{-8} - 10^{-9}\right)$ in the normalized time domain. This so-called adaptive time step procedure combined with the self-recovery effect of the capillary terms guarantees the long-time numerical stability and accuracy of the explicit algorithm even after performing $2^{75} - 2^{90} \approx 10^{27}$ steps. An adaptive mesh refining procedure is continuously applied using the criteria advocated by Pan and Cocks [29]. Typically, the number of active collocations points in our discretization scheme varied from 400 to about 550 depending on the normalized applied stress and TJ-longitudinal mobility. The curvature and the normal line vector are evaluated at each node for each time step by using discrete geometric relationships in connection with the fundamental definitions of the radius of curvature in differential geometry.

In our calculations, a few percent unavoidable mass leakage is observed at low stress levels $\left(\Xi \le -0.1\right)$ to the system, which shows appreciable improvements at the moderate to high stress levels $\left(\Xi \ge 1\right)$. This leakage arises from both edges of the test modulus even though we are employing insulating boundary conditions:

$$J_{Edges} = \frac{\partial}{\partial \bar{\ell}}\left(\bar{\kappa} + \Xi\bar{\sigma}_h + \Sigma\bar{\sigma}_h^2\right)\Big|_{L_\pm} \to 0$$

The main reason is associated with the fact that one doesn't have enough number of collocation points at the critical spots of the test modulus such as edges and corners, where the extreme high stress concentrations take place. We have also used a special program to compensate this mass leakage at the edges, which adds to or subtracts material from the upper and lower surfaces, respectively, using a well-defined scaling factors. On the other hand, the genuine mass accumulations at the ridges mainly come from the upper and lower surfaces of the specimen, which results as the thinning of the film. This thinning is very hardly noticeable since the sample has a very high length to thickness aspect ratio.

In the next section, while discussing on the simulation results we would often encounter with the time constant and thus it is beneficial to get some idea on the magnitude of the tentative time constant based on the available experimental data in the literature. According to the definitions of the time constant τ_o and the surface mobility $\hat{M}_s$ introduced previously, one may write $\tau_o \equiv \left[kT\ell_o^4/(\Omega_s D_s h_s g_s^o)\right]$, which may be easily calculated using the published physico-chemical data available in the literature. Using the values tabulated for copper in Table 1, one finds that $\tau_o \cong 5.72\times\left[10^{+2} - 10^{+6}\right]$ s depending upon the selected scale length ℓ_o $[100\,nm - 1000\,nm]$ at $T = 573^o K$, which is the standard device accelerated test temperature. At room temperature, $T = 300^o K$, one obtains about eight orders of magnitudes higher values for the normalized time such as $\tau_o \cong 1.2\times\left[10^{10} - 10^{14}\right]$ s.

Table 1. Physicochemical properties of Al, Cu, Sn, and Pb [38].

	Al	*Cu*	*Sn*	*Pb*
Elastic Moduli (GPa)	70.6	129.8	49.9	16.1
Poisson' Ratio	0.345	0.343	0.35	0.44
Surface tension (nm^{-1})	0.915	1.780	0.685	0.480
$\lvert tr(\underline{\underline{\lambda}})\rvert$	0.69	0.3	0.6	0.6
Q_s (eV)	0.62	0.95	0.506	-
$D^o_s(m^2s^{-1})$	$3x10^{-6}$	$5.84x10^{-5}$	$4.9x10^{-4}$	-
$h_s(m)$	$2.86x10^{-10}$	$2.56x10^{-10}$	$5x10^{-10}$	-
$\Omega_S(m^3)$	$1.66x10^{-29}$	$1.18x10^{-29}$	$2.71x10^{-29}$	$3.02x10^{-29}$

RESULTS AND DISCUSSIONS

In this section, first we will compare general features of the profiles obtained under the low uniaxial compressive stress field and the one deduced from the thermal grooving experiment presented in Figure 2d, where only the capillary forces are in action. Then the topological effects of the increase in the applied uniaxial compressive stress are examined critically by altering EDTI parameter covering a wide range of values: [$\Xi = -0.1, \dots ,1,.. -10$].

In the present simulations ESED contribution is ignored due to the fact that the EDTI term is at least a few orders of magnitude larger; especially for the medium and low stress levels. Using the values tabulated in Table 1; for a copper film having a thickness of $h_o = 200$ nm with a scaling length ℓ_o =100 nm, the given EDTI interval corresponds to [σ_{Cu}=13.25–1325] MPa, and for aluminum: [σ_{Al}=2.96–296] MPa. These stress ranges yield for ESED, respectively: [Σ_{Cu}=3.5x10^{-5},..., 3.5x10^{-1}] and [Σ_{Al}=6.3x10^{-6},..., 6.3x 10^{-2}]. However, as we mentioned previously, the difference between these two parameters decreases as the stress level increase. This is due to the quadratic dependence of ESED rather than the linear dependence of EDTI to the stress. It was found by Ogurtani [22] that the threshold level of the stress was about 21 GPa for the silicon and 15.6 GPa for copper thin crystal films, and above which the elastic strain energy w_{ESED} starts to dominate the elastic dipole tensor interaction energy denoted by u_{EDTI}, according to the relationship: $\left\{u_{EDTI} / w_{ESED} = -2ETr\underline{\underline{\hat{\lambda}}}\sigma_o^{-1}/3\right\}$. The upper stress level employed for the present simulations for 200 nm thick samples can be comparable with findings of Friesen et al. [30] namely, the instantaneous stress level at the initiation of the Volmer–Weber growth of polycrystalline Cu films was lower in the pre-coalescence regime (of order 1 GPa), and increased monotonically up to the film continuity, and then remained constant thereon (of order 10 GPa). Still the 100 nm Cu film deposited on the backside of each cantilever to improve the laser reflectivity did not show any plastic deformation, and showed rather reversible stress evolution during the growth.

Here, the initial configurations of the reported test modulus are always a flat surface having a freshly formed GB cutting the crystal into two pieces. Accordingly; the groove tip displacement is measured with respect to the original surface and the positive direction is chosen towards the bulk phase (Figure 1). In this paper, only the upper half of the test modulus is illustrated, which has reflection symmetry with respect to the mid-plane of the bicrystal.

Successive profiles, given in Figure 2a-b, show that the evolution under a uniaxial compressive stress (Ξ=−0.1) is tend to form a ridge (hillock) at the GB. The groove depth '*h*', which is measured from the initial flat surface towards the bulk region, is presented in Figure 2e on a semi log scale with respect to the normalized time. A close inspection shows that the depth follows up a $t^{1/4}$ trajectory after an initial transient stage, which can be categorized as Mullins' type, up to a certain depth where one observes a very pronounce peaking on the plot. This peaking depth may be called as the crossover depth designated by '$\overline{h}_c$', and similarly the corresponding normalized time may be designated as the crossover time for a good reason, and denoted by '$\overline{t}_c$'. If one zooms into the termination region of Figure 2c, it is observed that the GB-TJ displacement velocity is crossing the zero line and changes its sign, and then continues upwards to take negative values but ever decreasing in magnitude, and finally approaches zero line, asymptotically. This peculiar behavior is more pronounced in Figure 3b-4b, where a few orders of magnitude much higher stress is employed. Thus, the crossover time $\overline{t}_c$, where the depth, velocity and hoop stress versus log(time) plots, all show extremal behavior may be designated as the signature for the incubation time for the ridge formation and growth process.

Another characteristic length that was adopted by Mullins for his classical analytical theory; is the depth measured from the position of the peak maxima to the GB-root ($d=h+h_{max}$), and designated by '*d*'. It is also illustrated in Figure 3b in log-log scale together with the similar plot for the peak maxima $h_{\max}$. The simulation results presented in Figure 3 are obtained for a factor of ten increase in the

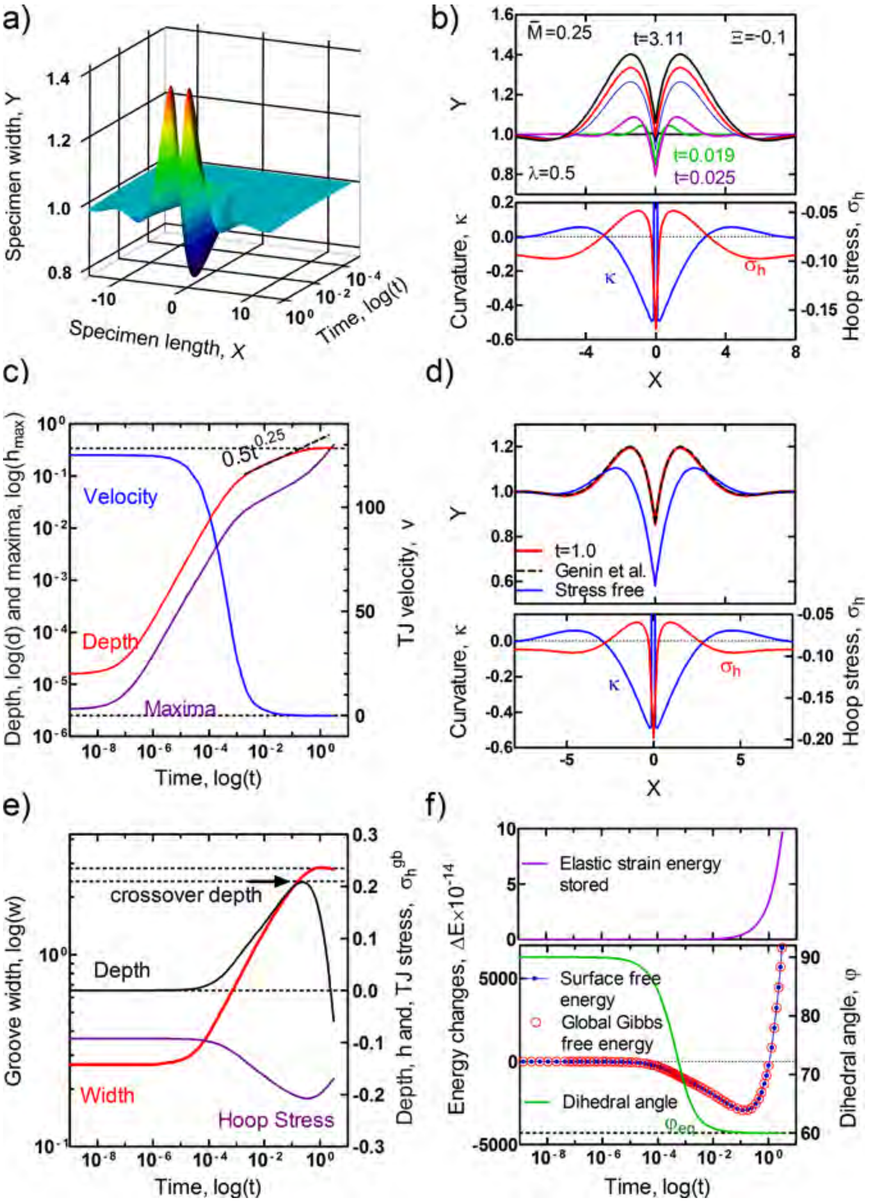

Figure 2. (Color online) Isotropic grain boundary grooving for λ=0.5, $\bar{M}^{long} = \bar{M}^{trans} = \bar{M} = 0.25$ and Ξ=−0.1. a) 3D representation of the groove evolution, b) successive 2D profiles; curvature and hoop stress distributions corresponding to t=3.11 (black profile), c) kinetic data for groove depth ('d'), maxima and TJ velocity, d) comparison of the stress free and groove under tension profiles given by Genin et al. [1] at t=1.0; curvature and hoop stress distributions at t=1.0, e) kinetic data for groove depth ('h'), width and TJ stress, f) energy changes and the kinetic data for the dihedral angle in semi-log scale.

applied nominal stress Ξ =1.0, compared to the previous simulation experiment. Figure 3b clearly indicates that the distance from the groove root to the maxima *'d'* shows a well-defined plateau during the ridge growth, even though the peak maxima doesn't show any sign of stagnation but rather elevation. Here a slight overshooting also takes place before the dihedral angle reaches to the non-equilibrium stationary value (Figure 3d-4d). All these indicate that the ridge translates into a nonequilibrium stationary state (according to the definition of Prigogine [31], when the Mullins' depth and width parameters enter into the well-defined plateau regime as may be also seen in Figure 2c-d by zooming if one filters out the white noise associated with the local internal entropy production.

In Figure 3c-4c the kinetics of the groove width and

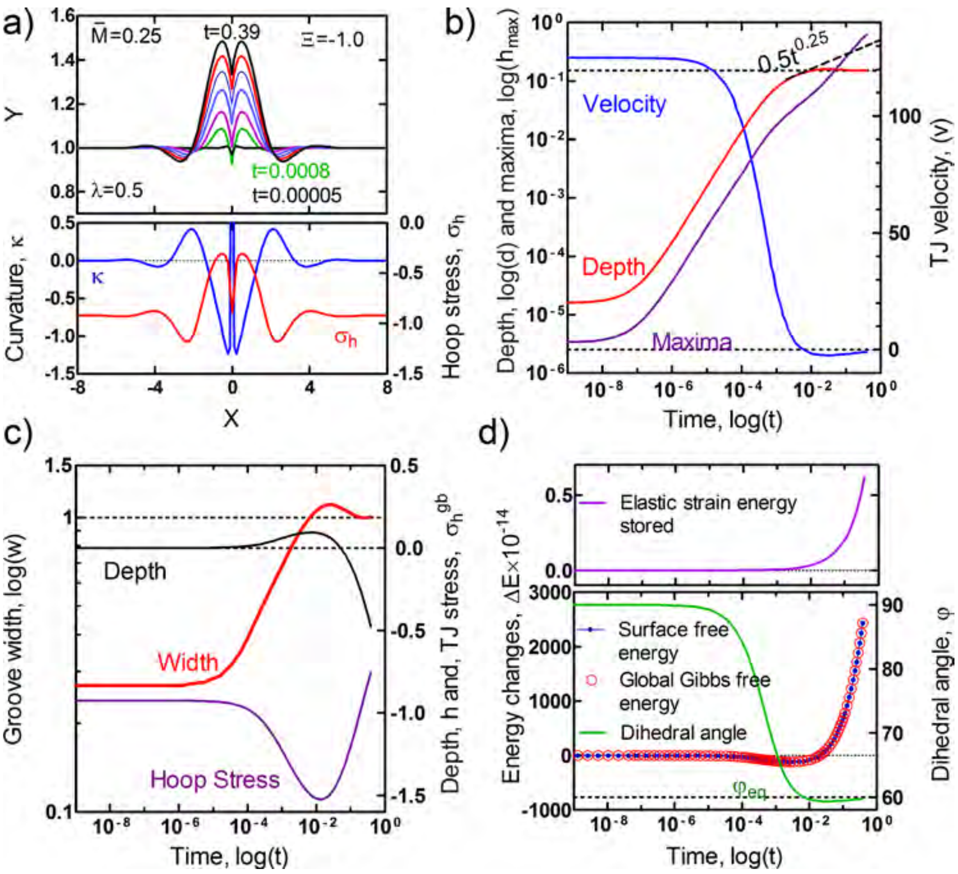

Figure 3. (Color online) Isotropic grain boundary grooving for λ=0.5, $\bar{M}^{long} = \bar{M}^{trans} = \bar{M} = 0.25$ and Ξ=−1.0. a) successive 2D profiles; curvature and hoop stress distributions corresponding to t=0.39 (black profile), b) kinetic data for groove depth ('d'), maxima and TJ velocity, c) kinetic data for groove width, depth ('h') and TJ stress, d) energy changes and the kinetic data for the dihedral angle in semi-log scale.

the value of the hoop stress at the TJ are also demonstrated. The compressive hoop stress value reported in these plots increase in magnitude as the groove deepens to h_c and then decreases as the grain boundary length increases with the ridge formation. On the contrary to the local hoop stress, the groove width stays constant during the plateau region. These are all strong indications for the existence of the ridge as a non-equilibrium stationary state under the given applied constant compressive stress system (isothermal isobaric natural process).

The solution proposed by Genin et al. [1] have also been presented in Figure 2d by reproducing it (using equations 23-27 of aforementioned article) for an arbitrary constant grain boundary flux of j=0.4, and for λ=0.5, B=1.0, and t=1.0. Although there are some fundamental differences, there exists a qualitative agreement between the Genin's analytic solution and the simulated profile in Figure 2. This is due to the fact that the dihedral angle and the GB-TJ velocity reported in Figure 2c-f follow trajectories very similar to the equilibrium trajectories employed in Mullins theory, during the natural evolution of the grain boundary groove at this moderately low stress levels. In the present case, the applied stress directly acts on the surface drift diffusion through the EDTI, while the GB region assumed to play no active role (no gradient driven matter flux is coming out from the GB to the TJ or vice versa, $J_g = 0$) in the overall process. The GB region has only one active role that is the direct involvement in the 2D-phase transition (in situ material exchange) taking place at the GB-TJ during its longitudinal displacement.

The free energy changes presented here in several plots are formulated recently [32] in great details for the isobaric composite system. Such a system is enclosed by external flexible and diathermal boundaries that allow not only establishing thermal equilibrium in the system, but also permitting to have a direct contact with the external constant surface tractions and body forces. That means the work done on the system is non-vanishing, $\Delta W \neq 0$. For such a system having a discrete free surface contour line, letting n to designate the total number of nodes, one may write down the rate of total strain energy relaxation (dissipation power) at a given time step i during the evolution

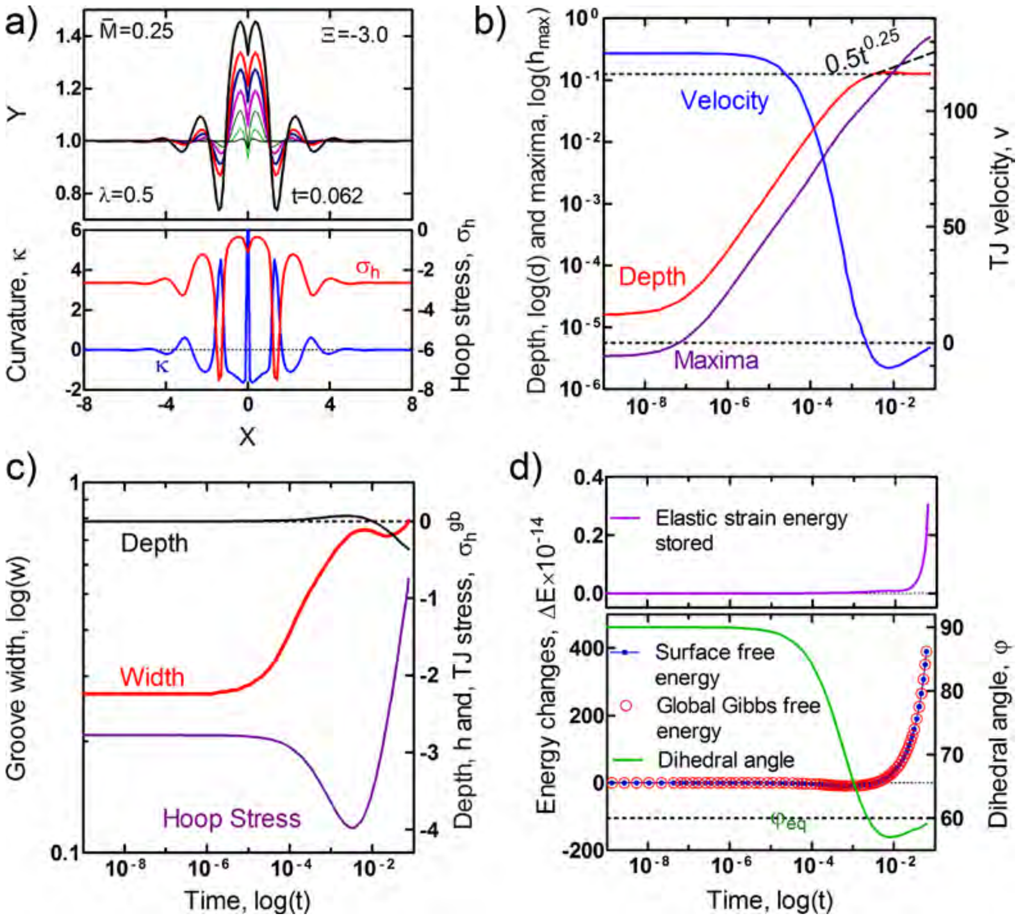

Figure 4. (Color online) Isotropic grain boundary grooving for λ=0.5, $\bar{\mathrm{M}}^{long} = \bar{\mathrm{M}}^{trans} = \bar{\mathrm{M}} = 0.25$ and Ξ=−3.0. a) successive 2D profiles; curvature and hoop stress distributions corresponding to t=0.062 (black profile), b) kinetic data for groove depth ('d'), maxima and TJ velocity, c) kinetic data for groove width, depth ('h') and TJ stress, d) energy changes and the kinetic data for the dihedral angle in semi-log scale.

as:

$$P_i = -\frac{(1-\nu^2)}{2E}\Im_i \sum_{j=0}^{n-1} \frac{\sigma_{h,ij}^2}{n} v_{ij} \;\Rightarrow\; \bar{P}_i = -w_o \ell_o^2 \bar{\Im}_i \sum_{j=0}^{n-1} \frac{\bar{\sigma}_{h,ij}^2}{n} \bar{v}_{ij} \qquad (5)$$

Here, $\bar{P}_i \equiv \tau_o P_i$ and $w_o \equiv (1-\nu^2)\sigma_o^2 / 2E$ is the nominal elastic strain energy density, and $E/(1-\nu^2)$ is the plain strain elastic modulus, $\bar{\Im}_i$ is the total scaled temporal length of the top surface of bi-crystal modulus including groove region at a given time step *i*, and with *j* standing for the collocation nodes of discrete surface. $\bar{\sigma}_{h,ij} \equiv (\sigma_{h,ij}/\sigma_o)$ and $\bar{v}_{ij}$ are the calculated normalized hoop stresses and velocities at each node. The summation is performed over the free surface contour line exposed to the surface drift diffusion. Then, the cumulative elastic strain energy relaxation (dissipation) of the body ΔE <0, which is according to Clapeyron's theorem [32, 33] compensated by one-halve of the work done on the isobaric system, may be calculated as a function of discrete normalized time $\bar{t}_i$ by a simple integration (*i.e.*, summation) procedure applied to above expression:

$$\Delta E_i \equiv \Delta \bar{E}_i = \bar{t}_i \sum_{k=0}^{i} \frac{\bar{P}_k}{i} < 0 \qquad (6)$$

The relationship in Eq. (6) is utilized to compute the total elastic strain energy relaxation, which is equal to the cumulative strain energy stored $\Delta \bar{W}_i^e$ in the body with an inverted sign $\Delta \bar{W}_i^e = -\Delta \bar{E}_i > 0$, and then the results are plotted in Figure 4d. The corresponding change in the bulk Gibbs free energy of a Hookian elastic solid is given by [33] $\Delta \bar{G}_i^b \cong \Delta \bar{F}_i^{Th} - \Delta \bar{W}_i^e \Rightarrow \Delta \bar{E}_i < 0$, assuming that the entropy density is not a sensitive function of strain. Here, $\Delta \bar{F}_i^{Th} \to 0$ is the thermal part of Helmholtz free energy, which is identically equal to zero for the isothermal changes. On the other hand, the global variations in the film surface free energy (capillary) including the shortening of the GB layer may be computed by the following equation:

$$\Delta \bar{G}_i^s = w_o \ell^* \left\{ \left(\bar{\Im}_i - \bar{L}_o \right) - 2\lambda \bar{h}_i \right) \right\} \qquad \text{(referred to the initial dead loaded state) (7)}$$

Here, $\ell^* \equiv \ell_o \Sigma^{-1}$ is the characteristic length, $\bar{h}_i$ is the temporal normalized depth measured from the original flat surface, and $\bar{L}_o$ is the initial flat top surface length. Then the global Gibbs free energy variations during GB grooving process as referred to the initial dead loaded state may be calculated from the following formula in real time and metric space, where $\Delta G_i^s \equiv \ell_o^2 \Delta \bar{G}_i^s$ and $\Delta G_i^b \equiv \ell_o \Delta \bar{G}_i^b$:

$$\Delta G_i^T = \Delta G_i^s - \Delta W_i^e = \Delta G_i^s + \Delta E_i \overset{?}{\leq} 0 \qquad \text{(referred to the initial dead loaded state)} \quad (8)$$

The free energy changes, which are normalized with respect to common cofactor $\left[w_o \ell_o^2\right]$ are given in Figure 2f, indicate that the absolute value of the cumulative strain energy relaxation increases monotonically as the surface roughness increases. On the contrary, the change in the global Gibbs free energy strictly follows the change in the surface free energy (due to the increase in the surface area), which makes a minima in negative scale and then monotonically increases to assume positive values. This anomalous situation as may be seen from Figures 3d and 4d is more critical for the higher stress levels, where one hardly can observe any dip in the global Gibbs free energy change. The global Gibbs free energy plots clearly show that the isothermal ridge growth process taking place above the TJ-velocity inversion point (See; the cross-over in Figures 3d and 4d) is energetically unfavorable.

Therefore, it is rather a kinetically driven process, which dominates the whole ridge growth stage. This also gives us a hint that the ridge growth stage is not controlled by Ziegler's [34] 'maximum entropy production principle, designated as $Td^2\Delta S/dt^2 \leq 0 \Rightarrow d^2\Delta G/dt^2 \geq 0$, but by the 'minimum entropy production hypothesis, characterized by $Td^2\Delta S/dt^2 \geq 0 \Rightarrow d^2\Delta G/dt^2 \leq 0$, as formulated by Prigogine [31] for the stationary weakly non-equilibrium states in linear complex systems, which are now exposed to fixed body forces and surface tractions.

In Figures 3 and 4, we presented the effect of an increase in the stress (EDTI) on the growth kinetics of a GB groove by surface diffusion under compressive stress fields. In each case distance '*d*' reaches a constant value, which is inversely proportional to the applied stress and similarly the value of the crossover depth decreases as stress increases. The amplitude of the secondary oscillations on both sides of the groove root rapidly increases with the applied stress during this kinetically driven evolution so that one may speak of extremely high surface instability above certain values.

An analysis of crossover depths 'h_c' and inversion-times collected for different levels of applied stresses may provide an analytical expression for the incubation time for ridge formation or may give an estimation of the time and depth, where grain boundary migration may start to occur if it is possible, as in the case of Genin's [6] model.

Such an analysis is presented in in Figure 5 and following equations are obtained by linear regression:

$$\bar{h}_c \cong 0.096 |\Xi|^{-1/3} \qquad (9)$$

$$\bar{t}_c \cong \begin{cases} 0.0062 |\Xi|^{-3/2}; & \Xi \leq 1.0 \\ 0.0058 |\Xi|^{-4/5}; & \Xi > 1.0 \end{cases} \qquad (10)$$

Reverting back into the real time and space the above equations yield into:

$$h_c \cong \left(\frac{0.002 g_s^o \ell_o^2}{\left|tr(\underline{\underline{\lambda}}_s)\right| (1+\nu) \sigma_o} \right)^{1/3} \qquad (11)$$

$$t_c \cong \begin{cases} \dfrac{0.035kT}{D_\sigma h_\sigma \Omega_\sigma} \left(\dfrac{\ell_o^{3/2} g_s^{o\,3/8}}{\left|tr(\underline{\underline{\tilde{\lambda}}}_s)\right| (1+\nu) \sigma_o} \right)^{3/2}; & \sigma_o \leq \dfrac{3g_s^o}{\left|tr(\underline{\underline{\tilde{\lambda}}}_s)\right| (1+\nu) \ell_o} \\ \dfrac{0.014kT}{D_\sigma h_\sigma \Omega_\sigma} \left(\dfrac{\ell_o^4 g_s^{o\,-1/4}}{\left|tr(\underline{\underline{\tilde{\lambda}}}_s)\right| (1+\nu) \sigma_o} \right)^{4/5}; & \sigma_o > \dfrac{3g_s^o}{\left|tr(\underline{\underline{\tilde{\lambda}}}_s)\right| (1+\nu) \ell_o} \end{cases} \qquad (12)$$

Figure 5b clearly shows that the crossover time plot has a very sharp knee at $\Xi_c \equiv \{\ell_o u_{EDTI} / g_s\} = 1$. Based on

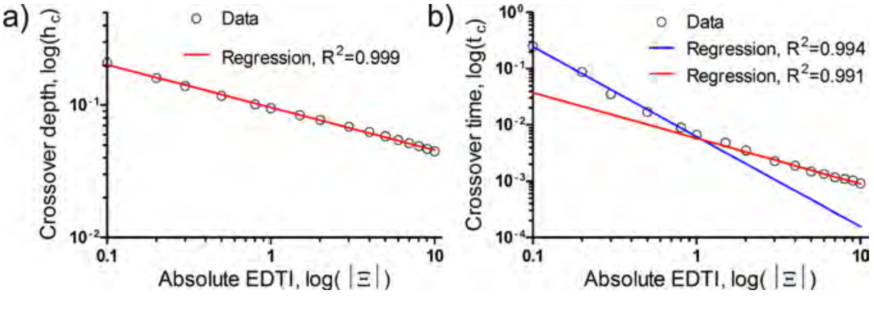

Figure 5. (Color online) Analysis of the crossover depth 'hc' and corresponding time as a function of the applied stress.

this information one can conclude that this parameter, in addition to the size of the specimen, is directly connected to the ratio of the EDTI and the surface Gibbs free energy densities. Thus it may be used as a threshold signature to separate the capillary and stress dominating regimes for the GB-ridge growth process under the uniaxial compressive stresses. This parameter also shows that the small specimen size pushes the system towards the capillary regime where the incubation time for the ridge formation stretches to longer times in logarithmic scale (i.e., apparent stagnation), just the contrary to the one should expect a priory.

CONCLUSIONS

In this study, we simulated and analyzed the surface morphological evolution kinetics associated with the GB-ridge formation and growth, in finite size bicrystal thin films under the applied uniaxial compressive stresses. In our simulations, the elastic dipole tensor interaction, between the strain field of mobile atomic species at the surface layer and the local stress field induced by the applied constant surface tractions and body forces, is considered to be the primary driving source rather than the gradient of the elastic strain energy density inhomogeneities. The most important outcomes of the extensive computer simulation studies may be outlined as follows:

1. On the contrary to the ESED, the use of gradient of the EDTI energy between the stress field and the mobile atomic species as a driving force for the surface drift-diffusion provides direct means to observe effects of compressive stresses on the evolution of bicrystal thin films for relatively small strength levels $\sigma_o \cong \{13.25(Cu) \text{ and } 2.86\text{ (Al)}\}$ MPa .
2. The effect of an applied stress field on GB grooving in thin film bamboo lines is studied in a wide range of EDTI parameters: Ξ = [–0.1, … , –10], which correspond to [–13.25, … , –1325] MPa for copper and [–2.96, … , –296] MPa for aluminum with scaling length of ℓ_o=0.1 μm. The application of compressive stresses slows down the groove penetration but rather favors development of grain boundary ridge profiles that are in accord with the results obtained by Genin et al. [1].
3. The present non-equilibrium thermokinetics theory has shown great potential for describing the growth kinetics of experimentally observed ridges in thin films through surface diffusion. However, there is still room for improvement by considering the grain boundary flux injection to GB-TJ by the applied stress system.
4. The grain boundary area increases during the ridge growth and such a process through an immobile boundary (normal to the initial film surface) is energetically unfavorable. Thus, a more complete model should be accounted for the GB migration (grain growth), which will be our future objective via the incorporation of TJ transverse motion. Yet in this study, an incubation time for hillock growth and a crossover depth, over which GB migration becomes energetically favorable, are defined and discussed by staying within the limits of the present model. For λ=0.5, the crossover depth is found to be proportional with $\sigma^{-1/3}$. It is also found that the stress dependence of the incubation time for hillock growth distinguishes between high and low stresses, and is proportional to $\sigma^{-3/2}$ and $\sigma^{-4/5}$, respectively.
5. Since the global Gibbs free energy increases rather than the decrease monotonically, the ridge growth stage is not controlled by Ziegler's 'maximum entropy production principle' [34] but rather by the 'minimum entropy production principle' as postulated by Prigogine [31] for the stationary weakly non-equilibrium states in complex systems, which are now exposed to preset fixed body forces and surface tractions.
6. These results indicate that, the application of bi-axial compressive stresses to the ultra-fine grain poly-crystalline thin films might be a good strategy to develop network of honeycomb shape ridge structures (quasi-quantum rings), which may show strong interface confinement to achieve certain unusual electronic and optical properties due to their particular 3D topology. This type of ridge assembly having almost honeycomb style pattern after the elevated temperature annealing treatment may offer a chance to study the magnetic behavior of susceptibility and the Aharonov-Bohm effect [35].

ACKNOWLEDGEMENTS

The authors wish to thank Professors Şakir Bor and Güngör Gündüz of Middle Technical University (METU) for their constant interest and valuable advice in this project. This work was partially supported by the Turkish Scientific and Technological Research Council, TUBITAK through a research Grant No. 107M011.

REFERENCES

1. Genin FY, Mullins WW, Wynblatt P. The effect of stress on grain boundary grooving. Acta Metall Mater 41 (1993) 3541-3547. doi: 10.1016/0956-7151(93)90234-J
2. Mullins WW. Theory of Thermal Grooving. J Appl Phys 28 (1957) 333. doi: 10.1063/1.1722742
3. Philofsky E, Ravi K, Hall E, Black J. Surface Reconstruction of Aluminum Metallization -- a New Potential Wearout Mechanism. 9th Reliab. Phys. Symp. IEEE, pp 120-128, 1971.

4. Chang CY, Vook RW, Lee YC, Hoshi I. Isothermal annealing of hillocks in Al–Cu films. Thin Solid Films 181 (1989) 57-63. doi: 10.1016/0040–6090(89)90472–0
5. Ericson F, Kristensen N, Schweitz J–A, Smith U. A transmission electron microscopy study of hillocks in thin aluminum films. J Vac Sci Technol B Microelectron Nanom Struct 9 (1991) 58. doi: 10.1116/1.585790
6. Genin FY. Effect of stress on grain boundary motion in thin films. J Appl Phys 77 (1995) 5130. doi: 10.1063/1.359324
7. 7. Genin FY. The initial stages of the formation of holes and hillocks in thin films under equal biaxial stress. Acta Metall Mater 43 (1995) 4289-4300. doi: 10.1016/0956–7151(95)00132–F
8. Genin FY, Siekhaus W. Experimental study to validate a model of hillock's formation in aluminum thin films. J. Appl. Phys. 79 (1996) 3560-3566.
9. Kim D, Nix WD, Vinci RP, Deal MD, Plummer JD. Study of the effect of grain boundary migration on hillock formation in Al thin films. J Appl Phys 90 (2001) 781. doi: 10.1063/1.1381045
10. Chaudhari P. Hillock growth in thin films. J Appl Phys 45 (1974) 4339. doi: 10.1063/1.1663054
11. Presland AEB, Price GL, Trimm DL. Hillock formation by surface diffusion on thin silver films. Surf Sci 29 (1972) 424-434. doi: 10.1016/0039–6028(72)90229–4
12. Hull D, Rimmer DE. The growth of grain–boundary voids under stress. Philos Mag 4 (1959) 673-687. doi: 10.1080/14786435908243264
13. Gao H, Zhang L, Nix WD, Thompson CV, Arzt E. Crack-like grain–boundary diffusion wedges in thin metal films. Acta Mater 47 (1999) 2865-2878. doi: 10.1016/S1359–6454(99)00178–0
14. Zhang L, Gao H. Coupled grain boundary and surface diffusion in a polycrystalline thin film constrained by substrate. Zeitschrift für Met 93 (2002) 417.
15. Barvosa–Carter W, Aziz MJ, Gray LJ, Kaplan T. Kinetically driven growth instability in stressed solids. Phys Rev Lett 81 (1998) 1445-1448. doi: 10.1103/PhysRevLett.81.1445
16. Lahiri SK. Stress Relief and Hillock Formation in Thin Lead Films. J Appl Phys 41 (1970) 3172. doi: 10.1063/1.1659383
17. Ogurtani TO. Unified theory of linear instability of anisotropic surfaces and interfaces under capillary, electrostatic, and elastostatic forces: The regrowth of epitaxial amorphous silicon. Phys Rev B 74 (2006) 1-25. doi: 10.1103/PhysRevB.74.155422
18. Kirchheim R. Stress and electromigration in Al–lines of integrated circuits. Acta Metall Mater 40 (1992) 309-323. doi: 10.1016/0956–7151(92)90305–X
19. Basaran C, Lin M, Ye H. A thermodynamic model for electrical current induced damage. Int J Solids Struct 40 (2003) 7315-7327. doi: 10.1016/j.ijsolstr.2003.08.018
20. Sukharev V, Nix WD, Zschech E. A model for electromigration–induced degradation mechanisms in dual–inlaid copper interconnects: Effect of microstructure. J Appl Phys 102 (2007) 053505. doi: 10.1063/1.2775538
21. Akyildiz O, Oren EE, Ogurtani TO. Grain boundary grooving in bi–crystal thin films induced by surface drift–diffusion driven by capillary forces and applied uniaxial tensile stresses. Philos Mag 92 (2012) 804-829. doi: 10.1080/14786435.2011.634850
22. Ogurtani TO. Mesoscopic nonequilibrium thermodynamics of solid surfaces and interfaces with triple junction singularities under the capillary and electromigration forces in anisotropic three–dimensional space. J Chem Phys 124 (2006) 144706. doi: 10.1063/1.2185625
23. Ogurtani TO, Oren EE. Irreversible thermodynamics of triple junctions during the intergranular void motion under the electromigration forces. Int J Solids Struct 42 (2005) 3918-3952. doi: 10.1016/j.ijsolstr.2004.11.013
24. Ogurtani TO, Akyildiz O. Morphological evolution of voids by surface drift diffusion driven by capillary, electromigration, and thermal–stress gradients induced by steady–state heat flow in passivated metallic thin films and flip chip solder joints. I. Theory. J Appl Phys 104 (2008) 023521. doi: 10.1063/1.2958088
25. Ogurtani TO, Akyildiz O. Morphological evolution of voids by surface drift diffusion driven by the capillary, electromigration, and thermal–stress gradient induced by the steady state heat flow in passivated metallic thin films and flip–chip solder joints. II. Applications. J Appl Phys 104 (2008) 023522. doi: 10.1063/1.2958303
26. Yeremin EN. The Foundations of Chemical Kinetics. MIR Publishers, Moscow, Russia , 1979.
27. Beer G, Watson JO. Introduction To Finite And Boundary Element Methods For Engineers. John Wiley & Sons, New York, USA, 1992.
28. Gear CW. Numerical initial value problems in ordinary differential equations. Prentice–Hall, Englewood Cliffs, N. J., 1971.
29. Pan J, Cocks ACF. A numerical technique for the analysis of coupled surface and grain–boundary diffusion. Acta Metall Mater 43 (1995) 1395-1406. doi: 10.1016/0956–7151(94)00365–O
30. Friesen C. Reversible stress changes at all stages of Volmer-Weber film growth. J Appl Phys 95 (2004) 1011. doi: 10.1063/1.1637728
31. Prigogine I. Introduction to Thermodynamics of Irreversible Processes. Interscience Publishers, New York, USA, 1961.
32. Ogurtani TO, Celik A, Oren EE. Morphological evolution in a strained–heteroepitaxial solid droplet on a rigid substrate: Dynamical simulations. J Appl Phys 108 (2010) 063527. doi: 10.1063/1.3483937
33. Sokolnikoff I. Mathematical Theory of Elasticity. McGraw–Hill Book Co., New York, 1956.
34. Martyushev LM, Seleznev VD. Maximum entropy production principle in physics, chemistry and biology. Phys Rep 426 (2006) 1-45. doi: 10.1016/j.physrep.2005.12.001
35. Aharonov Y, Bohm D. Significance of electromagnetic potentials in the quantum theory. Phys Rev 115 (1959) 485-491. doi: 10.1103/PhysRev.115.485
36. Kröner E. Kontinuums theorie der Versetzungen und Eigenspannungen. Springer, Berlin, 1958.
37. Hong QZ, Zhu JG, Mayer JW, Xia W, Lau SS. Solid phase epitaxy of stressed and stress–relaxed Ge–Si alloys. J Appl Phys 71 (1992) 1768. doi: 10.1063/1.351212
38. Smithells CJ. Metals Reference Book Vol. 3. Butterworths, London, 1967.

Appendix

The elastic dipole tensor concept was first introduced by Late Professor Kröner [36] for the elastic strain field interaction between point defects and the applied stress fields in bulk phases, which may be formulated as $u^{*}_{EDTI} = -\Omega_a \underline{\underline{\bar{\lambda}}} : \underline{\underline{\sigma}}$ The tetrahedral elastic dipole tensor associated with these so-called paraelastic defects may be described by: $\underline{\underline{\lambda}}^{*}_{\hat{q}} = \bar{\lambda}_1 \left[\underline{\underline{I}} + \eta \delta_{(n)q} \delta_{(n)m} \right]$ where $q = 3$ denotes direction of the symmetry axis and $\eta = (\bar{\lambda}_3 - \bar{\lambda}_1)/\bar{\lambda}_1$ is closely related to the shape factor. $\bar{\lambda}_3$, $\bar{\lambda}_1 = \bar{\lambda}_2$ are the principal values of the tetragonal elastic dipole tensor, along the symmetry axis denoted by $\hat{q}$ and in the interface tangent plane (transverse components), respectively. $\delta_{(n)q}$ is Kronecker deltafunction, $\hat{q}$ denotes the direction of the tetragonal axis, which is parallel to the interface normal $\hat{n}$ for the present case, and $(.)$ indicates that the Einsteinsummation rule for the repeated indices is not valid. Then one can easily show that the EDTI energy may be given by the following expression $u^{*}_{EDI} = -\Omega \lambda \underline{\underline{\bar{\lambda}}} : \underline{\underline{\sigma}} = -\Omega \bar{\lambda}_1 (Tr \underline{\underline{\sigma}} + \eta \sigma_{qq})$ for the general stress systems, where $\sigma_{qq} \equiv \hat{q}.\underline{\underline{\sigma}}.\hat{q}$, and it is equal to zero for the traction free surfaces. As a special case; the uniaxial stress system acting in the surface tangent plane in the direction of $\hat{t}$, one can obtain the following expression for EDTI energy: $u^{*}_{EDI} = -\Omega \bar{\lambda}_1 \sigma_{\hat{t}\hat{t}}$, where $Tr\sigma \Rightarrow \sigma_{\hat{t}\hat{t}}$ is called hoop stress in engineering applications. The general formula given previously, clearly shows that one cannot consider the application of the pure hydrostatic stress (whether it is hydrostatic pressure or triaxial tension) $\underline{\underline{\sigma}} = -p\underline{\underline{I}}$ on the composite system (solid/fluid and solid/amorphous), without violating the mostly used traction free boundary conditions. In the case of biaxial stress system acting in the surface tangent plane one can also obtain the following expression for EDTI energy: $u^{*}_{EDI} = -2\Omega \bar{\lambda}_1 \sigma_{\hat{t}\hat{t}}$. This shows that the biaxial in-plane stress has twice the effect of uniaxial stress as confirmed experimentally by Hong et al. [37].

Hittite Journal of Science and Engineering, 2015, 2 (1) 77-83
ISSN NUMBER: 2149-2123
DOI: 10.17350/HJSE19030000011

Recent Tectonic Features of the Central Part (Bolu-Corum) of the North Anatolian Fault

Hakan Yavasoglu[1], Mehmet Nurullah Alkan[2], Ibrahim Murat Ozulu[3], Veli Ilci[3], Fazli Engin Tombus[3], Kayhan Aladogan[2], Murat Sahin[3], Ibrahim Tiryakioglu[4], Serhat Oguzhan Kıvrak[5]
[1] Istanbul Technical University, Department of Geomatics Engineering, Istanbul, Turkey
[2] Hitit University, Department of Map and Cadastre, Osmancik, Corum, Turkey
[3] Hitit University, Department of Map and Cadastre, Corum, Turkey
[4] Afyon Kocatepe University, Department of Geomatics Engineering, Afyonkarahisar, Turkey
[5] Hitit University, Department of Construction Technology, Corum, Turkey

ABSTRACT

After the 1999 Izmit and Düzce earthquakes, the earth science studies increase on the NAF to better understand mechanism and to monitor the motion of it. Monitoring such motion can be achieved by the instrumental tools or techniques like GPS, InSAR, LIDAR, creep meter, etc. The GPS observations showed that while the NW-SE trending section of the NAF between Karlıova and Vezirköprü has nearly strike slip mechanism, the NE-SW trending section of the NAF between Vezirköprü and Bolu has transpressive character. While the fault-parallel velocities have been estimated from just a few GPS vectors available in the region, little is known about the fault-perpendicular component of the regional velocity. The rate of conversion and how it varies along strike are not known due to the sparsely distributed GPS benchmarks in the region. At the same time, the aseismic fault creep determined using InSAR has needed to proof and improve by other techniques and tools. For this propose the new project has been started to determine quantitatively the rate of convergence and its variation along segment of the NAF between Bolu and Çorum. In this study, we focus on the Bolu-Çorum segment of the NAFZ using GPS technique. The main aim of this study is determination of creep rate with geodetic measurements and combination of the data obtained from seismology, geodesy and geophysics to understand fault mechanism. Therefore, in this paper we discuss tectonic phenomena on the central part of the NAFZ and present the first results of the project.

Key Words:
Creep; GPS; Deformation; Nort Anatolian Fault; Earthquake.

Article History:
Received: 2015/05/10
Accepted: 2015/06/17
Online: 2015/07/01

***Correspondence to**: Mehmet Nurullah Alkan, Hitit University, Osmancık Derindere Vocational Higher School, Department of Map and Cadastre ,Osmancik, Çorum, Turkey*
Tel: +90 (364) 611-5029
Fax: +90 (364) 611-50 30
E-Mail: nurullahalkan@hitit.edu.tr

INTRODUCTION

Seismic hazard and loss assessment are important phenomena to save human life. For this purpose, understanding the mechanism of the active fault under tectonic stress is still critical subject [1-2]. The active faults can move abruptly to release the strain accumulation and produce destructive earthquakes or slip continuously (aseismic fault creep) without produce earthquakes significantly. The sudden release of accumulated strain on locked active faults (earthquake) along active faults can be subdivided into four periods: interseismic, preseismic, coseismic, and postseismic. This sequence is called the earthquake cycle in the literature. On the contrary, faults which slip freely can be locked partially ([3] such as Hayward fault [4], the Superstition Hills fault [5], the Longitudinal Valley fault [6], and the Ismetpasa and Destek segments and of the North Anatolian Fault [7-9]. In this subject, the important ıssue is threshold of the aseismic slip rate. If it is equal or larger than long-term slip rate, the destructive earthquakes will not occur along the fault which has aseismic slip rate. On the contrary, if the creep motion is lower than long-term slip rate along the fault, the fault has potential to produce moderate-to-large size earthquakes [9]. Therefore, knowledge and motoring of the aseismic fault creep and also comparing the results with long-

Table 1. List of the earthquakes[26]

Date	*Latitude (°)*	*Longitude (°)*	*Depth (km)*	*Magnitude*
24.11.2013	*40.8205*	*31.8691*	*5.99*	*5.1*
06.06.2000	*40.693*	*32.992*	*10*	*6*
16.11.1999	*40.717*	*31.608*	*10*	*5.1*
05.10.1977	*40.963*	*33.411*	*33*	*5.8*
03.09.1968	*41.86*	*32.463*	*20*	*6.3*
07.09.1953	*40.956*	*33.204*	*10*	*6.1*

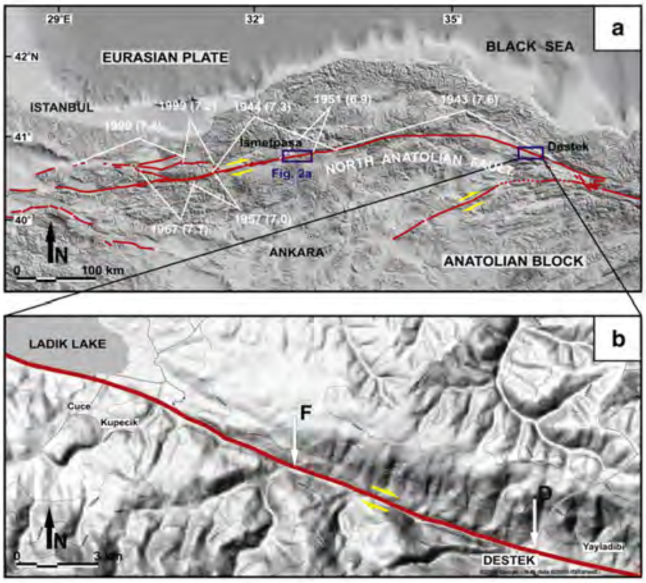

Figure 1. (a) Simplified map of the North Anatolian Fault showing creep locations and recent major earthquakes. (b) General trend of the North Anatolian Fault around Destek segment. "F" and "D" indicate the locations of the surveyed areas in and near Destek (Fig 2b) (after [9]).

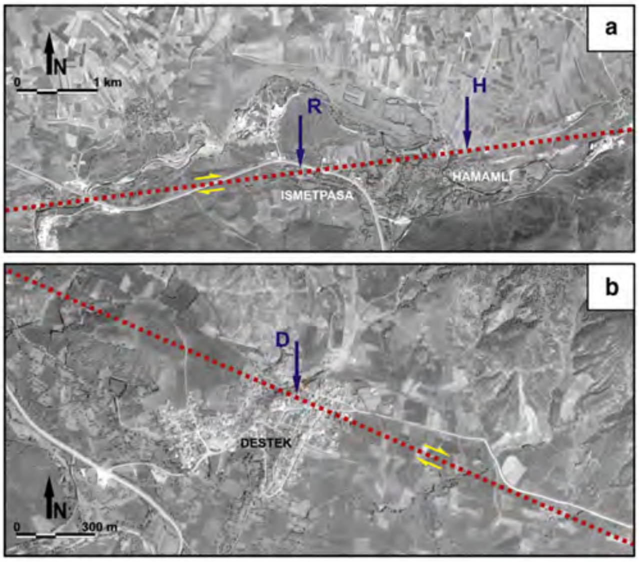

Figure 2. (a) Detailed map of the Ismetpasa. "R" is the railway station in Ismetpasa, "H" is the Hamamlı Village and the dashed line is the trace of the NAF. (b) Detailed map of (D) Destek. The dashed line is the trace of the NAF (after [9]).

term slip rate are critical to prevent loss of seismic hazard.

The Ismetpasa and Destek segments where lie from Bolu the west to Corum the east were ruptured by the earthquakes in 1943 (Tosya Ms=7.6), 1944 (Bolu-Gerede Ms=7.3) and 1951 (Kursunlu Ms=6.9) in the last century (Figure 1 and 2, the list of the other earthquakes are given in Table 1).

Geoscience Studies

In this study, we focus on the central part of the NAF with three sub-segments; Ismetpasa on the west, Destek on the east and central part between east and west boundaries.

Aseismic fault creep on the NAF was firstly reported by Ambraseys [7] at Ismetpasa segment and was calculated the rate of aseismic slip 20 mm/yr using tape meter measurements. After Ambraseys, the first geodetic study was started by establishing triangulation and trilateration network across the fault near Ismetpasa. The geodetic measurements indicate that the rate of creep is 9.3±0.7 mm/yr [10] and 7.8±0.5 mm/yr [11]. Using InSAR technique, Cakir et al., [8] estimated the rate 8±3 mm/yr for the creeping on the section. The LIDAR technology was also used

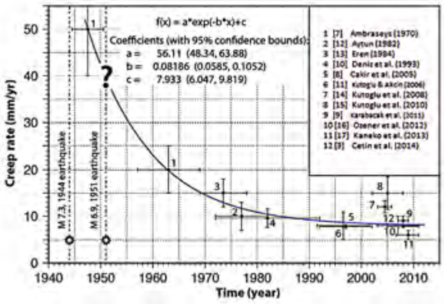

Figure 3. Time history of surface creep at Ismetpasa as reported by various studies following the 1944 earthquake (after [3]). Horizontal and vertical bars are the time window and error range of measurements, respectively. The question mark corresponds to the unknown effect of the 1951 earthquake on creep rate. Curve shows the fit of the exponential relaxation function to the change of the creep rate with time [18].

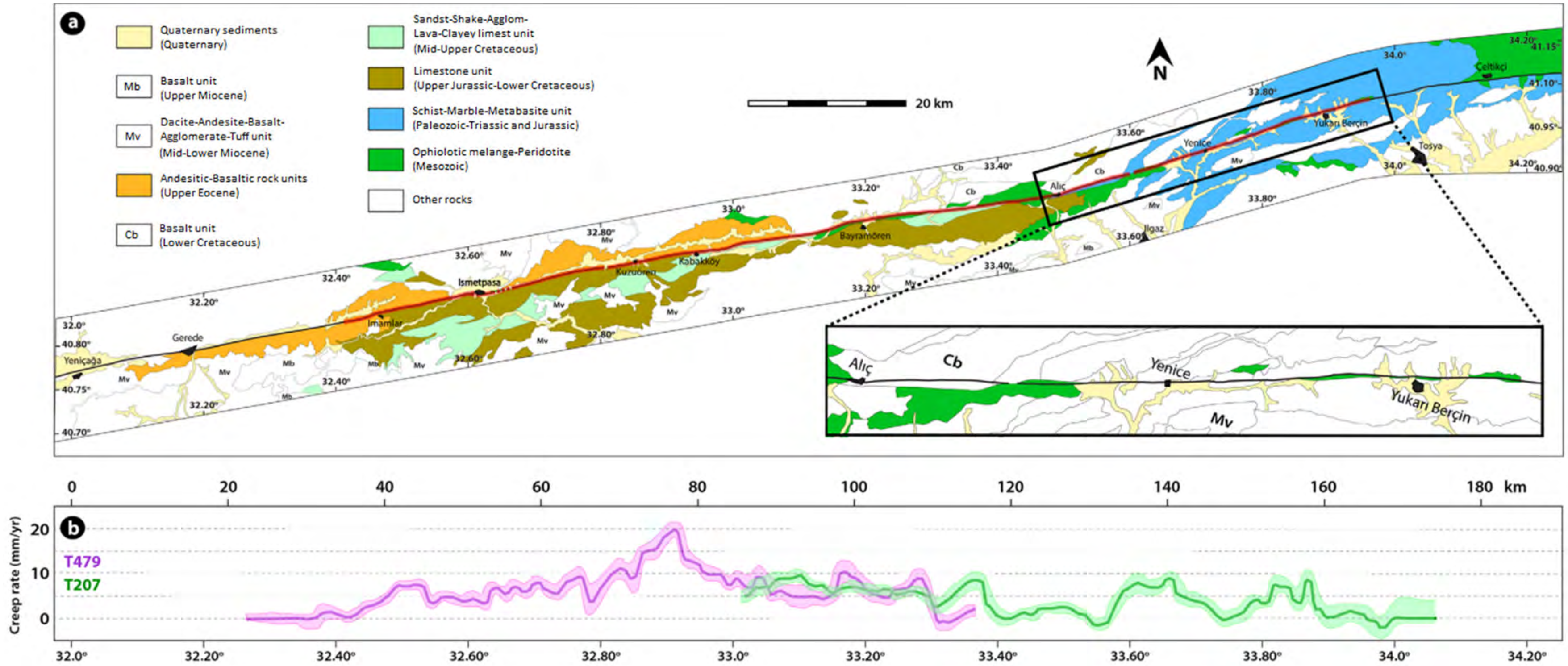

Figure 4. (a) Geology map of the study region. Geological units presumably involved in creeping are shown in colors and the others are labeled in white with abbreviations. Black and red lines represent the active fault and the creeping segment, respectively. The eastern end of the creeping section can be clearly seen in the inset rectangle. (b) Creep rates and error ranges for two individual tracks are indicated in purple (track T479) and green colors (track T207) (after [3]).

by Karabacak et al. (2011) [9] to calculate the rate of 6.8–10.0±4.0 mm/yr and 9.1–10.1±4.0 mm/yr. Cakir et al., (2012) [2] and Cetin et al., (2014) [3] reported that the rate is not stable along the fault and reaches a maximum of 20±2 mm/yr 20km to the east from Ismetpasa (Figure 3 and 4).

Another aseismic creep segment on the NAF was reported by Karabacak et al. (2011) [9] in Destek village on the northeast of the Corum. This segment of the NAF was ruptured in 26 November 1943 Tosya (Ms=7.6) earthquake. LIDAR results on this part of the fault showed an aseismic slip rate of 6.0–7.2±4.0 mm/yr, which releases considerable amount of strain in this part of the NAF but the results of the LIDAR measurements were not verified by the another techniques, observations or studies. This can be a handicap to explain the behavior of the fault in this segment.

The central part of the NAF in our study area, where no another aseismic surface slip section reported by previous studies. At the same time, Yavasoğlu et al. (2011) [19] and Peyret et al. (2013) [20] indicate that the central part of the NAF in between Destek and Ismetpasa are still active and going on strain accumulation with slip rate 20.5 ± 1.8 mm/yr.

DISCUSSIONS

The long term-slip rate is important issue in active tectonic studies to compare with aseismic slip rate and to understand the behavior of the active faults. The GPS is an accurate and economic tool to calculate the long-term slip rate for active faults. As explained in the previous section, the valuable studies have been published, except global and local GPS measurements for the central part of the NAF excluding studies that show general global slip rate, [19-22].

In this project, five profiles shaped GPS networks across the fault are established to determine local movement such as aseismic slip rate or creeping according to model (Figure 5).

Four profiles were established in Ismetpasa segment and one for Destek region. Each profile has eight force-centered stations located approximately from the north to the south and almost perpendicular to the fault on the profiles (Figure 6a, 6b and 6c).

We also combine the creeping and non-creeping sections of the NAF using continuous GPS sites (CORS-TR) (Figure 7).

CONCLUSIONS

The new geodetic network with 43 stations was established to monitor the creep and non-creep sections of the NAF. The first GPS campaign was carried out in August 2014 (on GPS days; 235, 236, 237, 238 and 241) with 5 second sample interval and 15 degree elevation mask. The first campaign data both obtained from new 43 sites and 48 continuous GPS stations (IGS and CORS-TR) was evaluated by GAMIT/GLOBK software [23].

Pseudo-range and phase GPS data are analyzed using GAMIT software as single-day solutions. Station coordinates, satellite orbits, 13 tropospheric zenith delay parameters per site and phase ambiguities using doubly-differenced phase measurements are solved while applying loose a priori constraints to all parameters.

The IGS final orbits, IERS earth orientation parameters are used, and azimuth and elevation dependent antenna phase center models are applied.

After the second and third campaigns, the project will be valuable. The similarities and differences in seismological behavior of the NAF along its creeping and non-creeping sections will be investigated for the first time in this project. It is an important shortcoming that such an investigation has not been conducted yet even though the phenomenon of surface creep in Ismetpasa has been known for over 40 years and in Destek discovered recently. Creeping section of the San Andreas Fault at Hayward has been monitored using micro geodetic and seismic networks for many years, which have revealed important information about the rheology and temporal behavior of the fault and its potential for producing earthquakes [24]. This will be the first study on the seismic characteristics of the creeping section of the NAF.

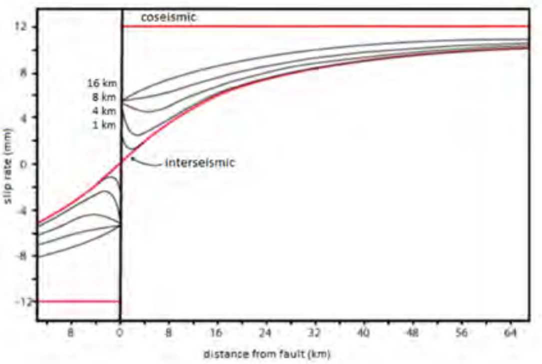

Figure 5. Black lines show creep model in different locking depth from 1km to 16km. Red lines show the interseismic and coseismic behavior without creeping.

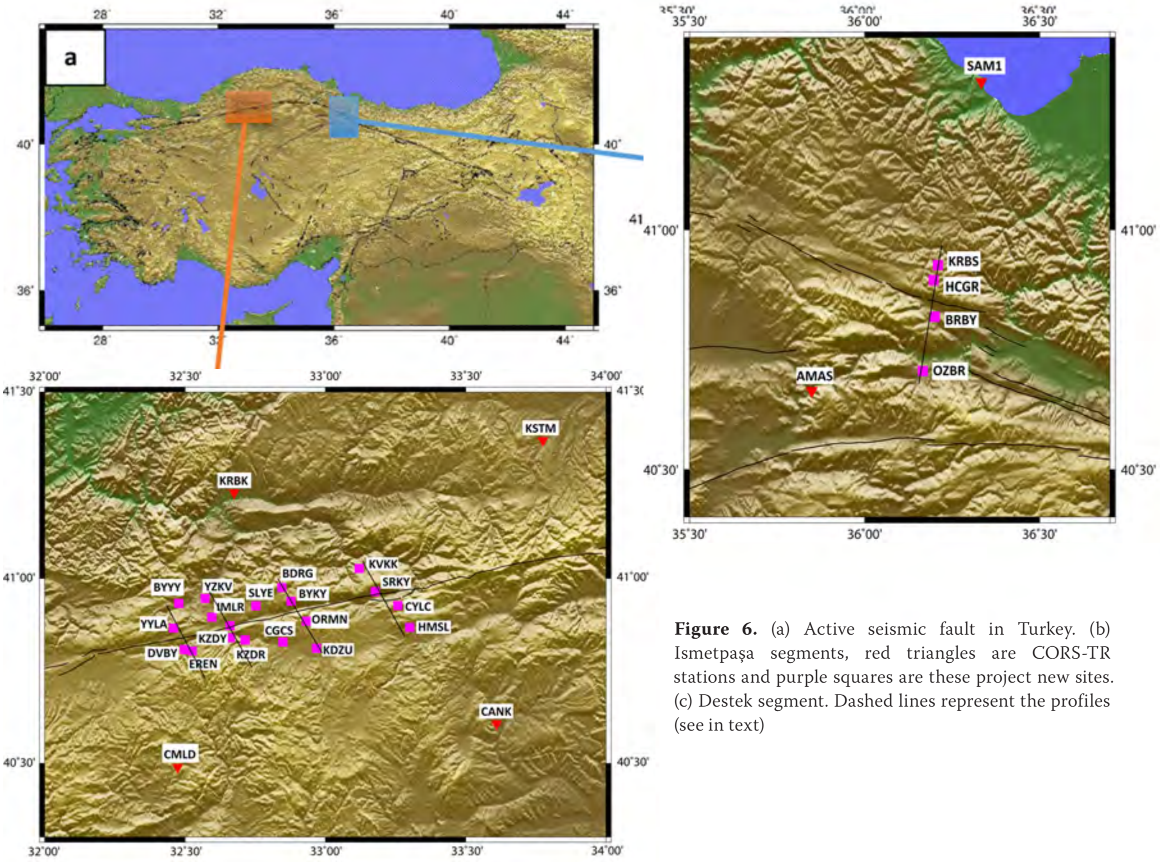

Figure 6. (a) Active seismic fault in Turkey. (b) Ismetpaşa segments, red triangles are CORS-TR stations and purple squares are these project new sites. (c) Destek segment. Dashed lines represent the profiles (see in text)

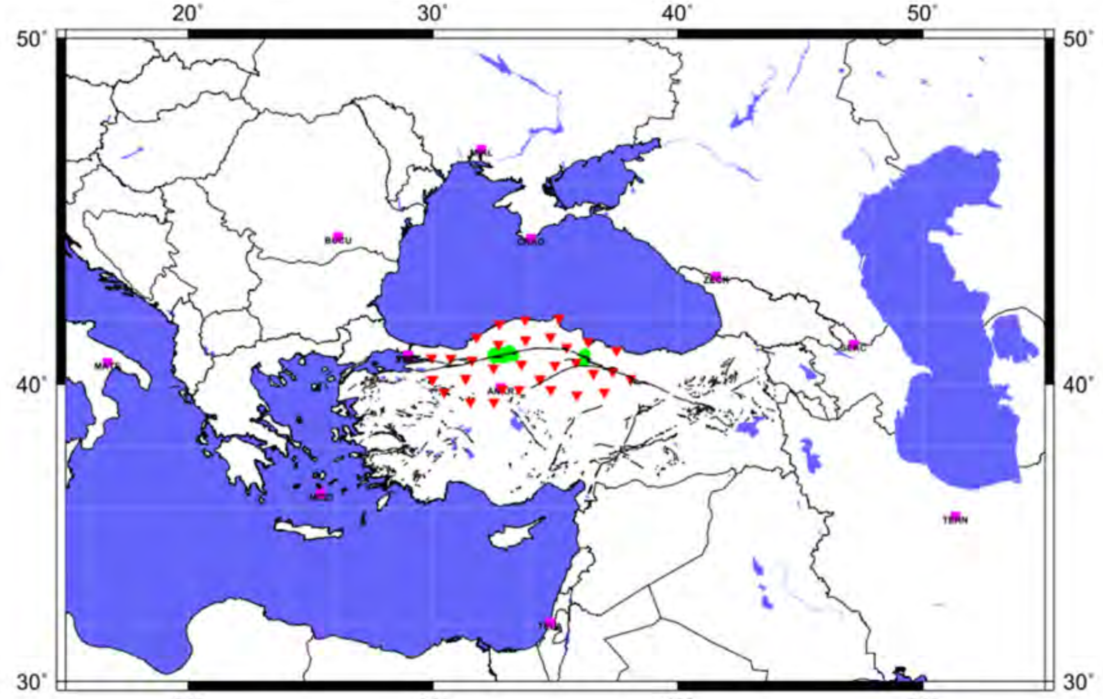

Figure 7. Green circles are new GPS sites, red reverse triangles for CORS-TR sites, and purple squares are IGS GPS stations..

ACKNOWLEDGEMENT

We would like to thank to Prof. Dr. Reha Metin Alkan the Rector of Hitit University. Financial supports of the projects are from Hitit University Fund and Istanbul Technical University Fund with numbers, MYO19001.14.001 and 38146, respectively. The figures in this paper were generated using the public domain Generic Mapping Tools (GMT) software [25]. We thank to Afyon Kocatepe University (Dr. Saffet Erdogan, MSc. Mehmet Ali Ugur).

REFERENCES

1. Carpenter BM, Marone C, Saffer DM. Weakness of the San Andreas Fault revealed by samples from the active fault zone. Nature Geoscience 4 (2011) 251-254.
2. Cakir Z, Ergintav S., Ozener H, Dogan U, Akoglu AM, Meghraoui M,Reilinger R. Onset of aseismic creep on major strike–slip faults. Geology 40(12) (2012) 1115-1118.
3. Cetin E, Cakir Z, Meghraoui M, Ergintav S, Akoglu AM. Extent and distribution of aseismic slip on the Ismetpasa segment of the North Anatolian Fault (Turkey) from Persistent Scatterer InSAR. Geochemistry Geophysics, Geosystems 15 (2014) 2883–2894.
4. Schmidt DA, Bürgmann R, Nadeau RM, d'Alessio M. Distribution of aseismic slip–rate on the Hayward fault inferred from seismic and geodetic data. Journal of Geophysical Research 110 (2005) B08406 doi:10.1029/2004JB003397.
5. Wei M, Sandwell D, Fialko Y. A silent M4.8 event of October 3–6, 2006, on the Superstition Hills Fault, Southern California. Journal of Geophysical Research 114 (2009) B07402, doi:10.1029/2008JB006135.
6. Thomas MY, Avouac JP, Champenois J, Lee JC, Kuo LC. Spatio–temporal evolution of seismic and aseismic slip on the Longitudinal Valley Fault, Taiwan. Journal of Geophysical Research 119 (2014) 5114–5139.
7. Ambraseys NN. Some characteristic features of the Anatolian fault zone. Tectonophysics 9 (1970) 143-165.
8. Cakir Z, Akoglu AM, Belabbes S, Ergintav S, Meghraoui M. Creeping along the Ismetpasa section of the North Anatolian Fault (Western Turkey): Rate and extent from InSAR. Earth and Planetary Science Letters 238 (2005) 225-234.
9. Karabacak V, Altunel E, Cakir Z. Monitoring aseismic creep along the North Anatolian Fault (Turkey) using ground–based LIDAR. Earth and Planetary Science Letters 304 (2011) 64-70.
10. Deniz R, Aksoy A, Yalin D, Seeger H, Hirsch O, Bautsch P. Determination of crustal movement in Turkey by terrestrial geodetic methods. Journal of Geodynamics 18 (1993) 13-22.
11. Kutoglu HS, Akcin H. Determination of 30–year Creep on the Ismetpasa segment of the North Anatolian Fault using an old geodetic network. Earth Planets Space 58 (2006) 937-942.
12. Aytun A. Creep measurements in the Ismetpasa region of the North Anatolian Fault Zone, in Multidisciplinary Approach to Earth–quake Prediction edited by Isikara AM and Vogel A vol. 2 (1982) 279-292 Friedr. Vieweg & Sohn, Braunschweig Germany.
13. Eren K. Strain analysis along the North Anatolian fault by using geodetic surveys. Bulletin Géodésique 58 (1984) 137-149.
14. Kutoglu HS, Akcin H, Kemaldere H, Gormus KS. Triggered creep rate on the Ismetpasa segment of the North Anatolian Fault. Natural Hazards & Earth System Sciences 8 (2008) 1369-1373.
15. Kutoglu HS, Akcin H, Gundogdu O, Gormus KS, Koksal E. Relaxation on the Ismetpasa segment of the North Anatolian Fault after Golcuk Mw 5 7.4 and Duzce Mw 5 7.2 shocks. Natural Hazards Earth System Sciences 10 (2010) 2653-2657.
16. Ozener H, Dogru A, Turgut B. Quantifying aseismic creep on the Ismetpasa segment of the North Anatolian Fault Zone (Turkey) by 6 years of GPS observations. Journal of Geodynamics 67 (2012) 72-77.
17. Kaneko Y, Fialko Y, Sandwell DT, Tong X, Furuya M.Interseismic deformation and creep along the central section of the North Anatolian fault (Turkey): InSAR observations and implications for rate–and–state friction properties. Journal of Geophysical Research 118(1) (2013) 316–331.
18. Savage JC., Svarc JL., and Yu SB. Postseismic relaxation and transient creep. Journal of Geophysical Research 110(B11) (2005) doi:10.1029/2005JB003687.
19. Yavasoglu H, Tari E, Tuysuz O, Cakir Z, Ergintav S. Determining and modelling tectonic movements along the central part of the North Anatolian Fault (Turkey) using geodetic measurements. Journal of Geophysical Research 51(5) (2011) 339-343.
20. Peyret M, Masson F, Yavasoglu H, Ergintav S, Reilinger R. Present–day strain distribution across a segment of the central bend of the North Anatolian Fault Zone from a Persistent–Scatterers InSAR analysis of the ERS and Envisat archives. Geophysical Journal International 192(3) (2013) 929–945.
21. McClusky S, Balassanian S, Barka A, Demir C, Ergintav S, Georgiev I, Gurkan O, Hamburger M, Hurst K, Kahle H, Kastens K, Kekelidze G, King R, Kotzev V, Lenk O, Mahmoud S, Mishin A, Nadriya M, Ouzounis A, Paradissis D, Peter Y, Prilepin M, Reilinger R, Sanli I, Seeger H, Tealeb A, Toksoz MN, Veis G. Global Positioning System constraints on plate kinematics and dynamics in the eastern Mediterranean. Journal of Geophysical Research 105 (2000) 5695-5719.
22. Reilinger R, McClusky S, Vernant P, Lawrence S, Ergintav S, Cakmak R, Ozener H, Kadirov F, Guliev I, Stepanyan R, Nadariya M, Hahubia G, Mahmoud S, Sakr K, ArRajehi A, Paradissis D, Al–Aydrus A, Prilepin M, Guseva T, Evren E, Dmitrotsa A, Filikov SV, Gomez F, Al–Ghazzi R, Karam G. GPS constraints on continental deformation in the Africa-Arabia, Eurasia continental collision zone and implications for the dynamics of plate interactions. Journal of Geophysical Research Earth 111 (2006) doi: 10.1029/2005JB004051.
23. King RW, Bock Y. Documentation for the GAMIT GPS Analysis Software Release 10.1 (2003) Massachusetts Institute of Technology, Cambridge MA, USA.
24. Titus SJ, DeMets C, Tikoff B. Thirty–Five–Year Creep Rates for the Creeping Segment of the San Andreas Fault and the Effects of the 2004 Parkfield Earthquake: Constraints from Alignment Arrays, Continuous Global Positioning System, and Creepmeters. Bulletin of the Seismological Society of America 96(4B) (2006) 250–268.

25. Wessel P, Smith WHF. New improved version of Generic Mapping Tools released. Eos Transactions American Geophysical Union 79(47) (1998) 579.

26. http://earthquake.usgs.gov (Last viewed: 17.06.2015)

Hittite Journal of Science and Engineering, 2015, 2 (1) 85-90
ISSN NUMBER: 2149-2123
DOI: 10.17350/HJSE19030000012

A New Generation, Promising Engineering Material: Cubic Boron Nitride (c-BN)

Baris Cetin[1], Hakan Kaplan[2] and Goksel Durkaya[2]
[1] FNSS Defense Systems Co. Inc., Senior Materials & Special Processes Engineer, B.S., Ankara, TURKEY
[2] Atilim University, Department of Metallurgical and Materials Engineering, Nanoscopy Lab., Ankara, TURKEY

ABSTRACT

In order to meet the design requirements and expanding demands in various engineering fields, it is essential to incorporate new technological improvements in material sciences into existing processes and applications. This involves engineering new material systems and improving existing ones towards higher strength, toughness and wear resistance. In this context, cubic boron nitride (c-BN), which is a special polymorph of boron nitride, seems to be a high-potential candidate for engineering solutions due to its great mechanical and chemical properties. In this article, advantages and disadvantages of c-BN material system are presented with respect to our ongoing research efforts. The preliminary results about the characterization study of thin film c-BN coatings with Raman spectroscopy are also presented.

Article History:
Received: 2015/05/12
Accepted: 2015/06/17
Online: 2015/07/01

***Correspondence to**: Baris Cetin,*
FNSS Defense Systems Co. Inc., Senior Materials & Special Processes Engineer,
Ankara, Turkey
Tel: +90 (312) 497-4619
Fax: +90 (312) 497-4301
E-Mail: cetin.baris@fnss.com.tr

Key Words:
Cubic Boron Nitride; Wear Resistance; Raman Spectroscopy.

INTRODUCTION

Because of its high mechanical, chemical and tribological properties and its potential on improving tool parts, c-BN material system attracts major research interest. c-BN has a very high hardness value (45 GPa Knoop) and has a potential to exceed that of diamond if it is understood and engineered at the microstructural level. It does not react with ferrous metal and oxygen even at high temperatures besides of its high thermal conductance and electrical resistance. Chemical stability towards ferrous metals and oxygen at high temperatures such as 1300°C, is a field that c-BN surpasses the diamond [1-3]. It was observed that when a fragment of c-BN was twice heated over 2000°C in vacuum, the material was not attacked by any of the usual acids and was only slowly oxidized in air at 2000°C [4]. By means of its great properties, c-BN is being used in production of tool steels with powder metallurgy or coating of them by PVD, coating of die steels in sheet metal forming or direct applications to final product where high wear resistance is needed [5-6]. Furthermore its antibacterial behavior creates opportunities for biomedical applications [7].

Polymorphs of BN

BN exists in nature with different polymorphs. Due to the specific bonding behavior of boron and nitrogen atoms, BN exists in many different structures. The well-known four polymorphs of BN are cubic (c-BN), hexagonal (h-BN), rhombohedral (r-BN) and wurtzite (w-BN). The variety of interesting properties of boron-nitrogen materials are closely related to their crystal structures. For example c-BN is a hard material, and its mechanical, thermal, and electronic properties are similar to diamond. On the contrary, h-BN is a soft material, whose softness comes from its layered hexagonal crystal structure, similar to graphite; therefore, h-BN is known also as "white graphite" [8-9]. Crystal structure information for the primary crystalline boron nitride phases are given in Table 1 [10].

As it is discussed, different polymorphs of BN such as c-BN and h-BN exhibit different mechanical properties. In comparison of both polymorphs, c-BN coatings have higher hardness while h-BN coatings yield better self-lubricating properties.

Table 1. Structural Data for Boron Nitride Phases

Phase	*a (A°) [18]*	*c (A°) [18]*	*Space Group*	*Atom Positions*
h-BN [19]	*2.5043*	*6.6562*	$P6_3/mmc$ *(194)*	*B: (0,0,0), (2/3,1/3,1/2)* *N: (2/3,1/3,0), (0,0,1/2)*
r-BN [20]	*2.5042*	*9.99*	*R3m* *(160)*	*B: (0,0,0), (2/3,1/3,1/3), (1/2,2/3,1/3)* *N: (2/3,1/3,0), (1/3,2/3,1/3), (0,0,2/3)*
c-BN [1,21]	*3.6153*		*F43m* *(216)*	*B: (0,0,0), (1/2,1/2,0), (0,0,1/2), (1/2,0,1/2)* *N: (1/4,1/4,1/4), (3/4,3/4,1/4), (1/4,3/4/,1/4), (3/4,1/4,3/4)*
w-BN [21,22]	*2.5505*	*4.210*	$P6_3/mmc$ *(186)*	*B: (0,0,0), (1/3,2/3,1/2)* *N: (0,0,3/8), (1/3,2/3,7/8)*

Therefore, c-BN is better solution in case of tool steel coating while h-BN is better choice where lubrication is an issue. This necessitates improved control over polymorph compositions for the specific purpose. In other words, it is a crucial issue for deposition of film coating to assure the content of desired polymorph and make the necessary characterization operations in order to evaluate the results. Volumetric percentage of c-BN, h-BN and others polymorphs in the resultant coating may alter hugely by small changes in deposition process parameters or material combinations. The higher is the c-BN content, the harder the resultant coating will be. It is not that much easy but possible to obtain BN coatings whose c-BN content is nearly %90. On the other hand, it should be taken into account that, adhesion is also a crucial subject. The most performant coating is not the one which has the highest c-BN content, i.e. strength and hardness. For instance, a coating with high hardness but low adhesion may not result in high machining performance [11]. In order to reach the most performant point, c-BN content and adhesion should be sufficiently good at the same time. Existence of high intrinsic stress in coating has a high potential in perturbing the adhesion of thin film.

Intrinsic Stress Problem of c-BN

The major disadvantage of c-BN is the high intrinsic stress values if a standard PVD (Physical Vapor Deposition) process is applied and a critical thickness (approximately 500 nanometer) is exceeded. This intrinsic stress which occurs between the substrate and thin film could reach up to very high levels such as 20 GPa. This huge amount of stress may lead to crack formation or peeling-off of the thin film [12]. One of the basic reasons for formation of intrinsic stress is the epitaxial interactions and different coefficients of thermal expansion of the substrate and coating material [13]. In the literature, it is proven that by means of special methods and processes like sequential growth, ion reduced stress relief, annealing, sputter cleaning, etc., c-BN films could be created with a 0,5 GPa intrinsic stress and a 1,3μm thickness [14]. In Figure 1, intrinsic stress – time graphs for medium energy simultaneous implantation technique is illustrated as example.

Utilization of complex cyclic process of sputter cleaning, growth, ion radiation induced stress relaxation and annealing might also give good and low-stress results. This process is illustrated in Figure 2 using the transverse optical (TO) Fourier transform infrared (FTIR) line position of c-BN as an indicator for the averaged stress in the growing film [15].

A very good alternative for the creation of stress-free c-BN films is the fluorine based CVD (Chemical Vapor

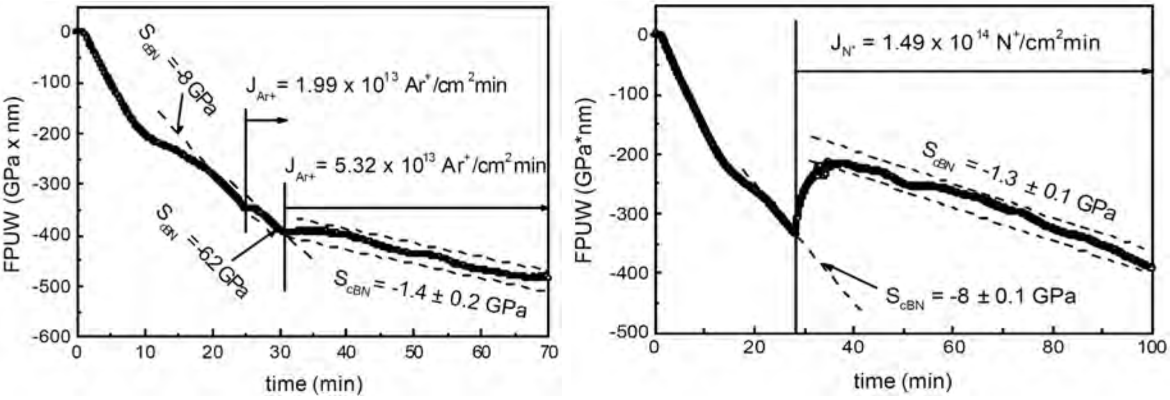

Figure 1. a) Stress-relief of c-BN by simultaneous Argon implantation during deposition, b) Stress-relief of c-BN by simultaneous Nitrogen implantation during deposition [11].

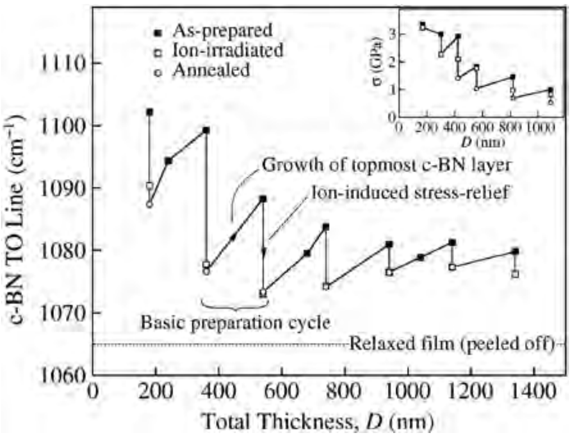

Figure 2. Cyclic PVD deposition process of c-BN

Deposition) application. With this special process, the critical ion energy level which is needed for the nucleation of c-BN can be decreased reasonably. As a result of the lower ion-bombardment energy, intrinsic stress might be reduced to ~1-2 GPa and the films show good adhesion with substrate and long-term stability [15]. However, CVD has also an important disadvantage of high operating temperatures. This high temperatures may cause some thermal softening or recrystallization of the substrate which can highly effect its hardness and toughness. Therefore, some optimization should be made among the deposition methods and also the operating parameters in order to obtain a c-BN coating which is desired.

Characterization of BN Coatings

There are several methods in the characterization of thin films such as FTIR spectrometry, Raman spectroscopy, X-Ray diffraction, and etc. Performing characterization tests is essential for deposition process since the final content of the film is barely dependent to operation parameter, substrate material, and etc. In order to assure the repeatability of the deposition or create any correlation between the operating parameters and content of the resultant film, it would be better to make characterization with minimum two methods. With the characterizations of thin films, deposition processes should be verified.

The characterization of c-BN is a challenging task because c-BN films could be very small-grained and highly defective [10]. It should also be noted that while working with very thin films like 40-50 nanometer, the penetration depth in other words the wavelength of the input light is very important. When the penetration depth goes superior to coating thickness, the spectroscopy analysis would also give information not only about the coating s but also about the substrate material.

Raman spectroscopy is a non-destructive testing method that is used to determine chemical composition and molecular strain in materials by utilizing photon vibration frequencies. Raman spectroscopy with its small wavelength (~532 nm) has a great advantage in thin film characterization with proper optical penetration depth. If the characteristic Raman shift values of a specific molecule is defined previously, then it can easily be detected by measurements.

In the field of BN coatings, the standard frequency shifts (Raman peaks) of the polymorphs are designated in the literature in a detailed manner. Therefore, the volumetric composition of any BN coating could be determined or computed by means of confirm Raman spectroscopy analysis.

There is a collaborative study between Atilim University, Nanoscopy Laboratory and FNSS Defense Systems Inc. which focuses on micro and nano characterization of BN

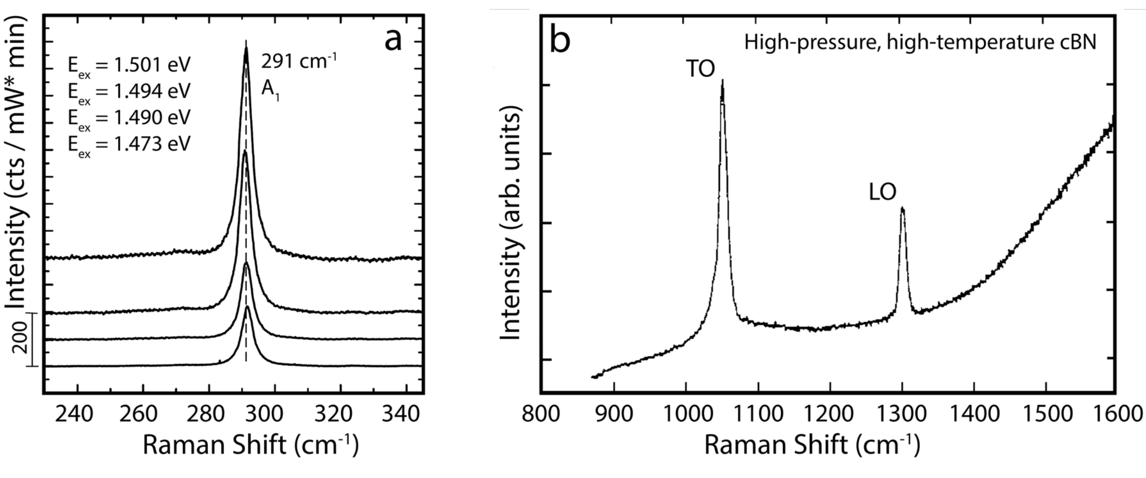

Figure 3. a) Raman spectra of a Cu-rich prepared $CuInS_2$ sample [16], b) Raman spectra of commercial sintered c-BN HTHP [10].

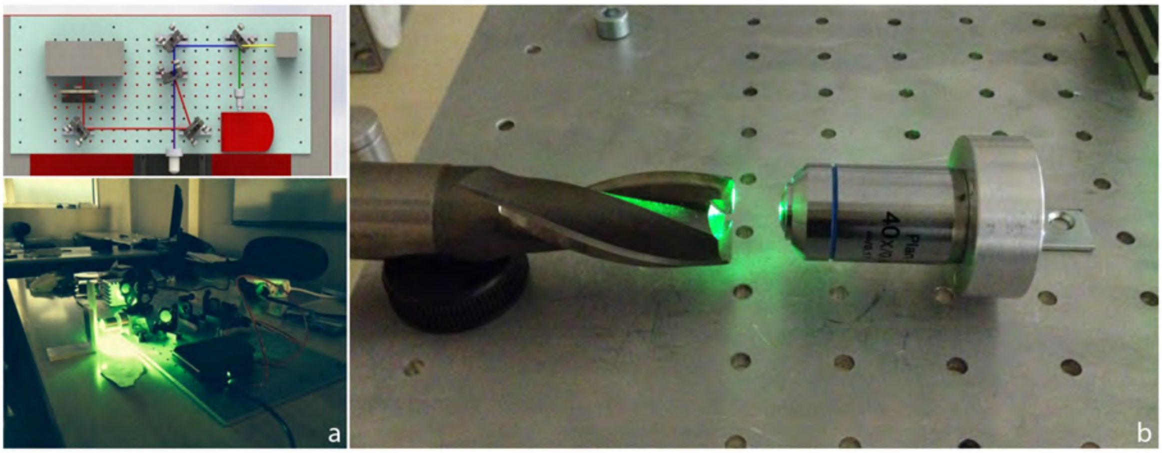

Figure 4. a) Design and prototype of the BN Raman spectrometer at the Atilim University Nanoscopy Lab., b) Raman measurement on the BN coated cutting tool.

coatings on tool parts. A novel Raman spectrometer has been designed specializing only on analysis of BN coated tool parts. As software and hardware development of the system still continues, the preliminary results on BN coated cutting tools (end mill cutters) using Raman spectroscopy is shown in the Figure 4. The end mill cutter studied here was made from high speed steel (HSS) and it was coated with BN using RF magnetron sputtering technique after ultrasonic cleaning process.

In Figure 4a, design and prototype of the BN Raman spectrometer is shown. Optical and mechanical design has been completed and the measurements have been initiated as shown in Figure 4b. The preliminary results on a cutting tool using Raman spectroscopy is shown in the Figure 5 with the calibration data. In Figure 5.a, PDMS polymer was measured using 532 nm excitation wavelength. The calibration data shows proper calibration of the spectrometer with clear signatures matching with the standards. In Figure 5b, the first measurement on a cutting tool coated with BN is shown. The first results show that possible fluorescent background should be eliminated by changing c-BN coating parameters in order to obtain better signal to noise ratio to study phonon signatures shadowed. While main phonon modes for BN system are known from the literature, many others relating to interfacial and chemical phases are also needed to be investigated in order to understand the mechanisms contributing to fluorescent background and low signal to noise ratio. We expect they might originate to multiple reasons including chemical phases on the interface, metal oxides and material defects. Further studies are ongoing in order to elucidate their real behavior on the coated systems.

CONCLUSIONS

c-BN systems promise high potential on improving mechanical and thermal properties of the tool parts as well as the wear resistance. In order to unleash its true potentials there are many challenges to overcome its growth where understanding of its microstructural properties becomes rather important. In this study, we have developed a custom Raman spectrometer specially designed for BN coating characterization in order to understand behavior of its molecular level dynamics in relation to macro scale properties. The calibration data shows proper calibration of the Raman spectrometer system with clear standard signatures obtained from the test sample. Our first result on a cutting tool shows not only phonon signatures may be present but also fluorescent background is observed which may be attributed to many origins including interfacial effects, chemical phases and material defects. Further studies are ongoing in order to understand the real behavior relating to micro scale dynamics of the BN coatings on tool parts.

REFERENCES

1. Prouch JJ, Alterovitz SA. Synthesis and Properties of Boron Nitride. Materials Science Forum 54–55 (1990).
2. Will G, Perkins PG. Is There a New Form of Boron Nitride with Extreme Hardness?. Diamond and Related Materials 10 (2001) 2010–2017.
3. Audronis M, Valiulis AV, Silickas P. Recent Developments in the Deposition of c–BN Coatings. Materials Science (MEDŽIAGOTYRA) 10 (2004) 152–156.
4. Wentrof RH. Cubic Forms of Boron Nitride. Journal of Chemical Physics 26 (1957) 956.

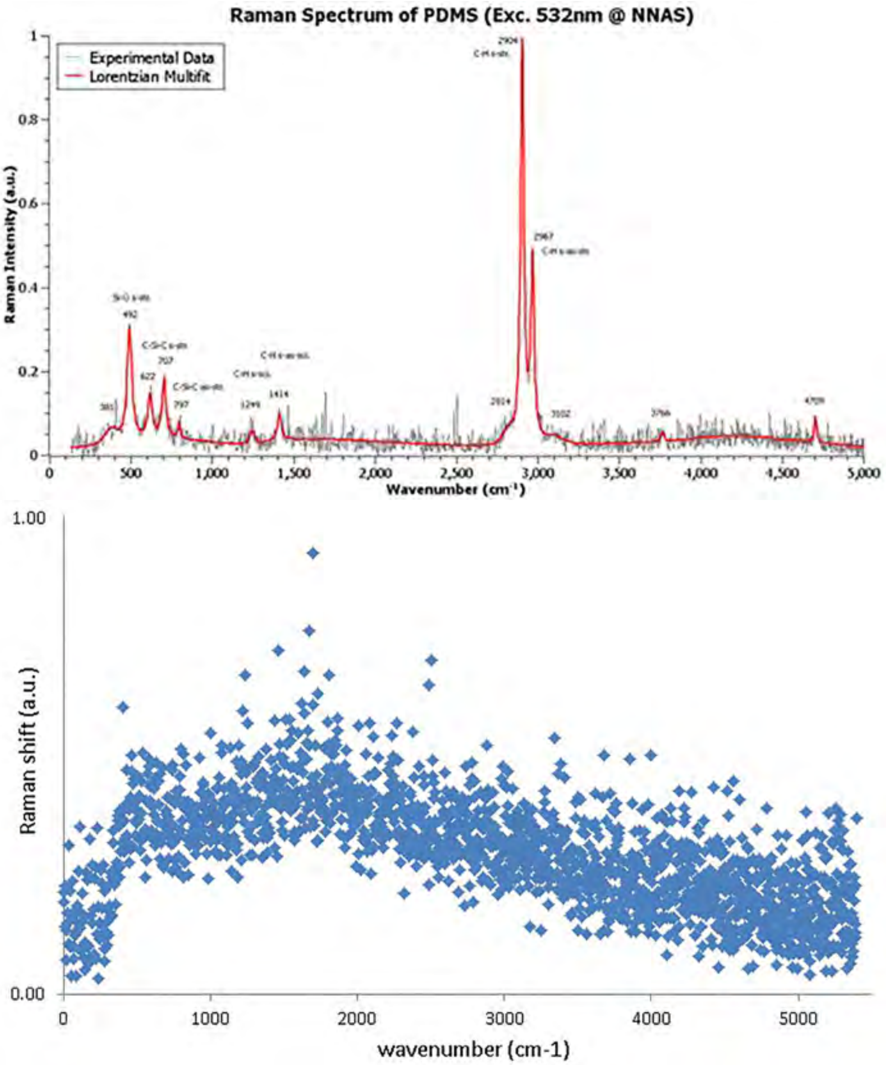

Figure 5. a) PDMS polymer measurement used for calibration, b) Raman Spectra of BN which was coated on cutting tool (First result at Nanoscopy Lab.).

5. Neo KS, Rahman M, Li XP, Khoo HH, Sawa M, Maeda Y. Performance Evaluation of Pure c-BN Tools for Machining of Steel. Journal of Materials Processing Technology 140 (2003) 326–331.
6. http://sheetmetal.me/tooling-terminology/brake-press-tooling/
7. Uzunoglu Emel et al. Antibacterial Activity of Cubic Boron Nitride (cBN) Coatings on Stainless Steel Grade 316 (316L). Abstract of Papers of the American Chemical Society Vol. 240.
8. Zhigadlo ND. Crystal Growth of Hexagonal Boron Nitride (hBN) from Mg-B-N Solvent System under High Pressure. Journal of Crystal Growth 402 (2014) 308–311.
9. Cesur H, Kaftanoglu B, Kalkanli A, Oral B. Deposition of Boron Nitride Coatings on Steel Subtrates by RF Magnetron Sputtering. Proceedings of the 7th International Conference on Coatings, Thessaloniki, Greece, September 2008.
10. Mirkarimi PB, McCarty KF, Medlin DL. Review of Advances in Cubic Boron Nitride Film Synthesis. Materials Science and Engineering 21 (1997) 47–100.
11. Fitz C, Kolitsch A, Fukarek W. Growth of Low Stress Cubic Boron Nitride Films by Simultaneous Medium Energy Implantation. Annual Report IIM, FZR 314 (2000) 31–34.
12. Çetin B, et al. Tool Life Improvement of End mill Cutters with BN Caoting by PVD Method. Proceedings of 8th International Conference and Exhibition on Design and Production of Machines and Dies/Molds, Aydın, Turkey, June 2015.
13. Waters P. Stress Analysis and Mechanical Characterization of Thin Films for Microelectronics and MEMS Applications. Ph.D. Dissertation, University of South Florida, 2008
14. Boyen HG, Widmayer P, Schwertberger D, Deyneka N, Ziemann P. Sequential Ion-Induced Stress Relaxation and Growth: A Way to Prepare Stress-relieved Thick Films of Cubic Boron Nitride. Appl. Phys. Lett. 76 (6) (2000) 709–711.

15. Zhang WJ, Bello I, Lifshitz Y, Lee ST. Recent Advances in Cubic Boron Nitride Deposition. MRS Bulletin 28 (2003) 184–188.

16. Thomas R. Raman Spectroscopy for the Anaylsis of Thin $CuInS_2$ Films. Dissertation, Der Fakultat II der Technischen Universitat Berlin 2002.

Hittite Journal of Science and Engineering, 2015, 2 (1) 91-96
ISSN NUMBER: 2149-2123
DOI: 10.17350/HJSE19030000014

Synthesis, Spectroscopic and Thermal Characterization of Non-Metal Cation (NMC) Pentaborates Salts Containing 2-amino-5-nitropyridine and 2-amino-6-methylpyridine as Cation

Ümit Sizir, Dursun Ali Kose and Omer Yurdakul
Hitit University, Department of Chemistry, Corum, TURKEY

Article History:
Received: 2015/05/18
Accepted: 2015/06/09
Online: 2015/07/01

***Correspondence to**: Dursun Ali Kose,*
Hitit University, Faculty of Arts and Science,
Department of Chemistry, Corum, Turkey
Tel: +90 (364) 227-7000
Fax: +90 (364) 227-7005
E-Mail: dalikose@hitit.edu.tr

ABSTRACT

The pyridine derivatives, 2-amino-5-nitropyridine and 2-amino-6-methylpyridine (6-aminopicolin), were used for the synthesis of two new non-metal cation (NMCs) pentaborate structures. The NMCs pentaborate molecules were characterized using ^{11}B-NMR, elemental analysis, BET, FT-IR, P-XRD and melting point technics. The thermal properties had been investigated by TGA/DTA/DTG methods. 2-amino-5-nitropyridine and 2-amino-6-methyl pyridine (NMC)s pentaborates showed different thermal stabilities among each other, but degradation of the dehydration of the following organic both NMC pentaborate structure as part away and decomposition products of B_2O_3 occurs by having glassy structure. The trigonal (BO_3) and tetragonal (BO_4^-) moities were determined in ^{11}B NMR spectrums. According to P-XRD methods each of the compound structures are in crystalline form. The peaks of pentaborate anion $[B_5O_6(OH)_4]^-$ were seen in FT-IR spectra. Lastly, the hydrogen storage properties of these molecules were studied. The estimated molecular formulas of the complexes are as follows:

2-amino-5-nitropyridine pentaborate: $[C_5H_5N_3O_2][B_5O_6(OH)_4]3H_2O$
2-amino-6-methylpyridine pentaborate: $C_6H_8N_2][B_5O_6(OH)_4]2H_2O$

Key Words:
Boron; Non-metal Cation Borate Structure; Pentaborate; P-XRD; Thermal Investigation; ^{11}B-NMR.

INTRODUCTION

Boron is a chemical element with symbol B and atomic number 5. Because boron is produced entirely by cosmic ray spallation and not by stellar nucleosynthesis, it is a low-abundance element in both the Solar system and the Earth's crust [1]. In biology, borates have low toxicity in mammals (similar to table salt), but are more toxic to arthropods and are used as insecticides. Boric acid is mildly antimicrobial, and a natural boron-containing organic antibiotic is known [2]. The earliest routes to elemental boron involved reduction of boric oxide with metals such as magnesium or aluminum. However the product is almost always contaminated with metal borides. Pure boron can be prepared by reducing volatile boron halides with hydrogen at high temperatures. Ultrapure boron for use in the semiconductor industry is produced by the decomposition of diborane at high temperatures and then further purified with the zone melting or Czochralski processes [3]. Elemental boron is rare and poorly studied because the material is extremely difficult to prepare. Most studies on "boron" involve samples that contain small amounts of carbon. Chemically, boron behaves more similarly to silicon than to aluminum. Crystalline boron is chemically inert and resistant to attack by boiling hydrofluoric or hydrochloric acid. When finely divided, it is attacked slowly by hot concentrated hydrogen peroxide, hot concentrated nitric acid, hot sulfuric acid or hot mixture of sulfuric and chromic acids [4]. Boron is always found in nature combined with oxygen as anhydrous mixed metal oxides or as hydrated metal borates, with more than 200 borate minerals known and more than 100 were structurally characterized [5–7]. Borate materials have attracted a great deal of attention in the past decades because of their rich structural chemistry and potential applications in mineralogy and industry [8-10]. The large family of borate materials have provided an expansive area of research in the last decades owing to their rich structural chemistry and important applications as nonlinear optical (NLO) crystals, luminescent host materials, lithium battery electrodes and porous open-frameworks for catalysis and separation [11]. From the structural point of view, boron atoms may coordinate with oxygen atoms not only in three-fold coordination (triangular, BO_3), but also in four-fold coordination (tetrahedral, BO_4). The BO_3 and BO_4 groups may be further linked via common oxygen atoms to form polynuclear anions, including isolated rings (or cages), infinite chains, sheets and frameworks and salts containing polyanions such as $[B_4O_5(OH)_4]_2^{[-11]}$, $[B_5O_6(OH)_4]_1^{-[12]}$ and $[B_9O_{12}(OH)_6]_3^{-[13]}$ have been reported [12–17]. Some structures display 'isolated' borate or polyborate anions, but the vast majority display more condensed anions comprising infinite chains, sheets or networks. Generally, the boroxole (B_3O_3) ring in various guises is a reoccurring structural motif, with the Lewis acidity of the metal counter-ions influencing the observed structures: strongly Lewis acidic metals being commonly found in structures with a high proportion of four-coordinate boron sites [18,19]. The only minerals that do not contain metal counter-ions are ammonioborite, $[NH_4]_3[B_{15}O_{20}(OH)_8].4H_2O$ [20] and larderellite $[NH_4][B_5O_7(OH)_2].H_2O$ [21] and these polyborate minerals have anionic structures exclusively paired with the ammonium cation. Non-metal cations differ from metal cations in their potential for interactions with borate anions: metal cations are spherical and primarily accept electron density from oxygen donors whilst non-metal cations may be nonspherical and may have H-bond donor sites [22]. These properties may lead to previously unobserved borate structural moieties and further offers the opportunity to explore structure directing H-bond relationships. Indeed, the guanidinium and imidizolium poyborate systems both display the isolated nonaborate anion, $[B_9O_{12}(OH)_6]^{-3}$, and this anion is only observed with these non-metal cations [23]. More recently some template complexed metal cation/ pentaborate anion salts have been characterized [24]. In this study, we reported non-metal cation (NMC) pentaborate structures derived from the amino acids histidine and arginine and characterized by spectroscopic and thermal and methods.

EXPERIMENTAL

0,02 mol 2-amino-5-nitropyridine and 2-amino-6-methylpyridine (Sigma-Aldrich) were solved in a mixture of acetonitrile (50/50 mL). Then (5.5 mL) methyl iodide (Sigma-Aldrich) was added on both of them to occur cationic form for 2-amino-5-nitropyridine and 2-amino-6-methylpyridine ligands. The solution was heated using heating basket about two hours at 85°C under reflux unit. Then formed colour different crystals were collected with filtration. Then the crystals were solved in 100 mL distillation water and the ion-exchange resin was added on it (double amount of crystals). The purpose of this step is to change iodine ion in 2-amino-5-nitropyridine and 2-amino-6-methylpyridine with hydroxy ion in resin. The solution with ion exchanger resin was remained about 24 hours at room temperature. After the filtration of resin, 0.1 mol (6.2 g) boric acid (Sigma-Aldrich) was added on the ion-exchanged solution. The last solution was stirred about two hours on magnetic stirrer. Then the solution was evaporated until drying with rotatory evaporator and the precipitate samples was collected and dried at 50°C in a vacuum stove.

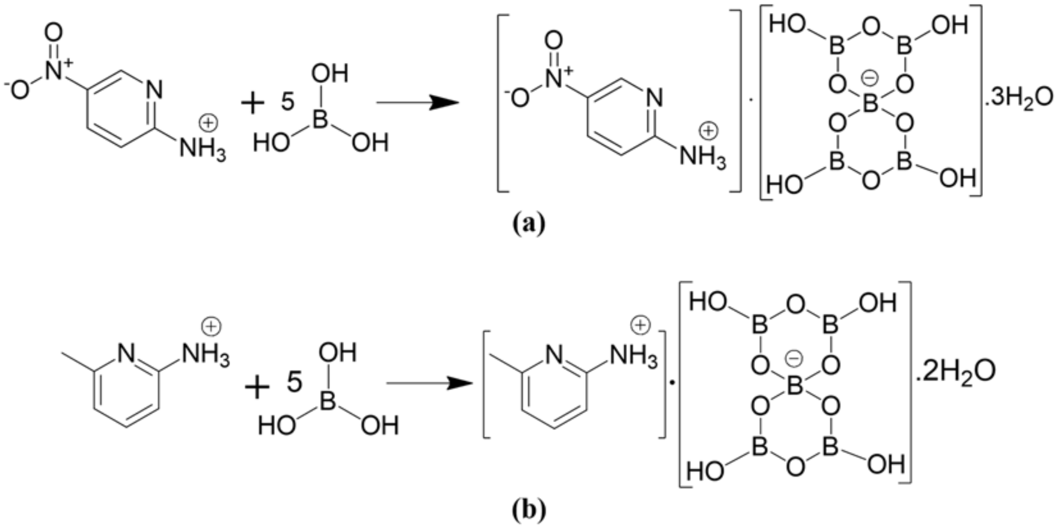

Figure 1. Synthesis scheme of 2-amino-5-nitropyridine pentaborate (a) and 2-amino-6-methylpyridine pentaborate (b) salts..

Table 1. Analytical results of 2-amino-5-nitropyridine and 2-Amino-6-methylpyridine derived pentaborates.

Molecular Formula	*M.W. (g/mol)*	*Yield (%)*	*Melting Point (°C)*	*C (%) Exp.Calc*	*H (%) Exp.Calc*	*N (%) Exp.-Calc.*
$C_5H_{16}B_5N_3O_{15}$	412.25	90	110	13.55-14.57	4.23-3.91	10.12-10.19
$C_6H_{16}B_5N_2O_{12}$	362.25	88	136	18.62-19.89	4.02-4.45	7.52-7.73

The synthesis reactions of 2-amino-5-nitropyridine and 2-amino-6-methylpyridine pentaborate were described below and obtained in a 88% and 90% overall yield respectively. Analytical data are shown in Table 1.

RESULTS AND DISCUSSION

The Figure 2 showes that FT-IR spectrum curves of 2-amino-5-nitropyridine pentaborate (red line) and 2-amino-6-methylpyridine pentaborate (black line) salts. The strong and broad bands at 3600-3000 cm^{-1} for each of the salt compounds are attributed to –OH stretching [25]. While, the peaks at the range of 3398 and 3391 cm^{-1} belong to N-H groups, at the 3197 and 3191 cm^{-1} refer to C-H groups of organic cations, respectively. The bands of C=C and bending N-H group appear at range of the 1468, 1399 cm^{-1} and 1457, 1407 cm^{-1}, consecutively [26]. The peaks at the 1230, 1200 cm^{-1} for 2-amino-5-nitropyridine pentaborate salt are concerned to B-O stretchings of triangular BO_3, while B-O stretchings of tetragonal BO_4^- are come out at the range of 1137, 1050 cm^{-1} [27]. The same group peaks of 2-amino-6-methylpyridine pentaborate salt are appeared at the range of 1238, 1207 cm^{-1} for triangular BO_3 and 1140, 1055 cm^{-1} for tetragonal BO_4^-. The most important peak for pentaborate structures is $B_5O_6(OH)_4^-$ anion group peak [28] that is obtained at the range of 530 cm^{-1} for 2-amino-5-nitropyridine pentaborate salt and 529 cm^{-1} for 2-amino-6-methylpyridine pentaborate salt.

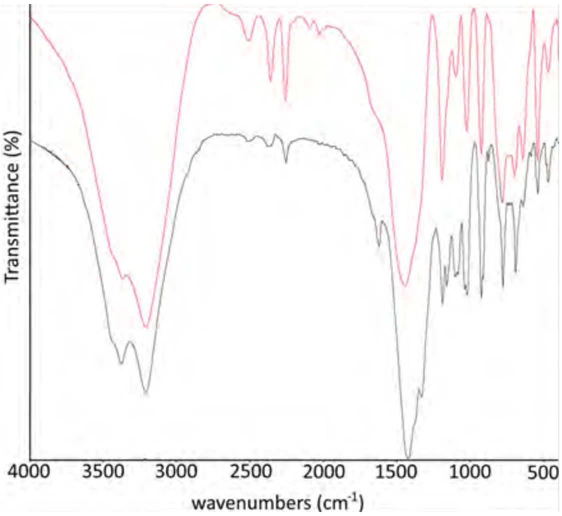

Figure 2. FT-IR spectrum curves of 2-amino-5-nitropyridine pentaborate (red line) and 2-amino-6-methylpyridine pentaborate (black line) salts.

^{11}B NMR spectra (400 MHz, D_2O) of 2-amino-5 nitropyridine (Figure 3a) and 2-amino-6-methylpyridine pentaborate (Figure 3b) derived pentaborates were given Figure 3. The 2-aminopyridine pentaborate spectrum has three peaks that are at 19.07 ppm attributed to trigonal free boric acid, at 13.10 ppm attributed to triborate structure and at 1.13 ppm tetrahedral center of pentaborate structure. The 2-amino-5nitropyridine pentaborate spectrum has three peaks that are at 19.39 ppm attributed to trigonal free boric acid, at 12.77 ppm attributed to triborate structure and at 1.16 ppm tetrahedral center of pentaborate structure. These results agree with previous literature [25,29-31].

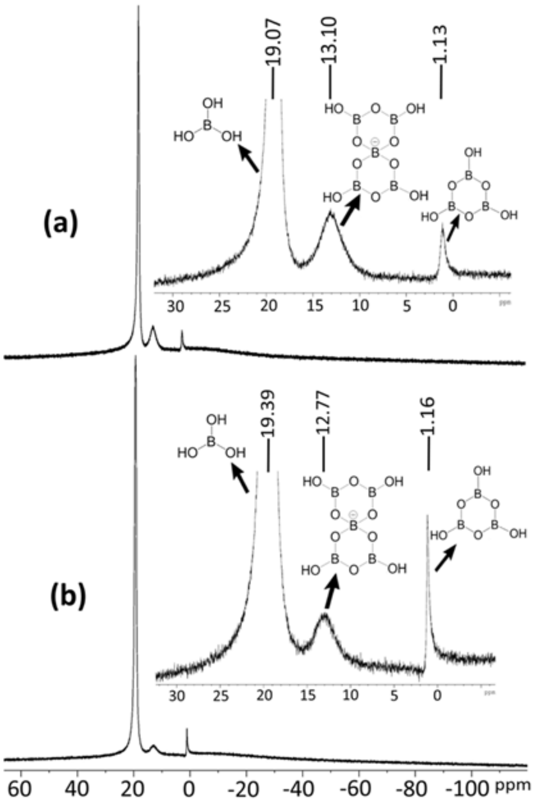

Figure 3. ^{11}B NMR curves of a) 2-amino-5 nitropyridine and b) 2-amino-6-methylpyridine pentaborate salts.

The ^{11}B NMR spectra of the 2-amino-5 nitropyridine and 2-amino-6-methylpyridine pentaborate salts are complex but explainable in terms of a complex series of equilibria existing in aqueous solution which link

Table 3. Thermal degradation steps and temperatures details.

Complex		Temp. Range/ (°C)	DTA$_{max.}$ (°C)	Removed Group	Weight Change/%		Total Loss / %		Decom. Prod.	Colour
					Found	Calc.	Found	Calc.		
$[C_5H_5N_3O_2][B_5O_6(OH)_4]3H_2O$ 412.25 g/mol	1	65-147	81	$3H_2O$	13.25	13.10				White
	2	149-241	197	$2H_2O$	8.73	9.22				
	3	243-567	275,471	$C_5H_6N_3O_2$	31.12	33.99	46.41	44.39	B_5O_8	Black
$[C_6H_8N_2][B_5O_6(OH)_4]2H_2O$ 362.25 g/mol	1	68-162	146	$4H_2O$	18.92	19.88				White
	2	164-493	177	$C_6H_9N_2$	29.61	30.13	51.47	50.53	B_5O_8	Black

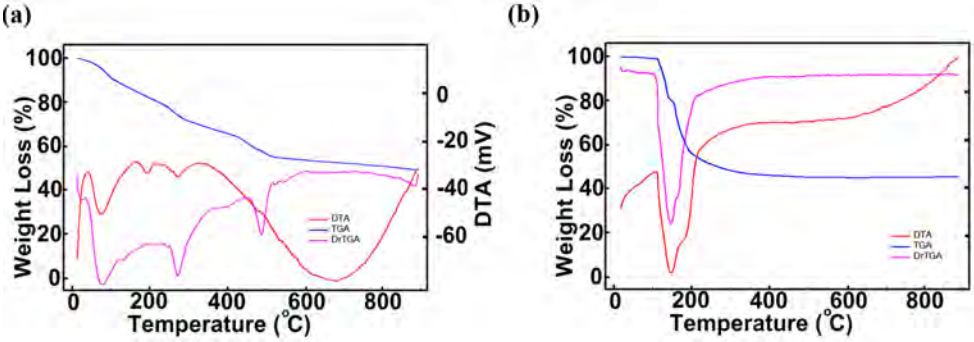

Figure 4. TGA/DTA/DTG curves of a) 2-amino-5 nitropyridine and b) 2-amino-6-methylpyridine pentaborate salts.

monomeric and oligomeric borate species [3].

Thermal analysis curves of 2-amino-5 nitropyridine (Figure 4a) and 2-amino-6-methylpyridine (Figure 4b) pentaborate salts are shown Figure 4. TGA data of NMCs pentaborates were recorded in the temperature range of 25-900°C in nitrogen atmosphere. Thermal decompositions take place in three stages. The first stage is attributed to dehydration each of them and then pentaborate hydroxy groups remove from the structure as aqua molecules. Thereafter, the organic portions are decomposed and remove as $CO/CO_2/NO/NO_2$. Finally a glassy B_5O_8 residue remains degradation products product of pentaborate salts. The thermal degradation steps and temperature range are detailed in Table 3.

The powder XRD patterns are given Figure 5. Red line curve for 2-amino-5-nitropyridine pentaborate and black line curve for 2-amino-6-methylpyridine pentaborate. According to P-XRD data products are mostly crystalline, but the structures have some of amorphous regions. They include main component boric acid and pentaborate salts. The compounds include amorphous residue in proportion as %9.4 and %8.9, respectively. Above, similar results are seen in ^{11}B NMR spectra of compounds.

According to single point BET analysis data the compounds surface area of 2-amino-5-nitropyridine pentaborate is 5.47 m^2/g and 2-amino-6-methylpyridine pentaborate is 3.15 m^2/g.

Lastly, hydrogen storage capacity of each compound was measured experimentally and the results were given Figure 6 as graphical data and summarized in Table 4. Eventually, the storage capacities of materials were 0.043 for 2-amino-5-nitropyridine pentaborate and 0.060 for 2-amino-6-methylpyridine pentaborate wt.%, while the values were 0.092 and 0.102 within the unit of g hydrogen/L adsorbent, respectively.

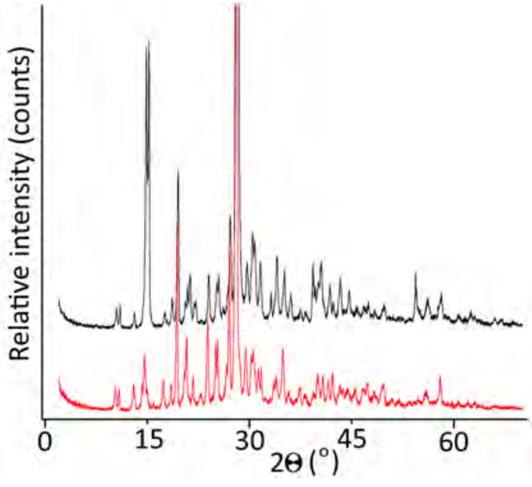

Figure 5. The powder XRD pattern of pentaborate salts. 2-amino-5 nitropyridine pentaborate (red line) and 2-amino-6-methylpyridine (black line).

Table 4. The hydrogen storage data of pentaborate salts.

Hydrogen Storage	*2-amino-5 nitropyridine pentaborate*	*2-amino-6-methylpyridine pentaborate*
Mass (%)	*0,043*	*0,06*
Volumetric (/g/ ml)	*0,092*	*0,102*

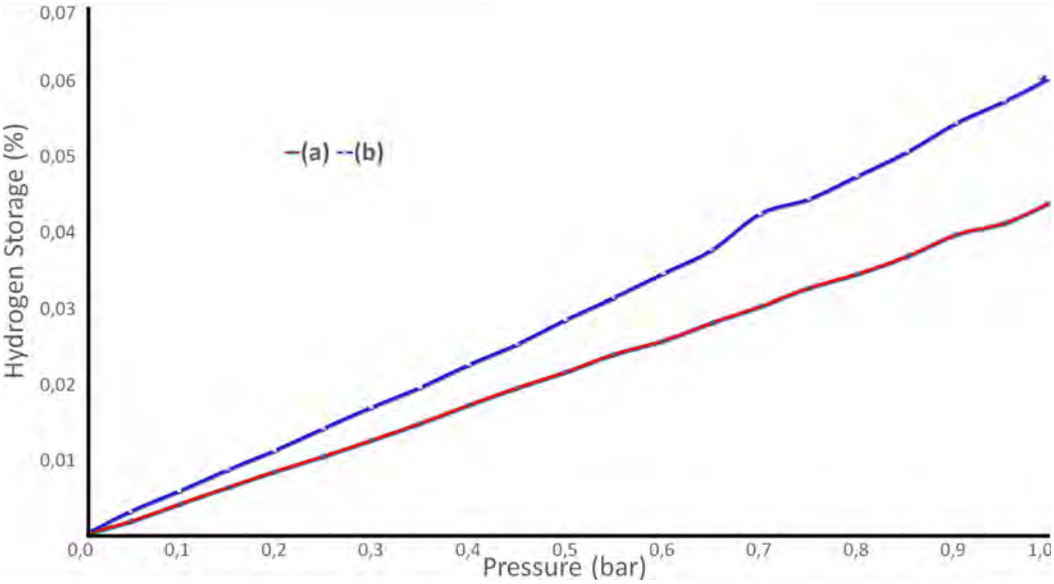

Figure 6. The hydrogen storage (mass %) graphic, (a) 2-amino-5 nitropyridine pentaborate and (b) 2-amino-6-methylpyridine pentaborate salts.

CONCLUSION

NMC pentaborate salts using amino pyridine derivatives, $[C_5H_5N_3O_2][B_5O_6(OH)_4]3H_2O$ and $[C_6H_8N_2][B_5O_6(OH)_4]2H_2O$, have been synthesized and characterized. The ^{11}B NMR spectra support to powder XRD pattern that the molecules include boric acid and pentaborate salt with organic cation. The final product, as a result of decomposition of pentaborate salts was obtained B_5O_8. Thermal stability of these two salts is as follows: 6-aminopicoline pentaborate > .2-amino-5-nitropyridine pentaborate. The surface area of 2-amino-5-nitropyridine pentaborate is 5.47 m^2/g and 6-aminopicoline pentaborate is 3.15 m^2/g according to single point BET analysis.

ACKNOWLEDGEMENT

This research was supported by the Science Research Department of Hitit University (Project no: FEF.19004.13.003).

REFERENCES

1. "Q & A: Where does the element Boron come from?". physics.illinois.edu. Retrieved 2011–12–04.
2. "The tartrolons, new boron–containing antibiotics from a myxobacterium, Sorangium cellulosum.". Retrieved 2013–01–24.
3. Berger LI. Semiconductor materials. CRC Press. pp. 37-43, 1996.
4. Laubengayer AW, Hurd DT, Newkirk AE, Hoard JL. Boron. I. preparation and properties of pure crystalline boron. Journal of the American Chemical Society 65(10) (1943) 1924-1931.
5. Heller G. A survey of structural types of borates and polyborates. Topic Current Chem. 131 (1986) 39-98.
6. Schubert MR, Brotherton J. in: RB. King (Ed.), Encyclopedia of Inorganic Chemistry, second ed. Wiley, New York, pp. 499-524, 2005.
7. Schubert M. Borates in industrial use. Struct. Bond. 105 (2003) 1-40.
8. Christ CL, Clark JR, A crystal–chemical classification of borate structures with emphasis on hydrated borates. Phys. Chem. Miner. 2 (1977) 59–87.
9. Burns PC. Borate clusters and fundamental building blocks containing four polyhedra; why few clusters are utilized as fundamental building blocks of structures. Can. Mineral. 33 (1995) 1167–1176.
10. (a) Wang GM, Sun YQ, Yang GY. Syntheses and crystal structures of two new pentaborates. J. Solid State Chem. 178 (2005) 729–735; (b) Wang GM, Sun YQ, Yang GY. Synthesis and characterization of a new layered lead borate, J. Solid State Chem. 179 (2006) 398–403.
11. Khan MdS, Prasad G, Kumar GS. Dielectric Properties of Ammonium Pentaborate Sinple Crystals. Crystal Research and Technology, 27(2) (1992) K28–K31.

12. Touboul M, Penin N, Nowogrocki G. Crystal Structure and Thermal Behavior of $Cs_2[B_4O_5(OH)_4]3H_2O$. J. Solid State Chem. 143 (1999) 260–265.
13. Schubert DM, Alam F, Visi MZ, Knobler CB, Structural characterization and chemistry of the industrially important zinc borate, $Zn[B_3O_4(OH)_3]$. Chem. Mater. 15 (2003) 866–871.
14. Yu ZT, Shi Z, Jiang YS, Yuan HM, Chen JS. A chiral lead borate containing infinite and finite chains built up from BO_4 and BO_3 units, Chem. Mater. 14 (2002) 1314–1318.
15. Penin N, Touboul M, Nowogrocki G. Crystal structure of a new form of sodium octoborate β–$Na_2B_8O_{13}$. J. Solid State Chem. 168 (2002) 316–321.
16. Huppertz H, von der Eltz B. Multianvil high– pressure synthesis of $Dy_4B_6O_{15}$: The first oxoborate with edge–sharing BO_4 tetrahedra. J. Am. Chem. Soc., 124 (2002) 9376–9377.
17. Zhang HX, Zheng ST, Yang GY. Pentaethylenehexamine manganese(II) pentaborate, Acta Cryst. C 60 (2004) m241–m243.
18. Schindler M, Hawthorne FC. A bond–valence approach to the structure, chemistry and paragenesis of hydroxy–hydrated oxysalt minerals. II. Crystal structure and chemical composition of borate minerals. Can. Mineral. 39 (2001) 1243–1256.
19. Brown ID. in: O'Keeffe M, Navrotsky A. (Eds.) Structure and bonding in crystals, vol. 2, Academic Press, New York, pp. 1- 30, 1981.
20. Merlino S, Sartori F. Ammonioborite: new borate polyion and its structure.. Science 171 (1971) 377-379.
21. Merlino S, Sartori F. The crystal structure of larderellite, $NH_4B_5O_7(OH)_2.H_2O$. Acta Crystallogr., Sect. B 25 (1969) 2264-2270.
22. Schubert DM, Smith RA, Visi MZ. Studies of crystalline nonmetal borates. Glass Technol. 44 (2003) 63-70.
23. Schubert DM, Visi MZ, Knobler CB, Guanidinium and Imidazolium Borates Containing the First Examples of an Isolated Nonaborate Oxoanion: $[B_9O_{12}(OH)_6]^{3-}$. Inorg. Chem. 39 (2000) 2250-2251.
24. Wang GM, Sun YQ, Yang GY. Syntheses and crystal structures of three new borates templated by transition–metal complexes in situ, J. Solid State Chemistry 179 (2006) 1545–1553.
25. Köse DA, Beckett MA, Çolak N. Synthesis, spectroscopic and thermal characterization of non–metal cation (NMC) pentaborates salts containing cations derived from histidine and arginine. Hacettepe J. Biol. & Chem., 40(3) (2012) 219-224.
26. Kamitsos EI. Infrared studies of borate glasses. Physics and Chemistry of Glasses, vol. 44(2), pp. 79-87, 2003.
27. Gautam C, Yadav AK, Singh AK. A review on infrared spectroscopy of borate glasses with effects of different additives. ISRN Ceramics, 2012, Article ID 428497, doi:10.5402/2012/428497.
28. Janda R, Heller G. IR– und raman spektren isotop markierter tetra– und pentaborate. Spectrochimica Acta 36A (1980) 997-1001.
29. Beckett MA, Bland CC, Coles SJ, Horton PN, Hursthouse MB. Supramolecular structures containing 'isolated' pentaborate anions and non–metal cations: Crystal structures of $[Me_3NCH_2CH_2OH][B_5O_6(OH)_4]$ and [4–MepyH, 4–Mepy]$[B_5O_6(OH)_4]$. J. Organomet. Chem. 692 (2007) 2832–2838.
30. Salentine CG. High–field ^{11}B NMR of alkali borates. Aqueous polyborate equilibria. Inorg. Chem. 22 (1983) 39203924.
31. Beckett MA, Horton PN, Hursthouse MB, Knox DA, Timmis JL. Structural (XRD) and thermal (DSC, TGA) and BET analysis of materials derived from non–metal cation pentaborate salts, Dalton Trans. 39 (2010) 3944–3951.

Hittite Journal of Science and Engineering, 2015, 2 (1) 97-102
ISSN NUMBER: 2149-2123
DOI: 10.17350/HJSE19030000015

Monitoring of Waste Gasification Products: Solid, Liquid and Syngas

Atakan Ongen and Semiha Arayici
Istanbul University, Department of Environmental Engineering, Istanbul, TURKEY

Article History:
Received: 2015/05/23
Accepted: 2015/06/16
Online: 2015/07/01

***Correspondence to**: Atakan Ongen,*
Istanbul University, Faculty of Engineering,
Department of Environmental Engineering,
Istanbul, Turkey
Tel: +90 (212) 473-7070(17724)
Fax: +90 (212) 473-7180
E-Mail: aongen@istanbul.edu.tr

ABSTRACT

In this study, biomass and waste gasification efficiencies were investigated in a lab-scale fixed bed reactor by the use of cyclone separator. Solid, liquid and gas products were monitored both during and after the completion of the process. Solid residue and liquid product obtained from waste gasification were studied through the use of Thermo-Gravimetric Analysis (TGA); and chemical properties were identified by elemental analysis and X-Ray Fluorescence (XRF) analyzer. Walnuts and pine cones were gasified as biomass. Syngas production being a function of temperature was monitored by analyzing H_2, CH_4, CO gases with a continuous gas analyzer. Mass reduction of 64%, 80% and 77% were achieved during the gasification of biological wastewater treatment sludge, walnut and pine cone, respectively. Syngas with almost 1500 kcal m-3 calorific value was produced. As for biomass syngas calorific value, it increased up to 2800 kcal m-3 for walnuts and 2500 kcal m-3 for pine cones.

Key Words:
Waste Management; Thermochemical Process; Gasification; Waste to Energy.

INTRODUCTION

Waste management hierarchy is one of the leading alternatives which are not desired to be disposed via storage. Some of its disadvantages can be counted as the need for wide area due to the high amount and volume of wastes and the high costs to minimize contamination risks. The management of waste sludge based on waste water treatment facilities focuses on reducing sludge weight and volume to reduce disposal costs, and on reducing potential health risks of disposal options. Thermochemical processes such as pyrolysis and gasification are among safe methods that are applied to this end. In this way, volume and weight of waste can be reduced and the amount of waste transferred to storage fields can be minimized and microbial stabilization of wastes can be achieved at high temperatures. Another important approach is to obtain products having an economic value through these processes. Within the scope of "waste to energy", energy recycling can be achieved from waste materials and valuable products that can be used in solid, liquid and/or gas form can be obtained. These processes called zero emission technologies lead to more environment-friendly waste management mechanisms [1-3]. There are many environmental benefits that can be derived from the use of waste reduction, waste reuse and recycling methods. The most significant environmental benefit caused by gasification will occur in air emissions. The overall reduction of total sulphur gases using gasification technology will also reduce odor [5]. Gasification allows a reduction of the amount of residues to be disposed in landfills and achieves co-gasification of different kind of wastes, including bottom ashes from conventional combustion units [6]. Gasification of wastes and/or biomasses may improve techno-economic situation of gasification process.

Gasification has been widely studied and numerous literature can be found about biomass gasification [7-10]. Gasification is a process that converts a combustible fuel into a partially oxidized gas called "syngas" with economically valuable heating value. Syngas is basically a mixture of CO, H_2, CO_2, CH_4 and H_2O. Fuel as a feedstock is converted into useful energy carriers and can be any hydrocarbon regarding to parameters such as feedstock composition, moisture, ash content, particle size, density, reactivity, etc. [7, 11]. Ramey et.al.

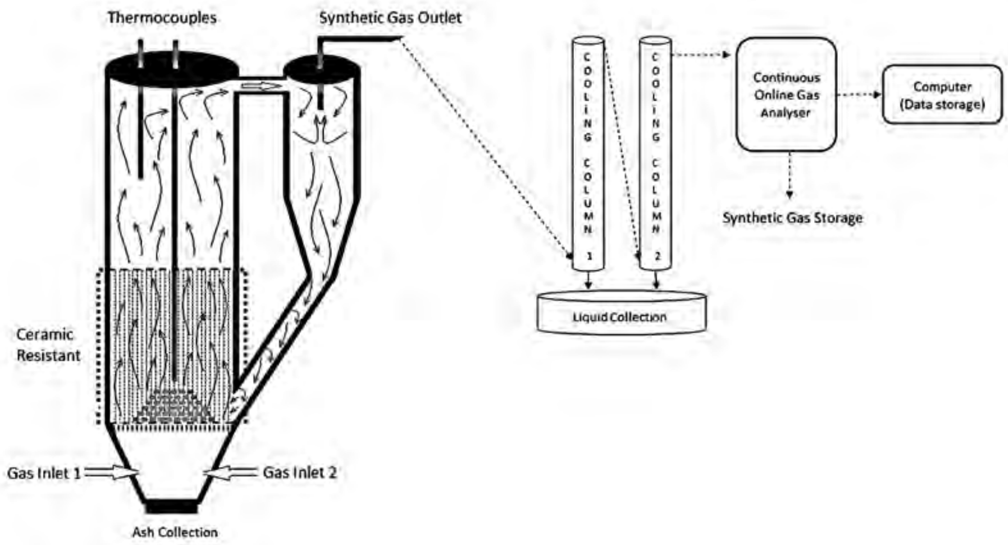

Figure 1. Schematic diagram of reactor.

(2015) reported that gasification is a promising technology to treat wastewater solids, and potentially enabling energy recovery. The authors also claimed that gasification is suitable for wastewater solids for several reasons. Volatile matter is converted to syngas, solid and liquid residuals are stabilized and running at autothermal conditions lower than 900 °C results reduced complexity of reactor operation. Mainly two types of reactors were used for gasification of municipal solid waste (MSW) or biomass [12]. Fluidized bed requires more investment while fixed bed requires less investment and it is more suitable for smaller capacity MSW treatment. Fixed bed reactors for gasification process are commonly used for real systems which have a relatively smaller MSW yield [13].

In the study, monitoring of gasification products and identification of syngas composition were studied. Two different biomass and a real industrial wastewater treatment sludge were used as feedstock. Waste minimization efficiency regarding to mass and volume loss after thermal treatment was reported. Syngas calorific value for each feedstock was calculated according to the CO, H_2 and CH_4 content of syngas produced.

Table 1. Chemical properties of biomass and waste.

Properties, wt.%	*Walnuts*	*Pine cones*	*Bio. Chem.*
C	*50,85*	*44,54*	*24,3*
H	*6,62*	*5,48*	*5,18*
N	*2,05*	*0,71*	*4,57*
S	-	-	-
O	*40,48*	*49,27*	-
Ash	*2,8*		*35*
Moisture	*4,5*	*3,8*	*11*
Volatile Matter	*60,1*	*64,5*	*65*
HLV, MJ kg^{-1}	*20,8*	*18,85*	*6,70-7,12*

EXPERIMENTAL

Sample characterization

Biologically treated wastewater treatment sludge derived from a leather industry and two biomasses (walnuts and pine cones) were used as fuels during experiments. Product monitoring was investigated and conversion of physical forms was recorded. Table 1 shows the chemical properties of biomass and treatment sludge.

As can be expected, the carbon content of organic substances was found higher than the one of sludge collected from biologic waste water treatment facility. In all samples, carbon is remarkable as the dominant element. Comparing calorific values a similar result was observed. Oxygen within biomasses was calculated by subtracting it from the total mass. Change in the chemical properties of fuels directly affected the efficiency of gasification process.

Experimental approach

Thermochemical experiments were carried out in a fixed bed steel reactor by the use of a cyclone separator at 40 cm height and 7 cm diameter. The reactor was equipped with two gas inlet lines allowing gasification gases (dried air and/or pure oxygen) to enter and one exhaust line allowing generated syngas to pass through the continuous gas analyzer.

Dried air was used as partial oxidizer for gasification and flow rate varied was adjusted by a HOSCO-brand flow meter to 0.05 Lmin^{-1}. In the experiments, 20 g of

Table 2. Higher heating values of some common fuels.

HHV	*Density*	*MJ m^{-3}*	*kcal m^{-3}*
H_2	*0.0899*	*12.77*	*3050*
CO	*1.25*	*12.64*	*3020*
CH_4	*0.717*	*39.82*	*9520*

waste sludge and 50g of biomass were used. Gasification experiments were carried out at 750°C and gas composition variance depending on process temperature was recorded. The condensable part of the syngas was collected by cooling columns with water jacket. Then, syngas was directed to the continuous gas analyzer. CO, CO_2, H_2, CH_4 and O_2 content of syngas was monitored. Process temperature was followed up with two thermocouples extended into middle and upper internal zone of reactor. During gasification studies, composition of syngas produced with continuous gas analyzer was analyzed and recorded every minute.

Calculations

Syngas composition was determined by ABB-brand, The Advance Optima process gas analyzers equipped with thermo-magnetic and infrared photometers. Calorific value of syngas generated during gasification experiments was calculated. For calculations, values presented in Table 2 were used [14].

RESULTS AND DISCUSSION

TGA Analysis

Thermogravimetric Analysis results conducted in order to detect thermal behaviors of samples are presented in Figure 2.

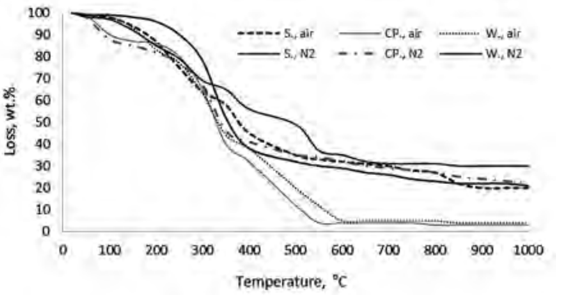

Figure 2. Thermogravimetric comparison of feedstock.

Based on the TG curves as a function of temperature, the mass loss range cannot be divided into zones since every single slope indicates independent behaviors against rising temperature. It can be said that all samples showed similar behavior in TG analysis conducted in N_2 environment. A slight mass loss, around 5-20%, was observed due to the removal of water within the materials between the ranges of 150-200 °C. With temperature rising, a high mass loss was observed (more than 50%) up to 350-400 °C. This zone was detected as where organic substance was pyrolytically decomposed. In this zone, there was the decomposition of hemicellulose, cellulose, and lignin-like contents especially within biomasses [4-6]. In the zone up to 1000 °C, on the other hand, mass loss continued degressively and mass loss was fixed at 80% for walnut and pine cone. It was fixed at 65% for sludge sample. At the end of the TG analysis conducted with air, there was an increase in mass losses due to the oxidation of organic content with oxygen. High mass loss was detected within similar 200-600 °C range for biomass samples as expected. At the end of the test, similar behavior was observed for both biomasses with a loss of 95%. On the other hand, sludge sample had approximately 75% mass loss based on the low organic substance content.

Thermochemical Processes

The gasification test was conducted with 0.05 L min^{-1} dry air volume at 750 °C. Data related to the mass and volume changes obtained from the tests are presented in Table 3.

Analyzing the sludge sample in terms of waste management and minimization, 64% mass and 62% volume decrease was recorded at the end of the process. Especially considering the problems derived from the coverage areas of wastes to be disposed from the storage areas, 62% volume decrease can be considered as a satisfactory minimization for wastes having organic and inorganic contents. In addition, the economic value of products in both liquid and gas form is considered as another advantage of the process. On the

Table 3. Conversion ratios - mass and volume.

Loss, mass	*Inlet, g*	*LP., g*	*SR., g*	*Loss, g*	*Loss, wt.%*	*Syngas, g.*
Bio. Sludge	*20*	*2,2*	*7,2*	*12,8*	*64*	*10,6*
Walnut	*50*	*14,8*	*10,2*	*39,8*	*79,6*	*25*
Pine cone	*50*	*13,5*	*11,3*	*38,7*	*77,4*	*25,2*
Loss, volume	*Inlet, ml*	*LP., ml*	*SR:, ml*	*Loss, ml*	*Loss, vol.%*	*Syngas, m^3 kg^{-1} fuel*
Bio. Sludge	*40*	*-*	*15,2*	*24,8*	*62*	*0,45*
Walnut	*70*	*-*	*11,7*	*58,3*	*83*	*1,85*
Pine cone	*72*	*-*	*13,5*	*58,5*	*81*	*1,94*

BS.: Biologically treated sludge WS.: Walnut shell PC.: Pine cone LP.: Liquid product SR.: Solid residue other hand, solid waste is considered as an addition agent that can be used in mixtures such as adsorbent or concrete, asphalt etc. based on its content. In this case, a process in line with the zero-waste approach can be conducted as each form that might be obtained from the waste sludge being used as fuel can be useful. In the literature, it is reported that 2.5 m^3 syngas can be obtained from 1 kg wood[15]. The syngas volumes; 1.94 and 1.85 m^3 kg^{-1} obtained from pine cone and walnut shell, respectively, in a fixed bed reactor show that the process was conducted satisfactorily.

Table 4. Composition of syngas

vol.%	Walnut	Pine Cone	B. Sludge
H_2	11-13	10-12	7-9
CO	28-31	21-23	17-19
CH_4	13-16	14-16	6-8
CO_2	15-20	15-20	10-14
O_2	1-2	1-3	1-3

Table 5. Average calorific values of syngas

HHV.	Walnut	Pine Cone	B. Sludge
kcal m^{-3}	2420-2855	2270-2585	1300-1610
MJ m^{-3}	10,5-12,1	10,1-10,8	5,1-6,7

Table 6. XRF results of raw and thermal treated samples.

wt.%	Raw sample	Treated sample
Na_2O	1,484	8,005
Al_2O_3	1,859	11,333
SiO_2	1,113	5,478
SO_3	2,167	1,854
CaO	5,078	17,455
Cr_2O_3	4,654	13,91
NiO	ND.	ND.
Fe_2O_3	0,282	1,395
ZnO	0,024	0,080
MgO	0,504	1,212
CuO	ND.	ND.
MnO	ND.	ND.
As_2O_3	ND.	ND.
PbO	ND.	ND.

Table 7. Results of Elemental Analysis.

	Elemental Analysis, wt.%			
	C	H	N	S
Biologic (Raw)	24,30	5,18	4,57	-
Biologic (Treated)	13,36	1,09	2,99	-
Walnuts (Raw)	50,85	6,62	2,05	-
Walnuts (Treated)	28,50	1,25	0,75	-
Pine cones (Raw)	44,54	5,48	0,71	-
Pine cones (Treated)	26,80	1,26	0,22	-

Syngas composition and calorific value

Maximum gas percentages obtained during tests are presented in Table 4. Here, values represent the highest value ranges detected based on the temperature. The syngas compositions produced from each fuel type are presented in volume type as %.

Analyzing gas compositions, it can be observed that CO gas is dominant. At the same time, CH4 gas was detected over 10% in tests conducted especially with biomasses. It was observed that the produced synthesis gas was the complete synthesis of H_2, CO and CH_4 gases. It can be said that CO_2 reduction was achieved at high temperatures based on high CO values (R.1). Char is gasified producing mainly methane according to the exothermic hydro-gasification reaction (R.2) [3]:

$$C + CO_2 \dashrightarrow 2CO \quad \Delta H°r = +172\ kJ/mol \quad (R.1)$$

$$C + 2H_2 \dashrightarrow CH_4 \quad \Delta H°r = -74.6\ kJ/mol \quad (R.2)$$

Syngas calorific values which were obtained at the end of the calculations made on the basis of values as can be seen in Table 4 are presented in Table 5.

Medium calorific syngas was achieved from biomasses according to the gas compositions given in Table 4. Calorific value of syngas from sludge sample was lower and it can be classified as “low calorific syngas”.

XRF and elemental analysis results of biologic treatment sludge

Both initial and post-process XRF analysis was conducted on sludge sample in order to observe thermal behavior of complex composition including organic and inorganic substances. The results are presented in Table6.

ND.: not detected

At the end of the analysis, some changes were detected in chemical contents of samples. An increase was detected especially in amounts of Na, Al, Si, Ca and Cr compounds detected within samples. This case can be explained by the condensation in non-volatile parts due to the loss of organic contents in samples. Keeping metal compounds within sludge at the end of heat treatment will make the remaining sludge to have environmental risk. In this case, the use of solid waste in alternative areas will be restricted and even more, it will be a must to manage it via waste management mechanisms. Furthermore, it is believed that keeping metallic forms within sludge can make it easy to control these types that can lead to air pollution. However, more tailed studies should be conducted to detect the relationship with air pollution.

Pre-process and post-process elemental analysis was conducted in order to observe elemental changes of sample and the obtained findings are presented in Table 7.

It was observed that carbon content of samples decreased but did not completely ended up at the end of the gasification tests conducted at 750 °C. This case can be affiliated with the limited performance of fixed bed reactor. Due to the lack of homogenous contact between the heat and sample, carbon which cannot take part in reactions and thus it is collected as solid residual at the end of the test. In this case, it is assumed that different reactor types such as fluid bed etc. should be tried for efficiency. The increase of gasification will lead to increase in the volume of produced syngas and thus amount of gas which is rich in calorific value will increase as well.

CONCLUSIONS

In this study, products in solid, liquid and gas forms obtained at the end of the gasification of treatment sludge which was collected from biologic treatment unit of two different biomass facilities and an industrial waste water treatment facility were monitored and their mass transformations were determined. In addition, composition of the produced synthesis gas composition was determined and calorific value calculations were made. The results obtained based on the data are as follows:

- Gasification is a very effective system to reduce the volume and mass of solid wastes just as in combustion. The advantage of this process compared to combustion is less emission. At the end of the gasification tests, it was found that waste sludge volumetrically decreased at 60-62% and biomasses decreased at 83-85%.
- Metallic forms in sludge intensified following the process and stayed within the sludge. This case puts the sludge into a more risky classification within the terms of waste management. Analysis on accessibility of metals to receiving environments from the sludge by means of toxicity characteristic leaching procedure (TCLP) will be one of the fundamental topics for further studies.
- Mass reduction was achieved as follows; 64% for Bio. Sludge, 79.6% for walnut and 77.4 for pine cone. TGA analysis reported more reduction that it was observed after thermal processes. The reason for that is believed to be the effect of reactor type and size. Related to the insufficient heat transfer through the feedstock material, thermal degradation was not as sufficient as it was in TGA.
- CO was the dominant compound of the produced syngas for each sample. It was found 28-31% for walnut; 21-23% for pine cone and 17-19% for sludge sample.
- 11-13%, 10-12% and 7-9% hydrogen was detected at the end of the gasification of walnut, pine cone and sludge, respectively.
- Methane is one of the syngas components. 13-16%, 14-16% and 6-8% methane production could be achieved for walnut sample, pine cone and sludge sample, respectively.

- Syngas having calorific value between the range of 2420-2855 kcal m^{-3} with walnuts; 2270-2585 kcal m^{-3} with pine cone and 1300-1610 kcal m^{-3} with biologic treatment sludge was produced.
- Some restrictions derived from the reactor type were observed during the use of carbon content of the fuel. It was detected that approximately half of the carbon content of fuels are left within the post-process solid residual.

REFERENCES

1. Romano MC, Spallina V, Campanari S. Integrating IT–SOFC and gasification combined cycle with methanation reactor and hydrogen firing for near zero–emission power generation from coal. Energy Procedia 4 (2011) 1168-1175.
2. Yamauchia Y, Akiyamaa K. Innovative Zero–emission Coal Gasification Power Generation Project. Energy Procedia 37 (2013) 6579 - 6586.
3. Romano M, Lozza G. Zecomix: a zero–emissions coal power plant, based on hydro–gasification, CO_2 capture by calcium looping and semi–closed high temperature steam cycle. Energy Procedia 1 (2009) 1473-1480.
4. Rollinson AN, Karmakar MK. On the reactivity of various biomass species with CO_2 using a standardised methodology for fixed– bed gasification. Chemical Engineering Science, 128 (2015) 82-91.
5. Bajpai P. Black Liquor Gasification. 1st Edition, ISBN: 978–0–08–100009–0, pages 87–92, Elsevier, 2014.
6. Arena U, Ardolino F, Di Gregorio F. A life cycle assessment of environmental performances of two combustion– and gasification–based waste–to–energy technologies. Waste Management, Available online 18, April 2015, http://dx.doi.org/10.1016/j.wasman.2015.03.041.
7. Consonni S, Vigano F. Waste gasification vs. conventional Waste–To–Energy: A comparative evaluation of two commercial technologies. Waste Management 32 (2012) 653-666.
8. Osowski, S, Neumann, J, Fahlenkamp, H. Gasification of biogenic solid fuels. Chemical Engineering and Technology 28 (2005) 596-604.

9. Knoef, H. Handbook on Biomass Gasification. In: Knoef, H. (Ed.), Biomass Technology Group (BTG) BV, Enschede, The Netherlands, pp. 1-378 (ISBN 90–810068–1–9) January 2005.
10. Midilli A, Dogru M, Akay G, Howarth CR. Hydrogen production from sewage sludge via a fixed bed gasifier product gas. Int J Hydrogen Energy, 27 (2002) (10):1035-41.
11. Perez JF, Melgar A, Benjumea PN. Effect of operating and design parameters on the gasification/combustion process of waste biomass in fixed bed downdraft reactors: An experimental study. Fuel 96 (2012) 487-496.
12. Bridgwater T. Review biomass for energy. J Sci Food Agric (2006); 86:1755-68.
13. Chen C, Jin YQ, Yan JH, Chi Y. Simulation of municipal solid waste gasification in two different types of fixed bed reactors, Fuel 103 (2013) 58-63.
14. Waldheim L, Nilsson T. Heating value of gases from biomass gasification. Report prepared for: IEA Bioenergy Agreement, Task 20 – Thermal Gasification of Biomass, Report no: TPS–01/16, TPS Termiska Processer AB, 2001.
15. Rajvanshi AK., 1986., Alternative Energy in Agriculture, Editor: Goswami, D.Y., Chapter 4, Vol. II, CRC Press, pgs. 83–102.

Hittite Journal of Science and Engineering, 2015, 2 (1) 103-114
ISSN NUMBER: 2149-2123
DOI: 10.17350/HJSE19030000016

Improving Fundamental Values and Environmental Awareness in Sustainable Engineering Education through Laboratory and Design Experiments

Nihan Kaya[1] **and Secil Satir**[2]
[1] Hitit University, Department of Chemical Engineering, Corum, TURKEY
[2] Hitit University, Department of Industrial Engineering, Corum, TURKEY

ABSTRACT

It is of the essence of this paper to attach importance to enabling prospective engineers to learn about simple and plain techniques and technologies of the past, while learning about the most up-to-date ones. The ancient and primitive handicrafts have gained importance as the requisites of sustainability and this has made old techniques and technologies popular again in the last 10 to 15 years, providing a significant area of research for international sustainability researchers. The historical awareness in this paper entails presentation of several examples from as far back as the primitive methods of the most ancient times. Perhaps, these methods are not directly used, but the paper aims to reach a conclusion with experiments that support sustainability by using similar simple methods to obtain simple prototypes that work with manpower. In this context, the paper conducts a basic research about the main objectives of sustainable engineering education. In addition to a comprehensive literature review, it considers environmental protection which is the main theme of sustainability particularly by presenting some results of laboratory experiments assigned to senior students for production of new material from waste materials. The paper illustrates a case analysis, original with its practical research methodology, and deals with the concept of sustainability with a decided awareness for history, environment, and design.

Key Words:
Sustainable Engineering Education; Historical and Environmental Awareness; Laboratory and Design Practices.

Article History:
Received: 2015/01/08
Accepted: 2015/06/17
Online: 2015/07/01

***Correspondence to**: Secil Satir,*
Hitit University, Faculty of Engineering,
Department of Industrial Engineering,
Corum, Turkey
Tel: +90 (364) 227-4533 (1268)
Fax: +90 (364) 227-4535
E-Mail: secilsatir@hitit.edu.tr

INTRODUCTION

The consequences of the Industrial Revolution experienced in the spheres of science and technology have tipped the scales of the ecological balance. Resulting ecological catastrophes included rapid loss of soil structure, extinction of species, desertification, acid rains, radioactive pollution, etc. Countries allocated part of their budgets to cope with and solve these emerging environmental problems and oriented their educational and political policies towards solving these issues. [1,2]. Therefore, it is of utmost significance to provide ecological training and also to train environment-conscious individuals in both solving environmental problems and in the protection of the environment. At this point, universities have a big share of responsibility. Although the young generation is not the instigator of the environmental problems, they are the people who will be affected from these issues and so they should be provided with more information, consciousness and sensitivity towards these problems than any other section of the community [1]. In countries like Turkey, where young people dominate the population, implementing environment protection measures could be possible only with a young population that has a high level of environmental awareness [3]. Apart from being an individual and social requirement, environmental education is also a right and should be evaluated under environmental rights. For this reason, it is an imperative to provide a training in which individuals are reminded of their rights and responsibilities in order to effect changes in their behaviors and to create a healthy, balanced and secure environment [4].

Being a lifelong education process, environmental training should be considered as part of training of any type and at any level. It was shown that students' levels of awareness for and sensitivity about environmental issues are irrespective of the grades they are in and that although they have a preconception of environmental issues and protection of resources, their daily practices and behaviors mismatch their level of knowledge. Accordingly, it was stressed that the efficiency of educational training given in undergraduate programs at universities in orienting attitude and behaviors should be questioned. It was further stressed that national strategies and policies are required for environmental training in institutions of higher education [1-5].

On the other hand, educational institutions that train engineers for corporations should teach about environmental issues and include communicative information from different engineering fields in their program as well as prepare their students for environment-friendly and sustainable production practices of the companies. In this context, Petersen's paper titled "The Potential Role of Design in a Sustainable Engineering Profile" investigates the profiles of engineers to be trained for the future and defends that sustainable design should be instilled with an interdisciplinary approach so that contemporary creative engineers could be trained [6].

A similar scholarly voice is heard in the article by Ochsendorf, titled "Sustainable Engineering: The Future of Structural Design": Here what needs to be taught is the global environmental influences and the importance of steel as a material; on the other hand, what could be contemporary solutions and sustainable structural designs; furthermore, what challenges await us in the future; and especially in engineering training the following should be taught: development of critical thinking, questioning hypotheses, seeking multiple possible solutions, solving open-ended problems [7].

The paper by Desha et al., titled "The Importance of Sustainability in Engineering Education: A Toolkit of Information and Teaching Material" dwells on the perils of climatic changes in recent years and considers the roles of engineers in sustainable development [8]. The paper questions engineering training and suggests renovations in the programs. Among many suggestions for new classes and courses are "Emerging Technological Innovations", "The Concept of Biomimicry - An Historical Context", and "Green Chemistry and Engineering – Benign by Design", which identify with the industrial design in the scope of this paper. These three suggested classes is a proof of our accurate synthesis of three fields for a multidisciplinary training of engineering, namely design-industrial product design- any engineering field –for example, chemical engineering- and history.

Another model study that underpin our paper is by Murphy et. al., titled "Sustainability in Engineering Education and Research at U.S. Universities" [9]. This article considers in detail engineering training at U.S. universities, and inspects the connection of classes/courses with the industry. They also define green engineering principles and fields; initially they display the current situation and then they determine what is lacking. All the authors are members to the sustainability center and suggest that green engineering principles should be applied at U.S. universities.

The aim of the paper

In the light of the facts above, and especially in the context of suggestions by Desha et. al. [8], research carried out by synthesizing multidisciplinary knowledge bring about exceptionally valuable information. Besides, information from many disciplines trigger opposite views for research, resulting in new ideas. Therefore, the aim of this paper is to synthesize information from three different and seemingly distinct fields, which draw nearer to each other thanks to the concept of sustainability, and provide a model for green engineering research as indicated by Murphy et. al. [9].

Main objectives of sustainable engineering education

One, perhaps the most important, objective of engineering training and education is to contribute to the development of social structure. In this context, Hilda Taba's "Social Studies Education" project and the experimental education project she conducted in San Francisco State University in early 1960s are of vital importance. The project ended two years later as she passed away in 1967; so the final report of the project was dedicated to her. The experimental project, "Social Studies Education", consisted of three significant sections and greatly influenced following training and education research and practice [10]:

"—Key Terms

> Project materials should include such key terms as cultural change, interdependency, power, collaboration, conflict, and causality. These selected key terms should be managed and synthesized according to their own specific facts.

—Organization Ideas:

> The five criteria or special factors for the organization and combination of the information and ideas learned after a unit is covered are below:

1. Meaning: Does it show important relationships

according to different viewpoints? How will the main issues be studied?
2. Explanatory power: Is the knowledge helpful in explaining and understanding the problems people face today? What are the socially and culturally important issues?
3. Convenience: Is the knowledge suitable for the students' needs, interests, and development?
4. Endurance: Is the knowledge of any permanent significance?
5. Balance: Does the knowledge promote our understanding of events, individuals, actions or phenomena?

In education, learning spirals are quite old and trustable schematic illustrations. In Hilda Taba's long-lasting experimental work and in her posthumously published work, conceptualized spirals were introduced in educational practices. Received Hilda Taba's attention and interest and presented by Juran in the context of quality development, the spirals were further developed by Bostingls' thought, adapted and integrated into education in the concept of "Total Quality in Education".

The continuous improvement in total quality in education is revised in each turn of the spiral by perceiving the attained state, conceptualizing it, thinking, acting, and reacting against negativities and providing sustainability by grading improvement. This is, in a sense, reproducing previously existing values with a contemporary understanding.

"Quality Model in Education" proposed by Bonstingl [11] was designated as "Continuous Learning and Development Model" instead of the old model taught and employed before.

Quality model in education offers the following features: unlimited and continuous improvement; diagnosis and evaluation through orientation; a spiral ascension through self-control; progress-focused as well as goal-focused; a lifelong journey with a desire for learning; an integrated system that is complete with learner-teacher-manager and other complementary people as well as physical environment; a lively and meaningful learning process in which learners are proud of the results and wish for its continuity; a teaching team that remove obstacles; continuous improvement suitable for the vision and mission of the university; an interdisciplinary focus on research and learning; an instruction and management focused on people and institutions and their locations rather than the restrictions of curriculum-resources-method-time; international equivalence of the same instruction and management; transformation of instruction/learning processes – testing by process portfolios; a training that enables students to ask better questions; instruction that could be transferred to or taken from real life situations. Students who got conscious training will cause positive and fruitful processes and results. All these characteristics and features offered by quality in education could also be considered in sustainable engineering education in the scope of "occupational and ethical responsibilities related to engineering practices".

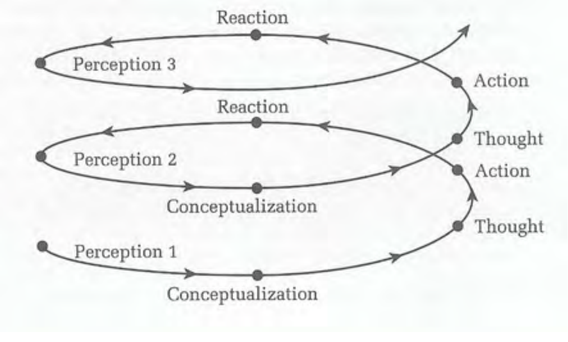

Figure 1. Bonstingl Spiral, [11].

"Rochester Institute of Technology" (RIT) could be counted among exemplary educational institutes in sustainable engineering education. Its educational programs have been designed in order to fulfill the following educational objectives and main goals:

- "Heightened awareness of issues in areas of sustainability (e.g., global warming, ozone layer depletion, deforestation, pollution, ethical issues, fair trade, gender equity, etc.).
- Clear understanding of the role and impacts of various aspects of engineering (design, technology, etc.) and engineering decisions on environmental, societal, and economic problems. Particular emphasis is placed on the potential trade-offs between environmental, social, and economic objectives.
- Strong ability to apply engineering and decision-making tools and methodologies to sustainability-related problems.
- Demonstrated capacity to distinguish professional and ethical responsibilities associated with the practice of engineering" [12].

Many more institutions could be provided as examples in terms of sustainable engineering education. All these institutions identify themselves with contemporary engineering education; it is certain that in terms of sustainability, they provide their students with environmental awareness. However, the examples that will be given in the scope of this paper will center on both the laboratory studies in engineering education and example projects that could be realized in Turkish design education as well as the differences they could bring about in sustainable engineering education.

Environmental awareness and environment-friendly production

When we look at the history of economy, we see that environmental issues have not emerged independently of people's life cycle but came into existence together with production and consumption and "...followed a course which was linked to the increase in production and consumption" [13].

After the inception of industrial revolution in England around 150-200 years ago, the mass production systems were copied by other countries. These developments encouraged people to consume more and the incalculably rapid growth of economy resulted in incredible pollution with chimney gases from coal operated factories, toxic waste from chemical industries, etc Although a delayed action, the number of enterprises that act sensitively in terms of environmental protection is growing bigger. Manufacturing enterprises should first learn about "environment-friendly production", which is an important standpoint of sustainable production.

"Environment-friendly production" is a concept that is synonymous with sustainable production. It could be defined as a manufacturing style which uses the least natural materials (e.g. forest products), which uses the least energy, which does not leave waste and which makes the product with the highest output. The main objective of environment-friendly production is stated as the optimizing resource materials without upsetting the balance of nature and minimizing the hazardous effects of waste on environment. To attain this main objective it is essential that the amount of waste and their flow should be defined, evaluated, and managed at the stages of product and process design, production planning, and production control.

Drawing on the work of Yücel and Ekmekçiler [14] explain that environment-friendly technologies fall under four main categories:

- "Technologies oriented towards eradicating the hazardous effects resulting from a procedure: These are the technologies that eliminate waste and other hazards resulting from production without making any changes in production process.
- Technologies that minimize raw materials, auxiliary materials, natural resource input and waste output by making changes in process. These are oriented towards changing the production process and production type. They are processes and final products that consume less energy, less water and less chemicals but work more efficiently and produce less hazardous waste.
- Recycling technologies: Technologies that enable reusing waste material by modifying them into new material, prevent littering, and minimize the consumption of natural resources.
- Old and traditional environment-friendly technologies: technologies that are inherently environment-friendly, in other words technologies that do not harm environment."

The technologies that seek solutions by changing processes are called "clean product-clean production" technologies. The main principle of clean production is to take preventive measures, not corrective ones. Accordingly, measures should be taken in order to use less raw materials and energy and minimize waste. For this end, ameliorating technological processes and developing new processes fall within the scope of sustainable production. The third item in the study by Yücel ve Ekmekçiler, recycling and reusing technologies have been in place for a long time. Waste paper, glass, metal, wood, and even plastics are recycled by breaking, melting, and are reproduced with various technologies as new materials of different types and purpose, and raw materials are used again [14].

Although few in number, old traditional environment-friendly technologies continue to exist especially in underdeveloped and developing countries. Small-sized enterprises that make production by handcrafts using semi-products still continue their handcrafting production today and earn their living with these production methods. Most of the medium-sized enterprises continue their half-machine-half-manpower production and operate in ateliers.

The literature shows that transition stage to sustainable production could be inspected in three groups: passive, active, and pro-active. Applied to product and services, clean production is a proactive production which is an integral approach and is listed in United Nations' environment program. In passive production, change meets with resistance and environmental requirement is considered costly. In active production, however, the environmental requirement is considered as activities that should be observed according to laws, regulations, and international protocols, etc. In proactive organization, environment is a priority subject of the enterprise and it is adopted and developed constantly by the employees.

Clean and sustainable production displays different characteristics according to the stage it is applied:

1. Productions that avoid toxic and hazardous raw materials and economize on energy, time, and labor are sustainable.

2. Productions that exclude hazardous material, that design with the least raw material and have the highest output are indicators of a clean and sustainable production.

3. Services including supply chain and in more extensive chain of values which do not pollute the environment, which are economical and which provide customer satisfaction are clean and sustainable.

4. In the marketing of clean and sustainable production of food, “green marketing” invented by American Marketing Association in 1975 is an example of contemporary ecologic and sustainable marketing. Accordingly, the products have to carry environmentalist tags on them.

The notion of green marketing cannot be restricted to marketing process but it can be reflected in all production processes. For instance, although at experimental level the marketing of solar powered cars, or cars that use hydrogen gas -obtained by electrolysis of water- as fuel, include all production processes and stages.

In line with green marketing, there are labeling types including “eco-labeling”, which symbolizes clean life cycle of the products; “disposable labels”, which define one aspect of products, and “negative labeling” which is a compulsory labeling type that shows negative sides of the product in terms of its supplied form instead of its claims.

Manufacturing enterprises bear all responsibilities of a sustainable production. According to Ottman what lies in the foundation of this understanding is “...a reliable product for the welfare and happiness of the community, advertisements that reflect reality, protective activities for the environment, safety of personnel, and efforts to provide employment.” The concept of reliable product leads to reliable production and brings to mind reliability of sustainability [15].

The notion of sustainability

Sustainability has emerged as a concept in 1970s together with the increase in raw material and energy sources and resulting upswing in environmental pollution. Global warming, rapid decreases in green areas of the world, rapid increase in human population, risk of draining all water resources, hunger, unemployment related to continual crises, social imbalances that could start crises in the world and similar reasons increase the importance of sustainability.

World Commission on Environment and Development (WCED) convened initially in 1984 and issued the Brundtland Report in the spring of 1987. The report defined “sustainable development” for the first time and expressed that humanity is able to persist in sustainable development [16].

At the United Nations Conference on Environment and Development (UNCED) held in Rio de Janeiro in 1992, the strategies expressed in Brundtland Report were further improved by the representatives of 179 countries and it focused on the protection of natural resources, sustainability for all forest varieties, and climate change. The conference resolved that the main reason behind the ongoing deterioration of natural environment was that production and consumption were realized with unsustainable models especially in developed countries. Accordingly, strategic decisions were considered such as taking preventive strategic decisions, using energy and resources in more efficient production processes, researching about and preferring cleaner manufacturing methods in all processes of product life cycle, and minimizing waste both during manufacture and after consumption of the products.

With the ‘White Paper’ issued by European Commission in 1994, a political infrastructure was formed for sustainable production with the title “Growth, competitiveness, employment: new formations and methods on our way to 21st century”. The significant information at the heart of this political infrastructure could be summarized as below: Raw materials should be used as efficiently as possible. Assembling techniques should be improved and recycling and reproduction capabilities should be supported. It is possible to recycle and reuse materials thanks to design measures to be taken during the planning of the product or the process. In the light of this information efficiency should be prioritized: efficiency should not be restricted to raw materials but it should cover all areas that have to do with time, money, and effort and should be reflected in the product functionality.

The ‘design measures’ mentioned in ‘White Paper’ emphasize the importance of sustainability of design. It is impossible to consider sustainability related to design on its own. Sustainability of design leads to considering the following:

- Sustainability of life and habitats,
- Sustainability of usage and consumption,
- Sustainability of production,

- Sustainability of design education. As areas of engineering are areas of design, their education is a part of the whole system.

Sustainable production is the prerequisite for sustainable design. The sustainable production principles established by LCSP (Lowell Center for Sustainable Production in USA) as their reason for establishment led to better acknowledgement and widespread practice of sustainability worldwide. Birdoğan, O'Brien, and Veleva et al. summarized in their respective studies the characteristic features of sustainable productions as below:

1. Environmental awareness should permeate the cultures of all organizations.
2. Sustainability should be given importance in all product and process designs of the enterprise.
3. Wastes and ecological impurities should be kept at a minimum during planning and implementation of production processes.
4. During product design, highest level of output should be considered, with minimum wastage of materials.
5. Modular design should be employed at a maximum in the entire manufacturing process.
6. Enterprises should be based on quality and efficiency, and goods and services should be manufactured with minimum input of resources.
7. They should improve the useful life of products by providing spare parts and means to reassemble [17-19].

There is a very comprehensive process and a chain of life cycle in the beginning and aftermath of a design project. In this context, it is initially compulsory to prepare safe surroundings and environment in terms of priority issues such as air, water, food, accommodation, etc. for sustainability of habitats and for preservation of future human habitat. In this issue, Birkeland's' definition of ecological scale unfold the designers' duties in a chained correlation which become more specialized from inside to outside:

- *"Bioregional Planning",* is an integral planning which include the holding capacity of regional, biologic life and ecologic systems, unique ecological features, shaping up lifestyles, production and management systems, etc.
- *"Urban Ecology",* second level from the outside, it represents the cities.
- *"Industrial Ecology",* mentions the economy of production processes and their environment protection efforts.
- *"Community Design",* points to the effects of development and settlements on ecologic balance.
- *"Construction Ecology",* describes economizing on materials in product structure and correct management of ecologic means.
- *"Eco-architecture",* ecologic designer should support designs that minimize operating effects of buildings with natural energies and develop human productivity.
- *"Ecodesign":* An eco-logical designer works in order to decrease the amount of toxic materials and energy amounts consumed up in the industry and households, ease demounting, and minimize waste caused by status-lover consumers through reusing and recycling [20].

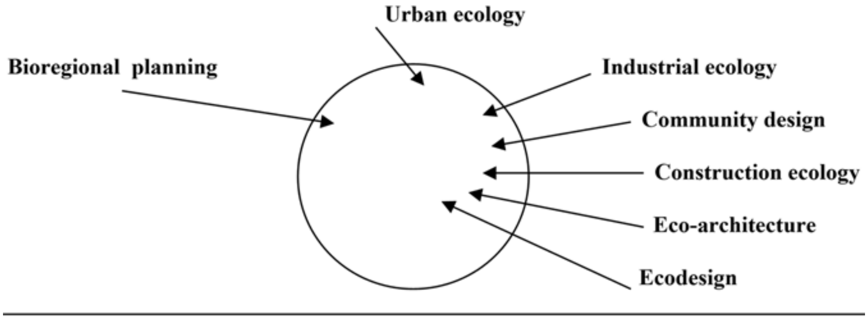

Figure 2. Ecological design areas exist in the whole of the scale [20].

Each of the areas in the ecologic design scale by Birkeland is related to all areas of life and practice. However, industrial ecology, construction ecology, and ecodesign are directly related to engineering fields.

Walker emphasizes that improvisations in design is possible by using the limited means at hand, and adds that there are few applicable a priori solutions and that a more sensitive type of design, and creativity should be encouraged. The source of such an approach is described as vernacular and local design because there is a perfect harmony among material values, beliefs, and ways of life of traditional cultures. The objects in these cultures have deep and symbolic meanings above and over their functional benefit:

> "We can learn from the craft and folk design traditions. However, we have to find ways to integrate the vernacular to the global in order to create designs that are suitable for modern communities developed in terms of technology and economy. This integration would be a progress for the industry in the closing of the profound gap between craft and design" [21].

Walker's proposal for the synthesis of the vernacular and the global, hints that the vernacular should be considered until the most ancient of fundamental values.

Comparison of sustainable design

It is not very easy to get used to the notion of sustainable design. For one thing, it is quite difficult to make design with sophisticated restrictions and without the definitions of designs we have learned, applied, and experienced until today. Nevertheless, now they will need designers' imagination, creativity, and innovation. The need for innovation have to be met by using the most advanced technologies, the least hazardous productions, the minimum amount of materials, catering for the local cultures and with awareness for social-environmental-economic responsibilities.

Table 1. Reshaping design: comparison of characteristic features [21]

Traditional Design	*Sustainable Design*
Industrial design	*Design of functional objects*
Product design	*Creation of material culture*
Specializing	*Improvisation*
Traditional	*Indefinite, indisposed*
Specific	*Integral, complementary*
Beneficial	*Unique*
Problem-solving	*Experimenting*
Solutions	*Possibilities*
A priori design	*Dependent design*

When comparing traditional design with sustainable design, Walker puts on the foreground the design of functional objects, which is already part of industrial product design. This leads us to the area of 'design engineering' and emphasizes the necessity that functional objects with minimum materials should directly interact with the users. It is suggested that sustainable design is dependent on environment, is integral and unique, it is experimenting while meeting spontaneous needs of people who became one with environment, and provides prospective life experience with future possibilities.

In line with this information, researchers of sustainability stress that future developments should be revised with the established values of the past, that communities put forward their material culture depending on their environment, and thus they underline the fact that historical beauties of the environment form the infrastructure of cultures in the scope of sustainable design.

Anatolian Mining and its reflections to our time in the context of fundamental values

Mining dates back to the most ancient times in Anatolia. It can be said that Anatolia is the homeland of mining. According to Sevin copper was molten at around 1200 °C in Değirmentepe on the banks of Euphrates at around

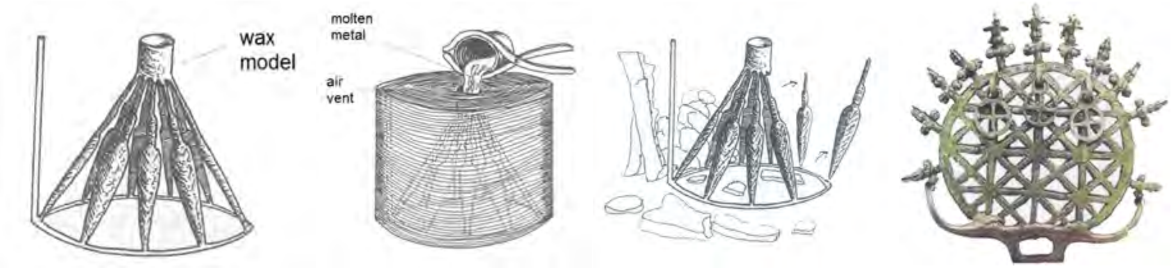

Figure 3. a) Second half of 3rd millennium B.C., vanishing wax method, wax model [22] b) Vanishing wax method, casting of molten metal, c) Vanishing wax method, cast product from bronze alloy cooled down, d) Old Bronze Era, Bronze "Sun Disk" found at Alacahöyük, 'BM' Mausoleum (2500 B.C.), It is thought to be produced with vanishing wax method. It is the symbol of Ankara University [23]. Used as the tip of ceremonial wand, the sun disk is thought to represent the "Sun God" [24].

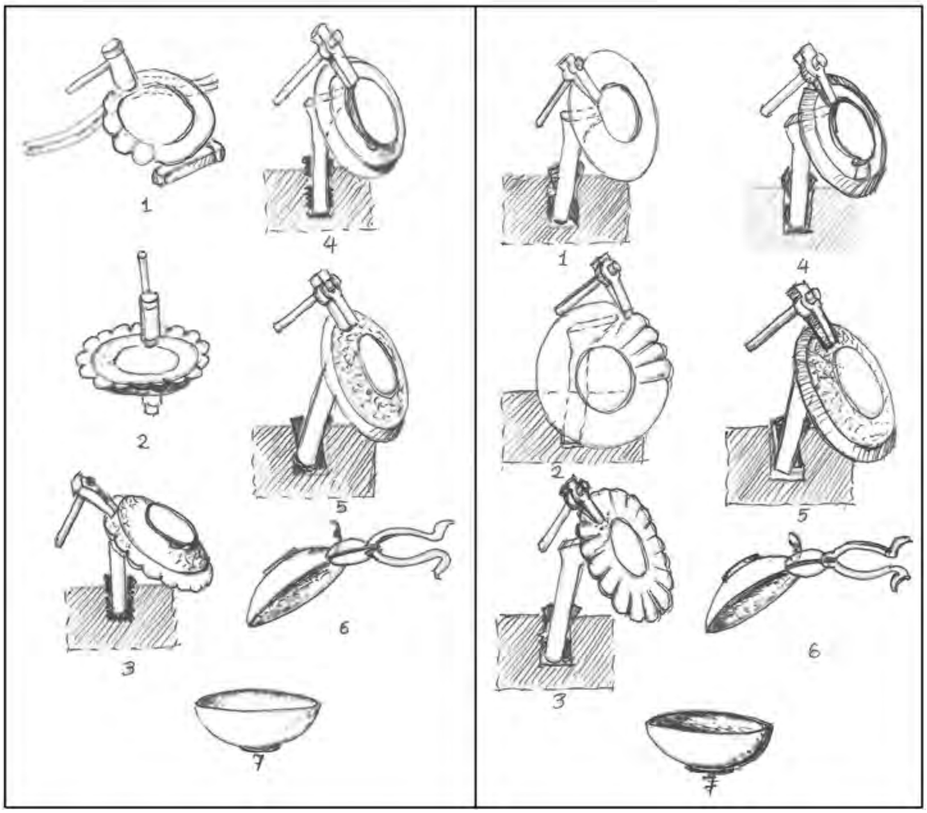

Figure 4. Metalworking techniques. The first group shows embossing partly with a free hand; the second group shows procedures with a supporting stand [26].

5th millennium B.C. Early Bronze Age saw the production of tools and arms at industrial levels, and local ateliers started to appear:

> “Dazzlingly artistic designs were made using sophisticated casting techniques by obtaining a bronze alloy by tossing either arsenic or tin into copper. In the second half of 3rd millennium B.C. a new technique emerged called “vanishing wax method” (cire perdue). In this method, initially a wax model was prepared and this was covered to make a mold. Heating the mold caused the wax to melt, and then liquid metal was poured in the mold. The mold was broken after it cooled down and the desired form was obtained. Sun disks at King’s mausoleums in Alacahöyük were cast using this technique.” [22]

Kuban also shows that techniques such as molding, embossing, soldering, and inlaying were developed around end of 3rd millennium B.C. Hattis, who lived in modern Kültepe region in Central Anatolia, are known to have kept up and mastered metal works starting with the initial period of 2000-1750 B.C. Coppersmith’s tradition which evolved in thousands of years in Anatolia (Figure 4) still uses embossing method [25]. Traditional method is ready in the mind of the coppersmith. An object of daily use (Figure 5) was obtained

Figure 5. Forming the copper tray with embossing method; the tray is completely made with traditional method. Design S.Satir, Production: Zülfikar Usta.

Figure 6. a) Tricycle to carry water demijohns, b) A manpowered vehicle to carry mail, c) Manpowered vehicle to sell flowers

after the method is transferred into an experimental and contemporary work with the collaboration of craftsman-designer.

What's more, 96.4% of Turkish economy is made up of SMEs and these enterprises usually own small ateliers where they make mostly crafting manufacture. With this viewpoint, and referring to 4th item of environment-friendly technologies in Yücel and Ekmekçiler [14], S. Satir covered the topic of handcrafted tools and vehicles made with semi-product materials in the lecture with undergraduate students at ITU-Industrial Product Design Department "Manpowered Vehicle Designs" seen in Figure 6 were realized. The materials suggested for these devsigns and their manufacture are ideal case analyses for the notion of sustainability.

The reason for the dense concentration of simple and plain products in culture-related fields is the solid structure of time-honored and ongoing traditions dating back to prehistoric periods. In this context, sustainability supports vernacular materials and production methods. If one most important aspect of sustainability is manufacturing with environment-friendly materials, other most significant facets include recycling vegetal waste with environmental concerns, and laboratory work in chemical industry, such as eliminating dyeing material from waste water in textile industry.

Laboratory work with environmental awareness

Engineers are important people in the development of their country: It is essential that besides what is contemporary, they have to observe the sustainability of natural and economic resources for healthy, secure and prosperous generations. Accordingly, it is an established fact that engineers have to be trained in environment and ethics besides a good quality technical training. Nevertheless, not enough environment and ethics classes could be incorporated in a formal education of four years.

With 2000s on, besides engineering standards, ABET added into its accreditation criteria for engineering faculties the requirement for students to prove their knowledge in economy, environment, sustainability, manufacturability, ethics, reliability, and social and political issues. It is emphasized that students should be helped to develop skills to analyze events and phenomena from historical and social viewpoints and generate ideas, and that approaches and practices that might limit their horizons in the narrow confines of the trade should be avoided.

Besides the classes related to environment, students could be assigned projects in order to provide them with environmental awareness. For instance, people have been eradicating forests to manufacture wood-based furniture,

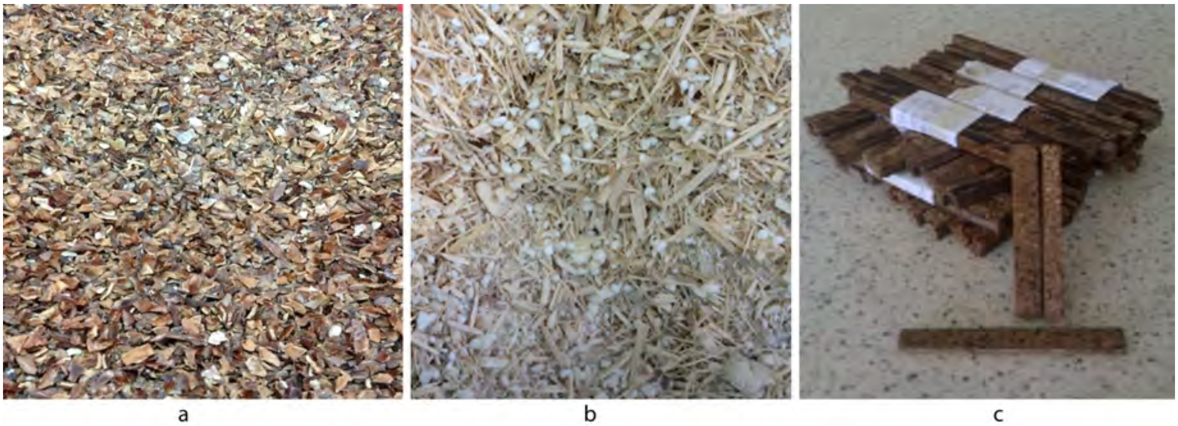

Figure 7. a) Waste walnut shells, b) Sunflower stalks, c) Composite material produced in the laboratory.

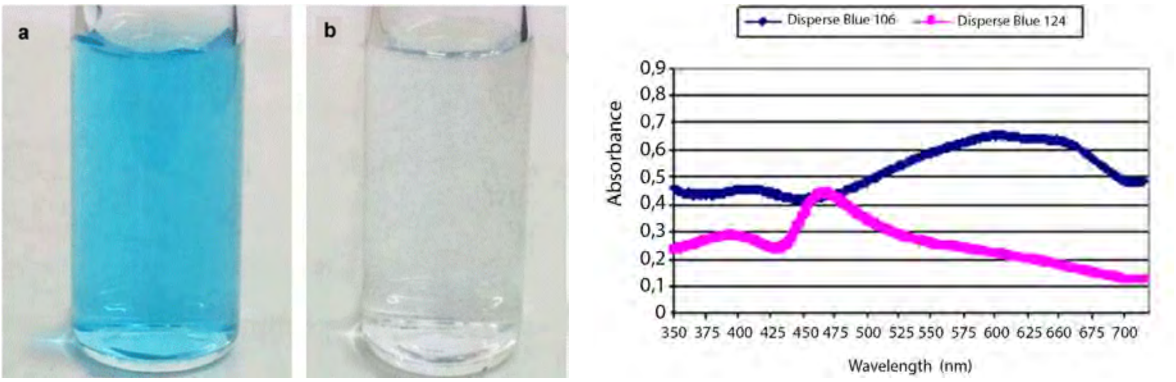

Figure 8. a) Before adsorption, b) After adsorption, c) The A-λ graph for disperse blue 106 and 124 [27]

construction and decoration materials. Although with the advancement of technology wood has been replaced in many sectors by materials such as plastic, metal, aluminum, concrete, and cement products, it is still preferred in the construction sector because of the warmth it adds to living environment. However, the decline in forests because of this reason and the difficulties in growing new ones in a timely manner to replace these trees make alternatives for wood more and more valuable. In this context, in order to minimize the risks to forests and to provide the wood texture and to evaluate waste material such as walnut shells, hazelnut shells, rice husks, sunflower stalks, and bagasse, students were assigned to prepare new composite material that is alternative to wood. Relative cheapness and availability of these filling materials for composites of this type make it cost- effective and make it possible to recycle waste material.

In the experiments, initially, walnut shells, hazelnut shells and sunflower stalks were obtained domestically, and ground to the required size. Waste materials (Figure 7a-b) were mixed with auxiliary material at varied rates according to prescribed recipes. Different homogenous mixtures were added phenol formaldehyde resin as binding agent. Hot press was applied to homogenous materials at 110°C at a pressure of 100 bars for 15 minutes. For pressing procedure predetermined optimum values for temperature, pressure, and time were used. Following the procedure the composite materials were cut with a compass saw to required size for analysis (Figure 7c). Pressed and resized samples were given standard tests for physical and mechanical strengths and checked for their suitability to use in various industrial sectors.

Another project assigned to engineering students besides theoretical classes in order to provide them with environmental awareness was adsorbing certain textile dyes and heavy metals from water using cheap waste material as adsorbents. The aim of this experiment was to provide students with environmental awareness by reusing waste material and concretize how worthless material could be commercially evaluated.

In this experiment, use of naturally available and cheap adsorbents such as walnut shells and hazelnut shells was tested in the disposal from waters of disperse blue 106 and disperse blue 124 pigments which are widely used in particularly textile industry to increase visual attractiveness. The effects of pH value, grain size and grain amount on the adsorption process in waters with different pigment concentrations were inspected. In the light of the findings (Figure 8) from experiments under different working conditions, it was seen that used waste material were effective in the disposal of pigments from waters.

In the disposal of disperse blue 106, 358 walnut shells were employed with an average grain size of 855 μm, while 855 hazelnut shells were employed with an average grain size of 1500 μm to dispose of disperse blue 124. The monoazo pigments of disperse blue 106 and 124 which were employed in the experiments were obtained from Sigma-Aldrich (Germany). The walnut and hazelnut shells used as adsorbents were domestically obtained and were subjected to resizing into grains and sieving before experiment.

CONCLUSIONS

This paper considers different fields of engineering with a holistic approach in the scope of sustainability with awareness for environment and fundamental time-honored values. Each engineering field has a rooted fundamental past. If this deep rooted past is evaluated with the history of the training country and its environment and the student is provided with awareness in this issue, the educational, historic, environmental, and social duties will be done. In the essence of this paper:

1. Hilda Taba's research [10] is dominated by concepts such as cultural change, interdependence, cooperation, contradiction and causality. Organizing the capacities of these key concepts and synthesizing information therein is of significant

importance. Hilda Taba's research symbolizes the fundamental past of engineering.

2. In Bonstingl's research [11], "Quality Model in Education" exhibits continuous learning and development. This spiral model allows for continuous auto-control and make it possible to evaluate ones past in a multidimensional way.

3. RIT's exemplary status in sustainable engineering education and its objectives cover almost all dimensions of environmental, social, economic, ethical, design concepts [12].

4. Yücel and Ekmekçiler [14] evaluated "old and traditional, environment-friendly technologies" in the scope of the subject matter.

5. Research by Birdoğan [17], Birkeland [20], Walker [21] supports the aim of this paper.

The supportive information in the literature review emphasize the significance of history and maintaining traditional fundamental values in the building up of environmental awareness. Similarly, the information that supports case studies was carefully selected. In this context:

Using local waste to preserve forests, or the experiment of treating pigmented water with hazelnut shells and sunflower stalks –a kind of waste-, to prevent contamination of water and land is very important dimension of the sustainability of engineering education.

Designing with semi-products and half machine half man power in small ateliers for future manufacture is again an utterly important design education experience. In this age of very sophisticated production technologies, it should not be very easy to support a semi-primitive production. However, in highly populated countries where the industry is mostly made up of SMEs, and high tech is scarce, supporting productions made with half-manpower will save energy.

At international level, RIT has a definite and ethical attitude in implementing sustainable engineering education. In Turkey, however, although environmental education is included in the curriculum as early as 1991, it still has the electives status. Therefore, for our country, it is not possible to talk about a standard training infrastructure or implementation at tertiary level in environmental issues at national level. It is essential that this training should not remain in theory but put into practice at an implementation phase which is adequate and is harmonious with course contents.

This is because institutions of higher education are responsible for training individuals who have knowledge, skills, and values necessary to contribute to the life quality of the global community.

REFERENCES

1. Erol GH, Gezer K. Teachers' Attitudes Toward Environment and Environmental Problems. International Journal of Environmental and Science Education 1(2006) 65–77.
2. Bakırcı H, Artun H. A Case Study Comparing Environmental Educational Policies of Different Countries. Electronic Journal of Social Sciences 10 (2011) 202–223.
3. İleri R. Çevre Eğitimi ve Katılımın Sağlanması. Ekoloji 28 (1998) 3–9.
4. Çolakoğlu E. Haklar Söyleminde Çevre Eğitiminin Yeri ve Türkiye'de Çevre Eğitiminin Anayasal Dayanakları. TBB Dergisi 88 (2010) 151–171.
5. Oğuz D, Çakcı I, Kavas S. Environmental Awareness of Students in Higher Education. SDU Faculty of Forestry Journal 12 (2011) 34–39.
6. Petersen RP. The Potential Role of Design in a Sustainable Engineering Profile. Paper presented at Conference on Engineering Education for Sustainable Development EESD13, University of Cambridge, UK, 23–24 September. E–Publishing Inc., UK, pp. 1–8, 2013.
7. http://ascelibrary.org/doi/abs/10.1061/40753%28171%29146 (25 June 2015, doi: 10.1061/40753(171)146).
8. Desha CJK, Hargroves KC, Smith MH, Stasinopoulos P. The Importance of Sustainability Engineering Education: A Toolkit of Information and Teaching Material. Paper presented at Engineering Training & Learning Conference, Griffith University, Australia, September. E–Publishing Inc., Australia, pp. 12–13, 2003.
9. Murphy CF, Allen D, Allenby B, Crittenden J, Davidson CI, Hendrickson C, Matthews HS. Sustainability in Engineering Education and Research at U.S. Universities. Environmental Science &Technology Feature 43 (2009) 5558–5564.
10. Fraenkel JR. Hilda Taba's Contributions to Social Studies Education, in Social Education. National Council for the Social Studies 56 (1992) 172–178.
11. Bonstingl JJ. Schools of Quality, second ed. Association for Supervision and Curriculum Development, Columbia–USA, 1996.
12. https://www.rit.edu/programs/sustainable–engineering–ms (25 June 2015).
13. On Environment. Foundation for Turkey Problematics, Ankara, June, pp.73, 1991.
14. Yücel M, Ekmekçiler ÜS. A Study About Environment–friendly Products: System of Clean Production, Eco–Label and Green Marketing. Electronic Journal of Social Sciences. 7 (2008) 320–333.
15. Ottman J. Green Marketing: Challenges and Opportunities for the New Marketing Age. İllinois: NTC Business Books, Lincolnwood, 1999.
16. http://www.mddelcc.gouv.qc.ca/developpement/voie_en.htm (25 June 2015).
17. Birdoğan B. Sustainable Production. Otomasyon Dergisi. 127 (2002).

18. O'Brien C. Sustainable production–a new paradigm for a new millennium. International Journal of Production Economics 60–61(1999) 1–7.
19. Veleva V, Hart M, Greiner T, Crumbley C. Indicators of Sustainable Production. Journal of Cleaner Production 9 (2001) 447–452.
20. Birkeland J. Design for Sustainability – A Sourcebook of Integrated Eco–logical Solutions. Earthscan Publishes, London, 2007.
21. Walker S. Sustainable by Design, Explorations in theory and Practice. Earthscan Publishes, London, 2007.
22. Sevin V. Ancient Anatolia and Thrace - From the Beginning to Persian Hegemony. İletişim Yayınları, İstanbul, 2003.
23. http://www.ankara.edu.tr/ (25 June 2015).
24. Baltacıoğlu H. Cultural Reflections, Ed. Betül Avunç, reprintTribute to Hayat Erkanal. Homer Yayınevi, İstanbul, 2006.
25. Kuban D. Main Lines of Turkish Art throughout History. Yapı Kredi Yayınları, Istanbul, 2004.
26. Barışta Ö. Turkish Handicrafts. Turkish Historical Society Press, Ankara, 1985.
27. Kaya N, Yücel T, Konkan A, Mocur D, Gültekin M. Disposal of Disperse Azo–dyes from Water Solutions by Using Walnut and Hazelnut Shells. Journal of Fac. Eng. Arch. Gazi Univ. 26 (2011) 509–514.

Hittite Journal of Science and Engineering, 2015, 2 (1) 115-125
ISSN NUMBER: 2149-2123
DOI: 10.17350/HJSE19030000017

A Second Degree Newton Method for an Inverse Scattering Problem for a Dielectric Cylinder

Ahmet Altundag
Istanbul Sabahattin Zaim University, Department of Mathematics Education, Istanbul, TURKEY

ABSTRACT

The inverse obstacle scattering problem we are interested is to reconstruct the image of an infinitely long homogeneous dielectric cylinder from the far field pattern for scattering of a time-harmonic E-polarized electromagnetic plane wave. We extend the approach suggested by Kress and Lee [18] that combines the ideas of Hettlich and Rundell [10] and Johansson and Sleeman [14] for the case of the inverse problem for a perfectly conducting scatterer to the case of penetrable scatterer. The inverse problem is depended on a system of non-linear boundary integral equations associated with a single layer approach to solve the direct scattering problem. We show the mathematical foundations of the method and illustrate its feasibility by numerical examples.

Key Words:
Helmholtz Equation; Inverse Scattering; Transmission Boundary Condition; Non-Linear Integral Equations; Gauss-Newton Iteration Methods; Single-Layer Approach.

Article History:
Received: 2015/05/17
Accepted: 2014/06/12
Online: 2015/07/01

***Correspondence to**: Ahmet Altundag, Istanbul Sabahattin Zaim University, Faculty of Engineering and Natural Sciences, Department of Mathematics Education, Istanbul, Turkey*
Tel: +90 (212) 692-9738
Fax: +90 (212) 693-8229
E-Mail: ahmet.altundag@izu.edu.tr

INTRODUCTION

Inverse scattering theory is concerned with methods for retrieving information on the geometry and the physical properties of obstacles from scattering of acoustic and electromagnetic wave. In the direct scattering problem the object is given and it is required to find the scattered wave. In the inverse scattering problem we want to receive information on geometry of the shape or physical parameters of the scattering object.

The inverse obstacle scattering problem that we currently deal with is considered for time-harmonic waves. The scattering object is assumed to be a homogeneous scatterer and the inverse problem is to reconstruct an image of the scatterer. In this manuscript we are interested in dielectric obstacles and restrict ourselves to the sufficiently long cylinders. This constrain provides us to reduce the inverse scattering problem into two dimensions.

Let simply connected bounded domain D be subset of IR^2 with C^2 boundary Γ. It illustrates the cross section of a sufficiently long dielectric cylinder and has constant wave number k_d with real and imaginary part larger than zero. k_0 and ν denote the exterior positive wave number and the outward unit normal to the boundary Γ. For a given one or several incident fields $v^i(x) = e^{ik_0\, x\cdot d}$ with incident direction d defined as a unit vector, for E –polarized electromagnetic waves the forward problem is assembled by the following Helmholtz equation with the transmission boundary condition: We look for solutions $v \in H^1_{\mathrm{loc}}(\mathrm{IR}^2 \setminus \bar{D})$ and $w \in H^1(D)$ to satisfy the Helmholtz equations

$$\Delta v + k_0^2 v = 0 \quad \text{in } \mathrm{IR}^2 \setminus \bar{\mathrm{D}}, \quad \Delta \mathrm{w} + \mathrm{k}_\mathrm{d}^2 \mathrm{w} = 0 \quad \text{in D} \tag{1.1}$$

fulfilling the transmission conditions

$$v = w, \quad \frac{\partial v}{\partial \nu} = \frac{\partial w}{\partial \nu} \quad \text{on } \Gamma \tag{1.2}$$

in the trace sense such that $v = v^i + v^s$. To ensure the scattered wave v^s vanishes at infinity, it requires to fulfil the following radiation condition

$$\lim_{r\to\infty} r^{1/2}\left(\frac{\partial v^s}{\partial r} - ik_0 v^s\right) = 0, \quad r = |x|. \tag{1.3}$$

It uniformly holds in all directions. The radiation condition can be rewritten as an asymptotic behaviour of the form

$$v^s(x) = \frac{e^{ik_0|x|}}{\sqrt{|x|}}\left\{v_\infty\left(\frac{x}{|x|}\right) + O\left(\frac{1}{|x|}\right)\right\}, \quad |x| \to \infty. \tag{1.4}$$

The v_∞ is an analytic function defined on the unit circle S^1 in IR^2 and is known far-field pattern of scattered field (see[8]).

The inverse obstacle scattering problem we are interested in is to reconstruct the boundary Γ of the scattering dielectric D by knowing v_∞ for one or several incident fields with different incident direction $d \in S^1$.

At this point we note that uniqueness results for this inverse transmission problem are only available for the case of infinitely many incident waves (see [15]). A general uniqueness result based on the far field pattern for one or finitely many incident waves is still lacking. More recently, a uniqueness result for recovering a dielectric disk from the far-field pattern for scattering of one incident field was established by Altundag and Kress [2].

For a more stable and accurate solution of the inverse transmission problem we extend the approach suggested by Kress and Lee [18] that combines the ideas of Hettlich and Rundell [10] and Johansson and Sleeman [14] from the case of the inverse problem for an object that is perfect conductor to the case of the inverse problem for an object that penetrates the incident field.

In order to transform the forward problem (1.1)–(1.3) to boundary integral equation, we represent the solution v^s and w to the direct scattering obstacle problem in terms of single-layer potential in $\mathrm{IR}^2 \setminus \bar{D}$ and in D with the densities ξ_0 and ξ_d, respectively. Approaching the boundary and using the jump relation and transmission boundary condition (1.2) we obtain a system of two boundary integral equations on the boundary Γ for the corresponding densities. We will denote this system of integral equations as a field equations. For the inverse obstacle scattering problem, the given far field pattern v_∞ and the required coincidence ofthe far field of the single-layer potential provides a further equation. In the sequel, we will denote this equation as a data equation. Field and data equation can be considered as three equations for three unknowns, i.e., boundary curve and the two densities. The system of boundary integral equations is non-linear with respect to the boundary and linear with respect to the two densities.This system of integral equations is ill-posed. The ill-posedness of the inverse problem is reflected through the ill-posedness of the data equation. This open up variety approaches to solve the inverse scattering obstacle problem by linearization and iteration. The first approach applied in [2]. The idea of the approach described as follows: Given an approximation Γ_{approx} for the boundary Γ in a first step the well-posed field equations can be solved for two densities on Γ_{approx}. Then in a second step, keeping the densities fixed, the ill-posed field equation can be linearised with respect to the boundary and the solution of the ill-posed linearised equation can be utilized to update the boundary approximation. Because of the ill-posedness the solution of this update equation requires stabilization. These two steps can be iterated until some suitable stopping criterion is satisfied. The second approach implemented in [3]. From the spirit of [20], the iteration scheme constructed as follows: Given an approximation Γ_{approx} for the boundary Γ and approximations $\xi_{d,approx}$, $\xi_{0,approx}$ for the densities ξ_d ,ξ_0 we linearize both the field and the data equations simultaneously with respect to the boundary curve and the two densities. The linear equations are then solved to update both the boundary curve and the two densities. Because of the ill-posedness the solution of the update equations requires stabilization, for example, by Tikhonov regularization. This procedure is then iterated until some suitable stopping criterion is achieved. In the current paper, the third approach is carried out. In the spirit of [10], [14] and [18], given an approximation Γ_{approx} for the boundary Γ in a first step the well-posed field equations can be solved for two densities on Γ_{approx}. Then in a second step, keeping the densities fixed, the ill-posed data equation can be linearised with respect to the boundary and we solve the linearised first degree data equation for a predictor. In a third step, keeping the densities fixed, we solve non-linear quadratic equation recursively for some steps to obtain a corrector. In a fourth step, we update the boundary approximation by $\Gamma_{\mathrm{approx}} + \mathtt{corrector}$ and continue this procedure until some suitable criteria is achieved. Because of the ill-posedness the solution of linearised data equation and quadratic equation require stabilization.

For a recent survey on the connections of the different approaches see Ivanyshyn, Kress and Serranho [12,13]. For related work for the Laplace equation we refer to Kress and Rundell [20] for the Dirichlet boundary condition and Eckel and Kress [9] Altundag and Kress [2,3] and Altundag [1,4] for the transmission condition and Altundag [5] for the transmision-impedance boundary condition. Finally, for a recent survey on the second degree Newton method see Hettlich and Rundell [10] Kress and Lee [18] Kress, Tezel and Yaman [22].

The scheme of the current manuscript is described as follows: In the second section we describe the solution of the forward problem via a single-layer potential approach as a base of our inverse algorithm. In the third section, we explain numerical solution of the forward algorithm. In the fourth section, the inverse algorithm is explained deeply. In the final section, we illustrate the feasibility of the method by demonstrating some numerical examples comparing the result with those for the Johansson and Sleeman method in [2], for the hybrid method in [4], and for the simultaneous linearization method in [3].

The forward problem

The forward problem (1.1)–(1.3) has at most one solution (see [7,19] for the three-dimensional case). Existence of a solution can be seen [7,19] for the three-dimensional case. The solution of the forward scattering problem is established in [2]. The forward scattering problem is solved via single-layer potential approach. The fundamental solution to the Helmholtz equation is given by

$$\Phi_k(x,y) := \frac{i}{4}\, H_0^{(1)}(k|x-y|), \quad x \neq y,$$

where k represents wave number and $H_0^{(1)}$ denotes the Hankel function of first kind and order zero. Using the notation of [8], in a Sobolev space setting, we introduce the single-layer potential operators

$$S_k : H^{-1/2}(\Gamma) \to H^{1/2}(\Gamma)$$

by

$$(S_k\xi)(x) := 2\int_\Gamma \Phi_k(x,y)\xi(y)\, ds(y), \quad x \in \Gamma, \tag{2.5}$$

and the normal derivative operators

$$K_k' : H^{-1/2}(\Gamma) \to H^{-1/2}(\Gamma)$$

by

$$(K_k'\xi)(x) := 2\int_\Gamma \frac{\partial \Phi_k(x,y)}{\partial \nu(x)}\, \xi(y)\, ds(y), \quad x \in \Gamma. \tag{2.6}$$

where $k = k_d$ and $k = k_0$. For the related mapping property, we cite to [17,23].

By using the jump relations on the boundary Γ, the single-layer potentials

$$\begin{aligned} w(x) &= \int_\Gamma \Phi_{k_d}(x,y)\xi_d(y)\, ds(y), \quad x \in D, \\ v^s(x) &= \int_\Gamma \Phi_{k_0}(x,y)\xi_0(y)\, ds(y), \quad x \in \mathrm{IR}^2 \setminus \bar{D}, \end{aligned} \tag{2.7}$$

solve the forward problem (1.1)–(1.3) provided the densities ξ_d and ξ_0 fulfil

$$\begin{aligned} S_{k_d}\xi_d - S_{k_0}\xi_0 &= 2v^i|_\Gamma, \\ \xi_d + \xi_0 + K_{k_d}'\xi_d - K_{k_0}'\xi_0 &= 2\left.\frac{\partial v^i}{\partial \nu}\right|_\Gamma. \end{aligned} \tag{2.8}$$

Provided k_0 is not a Dirichlet eigenvalue of the negative Laplacian for D, (2.7) has at most one solution. For the existence analysis and uniqueness of a solution, we refer to [2].

Numerical solution of the forward problem

To solve (2.8) numerically and present the inverse algorithm we assume the boundary curve Γ is defined by

$$\Gamma = \{\zeta(s) : 0 \leq s \leq 2\pi\}, \tag{3.1}$$

where ζ is a 2π–periodic and smooth function. By $\chi = \xi \circ \zeta$ representing the dependence of the operators on the boundary curve, we introduce the parametrized single-layer operator

$$\tilde{S}_k : H^{-1/2}[0,2\pi] \times C^2[0,2\pi] \to H^{1/2}[0,2\pi]$$

by

$$\tilde{S}_k(\chi,\zeta)(s) := \frac{i}{2}\int_0^{2\pi} H_0^{(1)}\,(k|\zeta(s)-\zeta(\tau)|)\,|\zeta'(\tau)|\,\chi(\tau)\,d\tau$$

and the parametrized normal derivative operators

$$\tilde{K}_k' : H^{-1/2}[0,2\pi] \times C^2[0,2\pi] \to H^{-1/2}[0,2\pi]$$

by

$$\tilde{K}_k'(\chi,\zeta)(s) := \frac{ik}{2}\int_0^{2\pi} \frac{[\zeta'(s)]^\perp \cdot [\zeta(\tau)-\zeta(s)]}{|\zeta'(s)|\,|\zeta(s)-\zeta(\tau)|}\,H_1^{(1)}(k|\zeta(s)-\zeta(\tau)|)\,|\zeta'(\tau)|\,\chi(\tau)\,d\tau$$

for $s \in [0,2\pi]$. We made use of $H_0^{(1)\prime} = -H_1^{(1)}$ and $b^\perp = (b_2,-b_1)$ for any vector $b = (b_1,b_2)$. The parameterized form of (2.8) has the representation as follows

$$\begin{aligned} \tilde{S}_{k_d}(\chi_d,\zeta) - \tilde{S}_{k_0}(\chi_0,\zeta) &= 2\,v^i \circ \zeta, \\ \chi_d + \chi_0 + \tilde{K}_{k_d}'(\chi_d,\zeta) - \tilde{K}_{k_0}'(\chi_0,\zeta) &= \frac{2}{|\zeta'|}\,[\zeta']^\perp \cdot \operatorname{grad} v^i \circ \zeta. \end{aligned} \tag{3.2}$$

The kernels

$$A(s,\tau) := \frac{i}{2}\,H_0^{(1)}(k|\zeta(s)-\zeta(\tau)|)\,|\zeta'(\tau)|$$

and

$$B(s,\tau) := \frac{ik}{2}\,\frac{[\zeta'(s)]^\perp \cdot [\zeta(\tau)-\zeta(s)]}{|\zeta'(s)|\,|\zeta(s)-\zeta(\tau)|}\,H_1^{(1)}(k|\zeta(s)-\zeta(\tau)|)\,|\zeta'(\tau)|$$

of the operators $\tilde{S}_k$ and $\tilde{K}_k'$ can be written in the form

$$\begin{aligned} A(s,\tau) &= A_1(s,\tau)\ln\left(4\sin^2\frac{s-\tau}{2}\right) + A_2(s,\tau), \\ B(s,\tau) &= B_1(s,\tau)\ln\left(4\sin^2\frac{s-\tau}{2}\right) + B_2(s,\tau), \end{aligned} \tag{3.3}$$

where

$$A_1(s,\tau):=-\frac{1}{2\pi}J_0(k|\zeta(s)-\zeta(\tau)|)|\zeta'(\tau)|,$$

$$A_2(s,\tau):=A(s,\tau)-A_1(s,\tau)\ln\left(4\sin^2\frac{s-\tau}{2}\right),$$

$$B_1(s,\tau):=-\frac{k}{2\pi}\frac{[\zeta'(s)]^{\perp}\cdot[\zeta(\tau)-\zeta(s)]}{|\zeta'(s)|\,|\zeta(s)-\zeta(\tau)|}J_1(k|\zeta(s)-\zeta(\tau)|)\,|\zeta'(\tau)|,$$

$$B_2(s,\tau):=B(s,\tau)-B_1(s,\tau)\ln\left(4\sin^2\frac{s-\tau}{2}\right).$$

J_0 and J_1 denote the Bessel functions of order zero and one respectively. The functions A_1, A_2, B_1, and B_2 turn out to be analytic with diagonal terms

$$A_2(s,s)=\left[\frac{i}{2}-\frac{C}{\pi}-\frac{1}{\pi}\ln\left(\frac{k}{2}|\zeta'(s)|\right)\right]|\zeta'(s)|$$

in terms of Euler's constant C and

$$B_2(s,s)=-\frac{1}{2\pi}\frac{[\zeta'(s)]^{\perp}\cdot\zeta''(s)}{|\zeta'(s)|^2}.$$

For the boundary integral equations with kernels of the form (3.3) a combined quadrature and collocation methods based on trigonometric interpolation, we refer to [8] or [21] and we also refer to [17] for the related error analysis.

To illustrate a numerical example, we examine the scattering of an incident field from a sufficiently long homogeneous dielectric cylinder. Its cross section consists of a non-convex kite-shaped and it is expressed by the parametric form

$$\zeta(s)=(\cos s+0.65\cos 2s-0.65, 1.5\sin s),\quad 0\le s\le 2\pi. \tag{3.4}$$

The far-field pattern of the single-layer potential v^s with density ξ_0 is given by

$$v_\infty(\hat{x})=\alpha\int_\Gamma e^{-ik_0\hat{x}\cdot y}\,\xi_0(y)\,ds(y),\quad \hat{x}\in S^1, \tag{3.5}$$

where

$$\alpha=\frac{e^{i\frac{\pi}{4}}}{\sqrt{8\pi k_0}}.$$

Table 1 illustrates some numerical result for the far field pattern $v_\infty(d)$ with respect to forward direction d and $v_\infty(-d)$ with respect to opposite direction $-d$. $d=(1,0)$ is chosen as a direction of incident field and the wave numbers are $k_0=1$ and $k_d=2+3i$.

The inverse problem

We progressed to explain an iterative scheme for solving the inverse obstacle scattering problem. We extend the inverse algorithm suggested by by Kress and Lee [18] that combines the ideas of Hettlich and Rundell [10] and Johansson and Sleeman [14] from the case of impenetrable scatterer to the case of penetrable scatterer. To do that it requires to introduce far-field operator of the form $S_\infty: H^{-1/2}(\Gamma)\to L^2(S^1)$ by

$$(S_\infty\xi)(\hat{x}):=\alpha\int_\Gamma e^{-ik_0\hat{x}\cdot y}\,\xi(y)\,ds(y),\quad \hat{x}\in S^1. \tag{4.1}$$

By considering the equations (2.7) and (3.5) we deduce that far-field pattern for the solution to forward problem

$$v_\infty=S_\infty\xi_0 \tag{4.2}$$

in terms of the solution to (2.8). Now, we can state the following theorem as a basis of inverse scattering problem.

Theorem 4.1. Assume that far-field pattern v_∞ and an incident plane wave v^i are given. Assume ξ_d and ξ_0, the boundary curve Γ fulfil the following equations

$$\begin{aligned} S_{k_d}\xi_d-S_{k_0}\xi_0 &= 2v^i, \\ \xi_d+\xi_0+K'_{k_d}\xi_d-K'_{k_0}\xi_0 &= 2\frac{\partial v^i}{\partial\nu}, \\ S_\infty\xi_0 &= v_\infty. \end{aligned} \tag{4.3}$$

Table 1. Approximate numerical value for the forward scattering problem

n	Real $[v_\infty(d)]$	Imag $[v_\infty(d)]$	Real $[v_\infty(-d)]$	Imag $[v_\infty(-d)]$
8	-0.6017247940	-0.0053550779	-0.2460323014	0.3184957768
16	-0.6018967551	-0.0056192337	-0.2461831740	0.3186052686
32	-0.6019018135	-0.0056277492	-0.2461946976	0.3186049949
64	-0.6019018076	-0.0056277397	-0.2461946846	0.3186049951

Then boundary curve Γ solves the inverse obstacle scattering problem.

The system of boundary integral equations (4.3) is linear with respect to the densities and non-linear with respect to the boundary curve Γ. What is more, it is ill-posed. The ill-posedness of the inverse problem is reflected through the ill-posedness of the third integral equation, the far field equation denoted as *data equation*. In the current paper, we are going to proceed as follows: Given a current approximation Γ_{approx} for Γ in a first step the well-posed *field equations* can be solved for two densities on Γ_{approx}. Then in a second step, keeping the densities fixed, the ill-posed *data equation* can be linearised with respect to the boundary curve and we solve the linearised first degree data equation for *a predictor*. In a third step, keeping the densities fixed, we solve non-linear quadratic equation recursively for some steps to obtain a *corrector*. In a fourth step, we update the boundary approximation by $\Gamma_{\text{approx}} + corrector$. To describe the procedure in more detail, we also require the parametrized version

$$\tilde{S}_\infty : H^{-1/2}[0,2\pi] \times C^2[0,2\pi] \to L^2(S^1)$$

of the far field operator as given by

$$\tilde{S}_\infty(\chi,\zeta)(\hat{x}) := \gamma \int_0^{2\pi} e^{-ik_0 \hat{x}\cdot\zeta(\tau)}\, |\zeta'(\tau)|\chi(\tau)\, d\tau, \quad \hat{x} \in S^1. \tag{4.4}$$

Then the parametrized form of (4.3) is transformed of the form

$$\begin{aligned} \tilde{S}_{k_d}(\chi_d,\zeta) - \tilde{S}_{k_0}(\chi_0,\zeta) &= 2\, v^i \circ \zeta, \\ \chi_d + \chi_0 + \tilde{K}'_{k_d}(\chi_d,\zeta) - \tilde{K}'_{k_0}(\chi_0,\zeta) &= \frac{2}{|\zeta'|}\, [\zeta']^\perp \cdot \operatorname{grad} v^i \circ \zeta, \\ \tilde{S}_\infty(\chi_0,\zeta) &= v_\infty. \end{aligned} \tag{4.5}$$

For a fixed χ the Fréchet derivative $\tilde{S}'_\infty$ of the operator $\tilde{S}_\infty$ with respect to the boundary curve ζ in the direction h_1 is given by

$$\tilde{S}'_\infty(\chi,\zeta;h_1)(\hat{x}) := \alpha \int_0^{2\pi} e^{-ik_0\hat{x}\cdot\zeta(\tau)} \left[-ik_0\, \hat{x}\cdot h_1(\tau)|\zeta'(\tau)| + \frac{\zeta'(\tau)\cdot h_1'(\tau)}{|\zeta'(\tau)|} \right] \chi(\tau)\, d\tau \tag{4.6}$$

for $\hat{x} \in S^1$. Then the linearization of the third equation in (4.5) at ζ with respect to the direction h_1 reads

$$\tilde{S}_\infty \chi_0 + \tilde{S}'_\infty(\chi_0,\zeta;h_1) = v_\infty. \tag{4.7}$$

(4.7) is a linear equation for the predictor h_1 but it is ill-posed. The ill-posedness is inherited from Fréchet derivative of the boundary.

For a fixed χ the Fréchet derivative $\tilde{S}''_\infty$ of the operator $\tilde{S}'_\infty$ with respect to the boundary curve ζ in the direction h_2 can be deduced of the form

$$\tilde{S}''_\infty(\chi,\zeta;h_1,h_2)(\hat{x}) := \alpha\int_0^{2\pi} e^{-ik_0\,\hat{x}\cdot\zeta(\tau)}\Big\{-k_0^2\,\hat{x}\cdot h_1(\tau)\,\hat{x}\cdot h_2(\tau)\;|\zeta'(\tau)|$$
$$-ik_0\,\hat{x}\cdot h_2(\tau)\frac{\zeta'(\tau)\cdot h_1'(\tau)}{|\zeta'(\tau)|} - ik_0\,\hat{x}\cdot h_1(\tau)\frac{\zeta'(\tau)\cdot h_2'(\tau)}{|\zeta'(\tau)|} \tag{4.8}$$
$$+\frac{h_1'(\tau)\cdot h_2'(\tau)}{|\zeta'(\tau)|} - \frac{\zeta'(\tau)\cdot h_1'(\tau)\;\zeta'(\tau)\cdot h_2'(\tau)}{|\zeta'(\tau)|^3}\Big\}\chi(\tau)d\tau.$$

Using the second degree approximation the equation (4.7) is replaced by the quadratic equation

$$S'_\infty(\chi,\zeta;h) + \frac{1}{2}S''_\infty(\chi,\zeta;h,h) = u_\infty - S_\infty(\chi,\zeta). \tag{4.9}$$

As in the inspire of Hettlich and Rundell [10], the nonlinear quadratic equation (4.9) is solved in two steps, namely a predictor and a corrector step. The predictor step coincides with the Johansson and Sleeman method [14]. For this step, we solve ill-posed linearized data equation (4.7) via Tikhonov regularization with Sobolev penalty term H^p and regularization parameter $\lambda_{1,n}$ to obtain a predictor h_1. After h_1 obtained , in the corrector step the ill-posed linear equation can be expressed as follows

$$S'_\infty(\chi,\zeta;h_{j+1}) + \frac{1}{2}S''_\infty(\chi,\zeta;h_{j+1},h_j) = v_\infty - S_\infty(\chi,\zeta). \tag{4.10}$$

Equation(4.10) is solved recursively for $h_{j+1}, j = 1,\dots,M$. Since equation(4.10) is ill-posed, it requires stabilization. We use Tikhonov regularization with Sobolev penalty term H^p and regularization parameter $\lambda_{2,n}$.

Now, we can describe the algorithm as follows: given an approximation for the boundary curve Γ with parametrization ζ, each iteration step of the proposed inverse algorithm consists of fourth parts.

1. We solve the first two well-posed equations of (4.5), i.e., the field equations for the densities χ_d and χ_0.
2. Keeping χ_0 fixed, we solve the ill-posed linearized data equation (4.7) for a predictor h_1. Since the kernels of the integral operators in (4.7) are smooth, for its numerical approximation the composite trapezoidal rule can be employed. Because of the ill-posedness the solution of (4.7) requires stabilization, for example, by Tikhonov regularization.
3. Keeping χ_0 fixed, we solve the linearized second degree equation (4.10) via Tikhonov regularization recursively in M steps to obtain the corrector $h = h_{M+1}$.
4. We update the boundary approximation by $\zeta + h$ and return to first step until some suitable criteria is achieved. The following stopping criterion is implemented and it is given by the relative error

$$\frac{\| v_{\infty;N} - v_\infty \|}{\| v_\infty \|} \le \epsilon(\delta) \tag{4.11}$$

where $v_{\infty;N}$ is the computed far field pattern for after N iteration steps and where $\epsilon(\delta) = \gamma\delta$, for noise level δ and $\gamma \approx 1$.

We represent the boundary parametrization of the form

$$\zeta(s) = p(s)\begin{pmatrix}\cos s\\ \sin s\end{pmatrix}, \quad 0 \le s \le 2\pi, \tag{4.12}$$

with a non-negative function p. The increments are of the form

$$h(s) = q(s)\begin{pmatrix}\cos s\\ \sin s\end{pmatrix}, \quad 0 \le s \le 2\pi, \tag{4.13}$$

with a real function q. For the approximation procedure, we assume that p and its update q have the form of a trigonometric polynomial of degree J,

$$q(s) = \sum_{j=0}^{J} a_j \cos js + \sum_{j=1}^{J} b_j \sin js. \tag{4.14}$$

The linearised equations (4.7) and (4.10) are solved in the least squares sense, penalized via Tikhonov regularization, for the unknown coefficients $a_0,\dots,a_J$ and $b_1,\dots,b_J$ of the trigonometric polynomial representing the update q. From the our numerical example, we observe that it is more advantageous to use an H^p Sobolev penalty term rather than an L^2 penalty term in the Tikhonov regularization.

We interpret the operators $\tilde{S}'_\infty$ and $\tilde{S}''_\infty$ as an ill-posed linear operator having the mapping properties of form

$$\tilde{S}'_\infty, \tilde{S}''_\infty : H^p[0,2\pi] \to L^2[0,2\pi] \tag{4.15}$$

for some small $p \in \mathrm{IN}$.

As a theoretical basis for the application of Tikhonov regularization we refer to [11]. Under the assumption of star-like boundaries, the operator $\tilde{S}'_\infty$ and $\tilde{S}''_\infty$ are injective if k_0^2 is not a Neumann eigenvalue for the negative Laplacian in D.

We also extend the above algorithm for finitely many incident plane waves. Let $v_1^i, \dots, v_R^i$ are R incident plane waves with different incident directions and $v_{\infty,1}, \dots, v_{\infty,R}$ be the corresponding far-field patterns for scattering from Γ. The inverse scattering problem is to reconstruct the unknown Γ. This is equivalent to solve

$$\begin{aligned} \tilde{S}_{k_d}(\chi_{d,r}, \zeta) - \tilde{S}_{k_0}(\chi_{0,r}, \zeta) &= 2\, v_r^i \circ \zeta, \\ \chi_{d,r} + \chi_{0,r} + \tilde{K}'_{k_d}(\chi_{d,r}, \zeta) - \tilde{K}'_{k_0}(\chi_{0,r}, \zeta) &= \frac{2}{|\zeta'|}\, [\zeta']^\perp \cdot \mathrm{grad}\; v_r^i \circ \zeta, \\ \tilde{S}_\infty(\chi_{0,r}, \zeta) &= v_{\infty,r}, \end{aligned} \tag{4.16}$$

for $r = 1, \dots, R$. The inverse algorithm can be described as follows: Given an approximation ζ, we firstly solve the first two equations in (4.16) for $r = 1, \dots, R$ to obtain $2R$ densities $\chi_{d,1}, \dots, \chi_{d,R}$ and $\chi_{0,1}, \dots, \chi_{0,R}$. Secondly, we solve the linearised equation

$$\tilde{S}_\infty \chi_{0,r} + \tilde{S}'_\infty(\chi_{0,r}, \zeta; h_1) = v_{\infty,r}, \quad r = 1, \dots, R, \tag{4.17}$$

for the predictor h_1 by interpreting them as one ill-posed equation with an operator from $H^p[0,2\pi] \mapsto (L^2[0,2\pi])^R$ and applying Tikhonov regularization. Thirdly we solve linearized second degree equation

$$S'_\infty(\chi_{0,r}, \zeta; h_{j+1}) + \frac{1}{2} S''_\infty(\chi_{0,r}, \zeta; h_{j+1}, h_j) = v_{\infty,r} - S_\infty(\chi_{0,r}, \zeta) \tag{4.18}$$

Numerical examples

As proof of concept rather than a documentation of a fully developed code, in this final section we present some numerical examples exhibiting the feasibility of our approach. In order to prevent an inverse crime, the synthetic far-field data were obtained by using the boundary integral equations based on a combined single- and double layer potential approach (see [7,19]). We use the numerical algorithm explained in [8,17,16] 64 quadrature points are used. The linearised data equation (4.7) and linearised second degree data equation (4.10) were solved by Tikhonov regularization with an H^2 penalty term, i.e., $p=2$ in (4.15). The regularized equation is solved by Nyström's method with the composite trapezoidal rule. The table 5.2 illustrates the types of contour given by corresponding representation formula.

In all our five examples we used R=8 as a number of incident waves with the directions d=(cos(2πr/R), sin(2πr/R), r=1,..., R and **J=10** as degree for the approximating trigonometric polynomials in (4.14) and M=10 as the number of recursion and the wave numbers k_o=1 and k_d=5 + 1i. The initial guess is given by the dotted line, the exact boundary curves are given by the dashed (blue) lines and the reconstructions by the full (red) lines. For simplicity, for the stopping rule we chose ε (σ) the same for all noise levels since this already gave satisfactory reconstructions. In according with the general convergence results on regularized Gauss–Newton method (see [6]) for the regularization parameters we used decreasing sequences

$$\lambda_{1,n} = \tau_1^{-n} \lambda_1, \qquad \lambda_{2,n} = \tau_2^{-n} \lambda_2$$

with λ_1, λ_2 positive and $\tau_1, \tau_2 > 1$ chosen by trial and error. The iteration numbers and the regularization parameters λ_1 and λ_2 for the Tikhonov regularization of (4.7) and (4.10), respectively, were chosen by trial and error. However, to illustrate the feasibility and stability of our method we used the same regularization parameter in all examples. These were chosen as $\lambda_1 = 0.9$, $\tau_1 = 1.2$ and $\lambda_2 = 0.8$, $\tau_2 = 1.36$.

Random errors are obtained by

$$\tilde{v}_\infty = v_\infty + \delta\eta \frac{||v_\infty||}{|\eta|} \tag{5.1}$$

Table 2. Boundary Curves

Types		*Representations*
Dropped-shaped	:	$\zeta(s)=\{(-0.5+0.75\sin\frac{s}{2},-0.75\sin s):s\in[0,2\pi]\}$
Apple-shaped	:	$\zeta(s)=\{\frac{0.5+0.4\cos s+0.1\sin 2s}{1+0.7\cos s}(\cos s,\sin s):s\in[0,2\pi]\}$
Kite-shaped	:	$\zeta(s)=\{(\cos s+1.3\overset{2}{\cos} s-1.3,1.5\sin s):s\in[0,2\pi]\}$
Peanut-shaped	:	$\zeta(s)=\{\sqrt{\overset{2}{\cos} s+0.25\sin s}\,(\cos s,\sin s):s\in[0,2\pi]\}$
Rounded triangle	:	$\zeta(s)=\{(2+0.3\cos 3s)(\cos s,\sin s):s\in[0,2\pi]\}$

with the random variable $\eta\in\mathbb{C}$ and $\{\mathrm{Re}\,\eta,\mathrm{Im}\,\eta\}\in(0,1)$.

In the first Figure 1, second Figure 2, third Figure 3, fourth Figure 4, and fifth Figure 5 examples illustrate reconstructions obtained after 13, 15, 15, 10, and 15 iterations respectively.

Table 3 illustrates the convergence behaviour of the proposed algorithm. The first column represents iteration number N and the other columns represent relative error determined by (4.11) for each contour 5.2.

Our examples clearly indicate the feasibility of the proposed algorithm with a reasonable stability against noise. From our further numerical experiments it is observed that using more than one incident wave improved on the accuracy of the reconstruction and the stability.

Furthermore, an appropriate initial guess is important to ensure numerical convergence of the iterations. Our examples also indicate that the proposed algorithm with the numerical reconstructions are superior to those obtained via by Johonsson and Sleeman method [14] in [2] to those obtained via by the hybrid method in [4]. Moreover, the proposed algorithm has as the same efficiency of accuracy and stability as the simultaneous linearization method in [3]. However, the proposed algorithm requires less computational effort than the simultaneous linearization method. Therefore, it is superior the simultaneous linearization method with respect to computational cost.

ACKNOWLEDGEMENTS

The author thanks Professor Rainer Kress for the discussion on the topic of this paper.

Table 3. Relative error at each iteration step

N	*Apple-Sh.*	*Dropped-Sh.*	*Kite-Sh.*	*Peanut-Sh.*	*R. Triangel*
1	0.6757221101	0.6360551737	0.6368500557	0.2148574440	0.8949045371
2	0.1643964696	0.1657433896	0.2976995503	0.0503726493	0.3733278852
3	0.0422092172	0.0281626370	0.1881878713	0.0067460381	0.2176997240
4	0.0142325900	0.0161566231	0.1346324897	0.0025621311	0.0940590296
5	0.0096240121	0.0137267005	0.1076783088	0.0024559183	0.0415419160
6	0.0081622629	0.0124983950	0.0910946349	0.0023434131	0.0205255193
7	0.0062161463	0.0114739054	0.0796446254	0.0022429730	0.0115610162
8	0.0043983846	0.0105610342	0.0710851110	0.0021531523	0.0078191797
9	0.0031519393	0.0098295139	0.0643294142	0.0020709805	0.0062761911
10	0.0024892871	0.0093579625	0.0587910366	0.0019941389	0.0055382041
11	0.0021832518	0.0091470771	0.0541263151	Terminated	0.0050712243
12	0.0020280692	0.0091156042	0.0501207838		0.0047028951
13	0.0019307739	0.0091655215	0.0466334592		0.0043807490
14	Terminated	0.0092326307	0.0435672694		0.0040879823
15		0.0092904674	0.0408523510		0.0038178513
16		Terminated	Terminated		Terminated

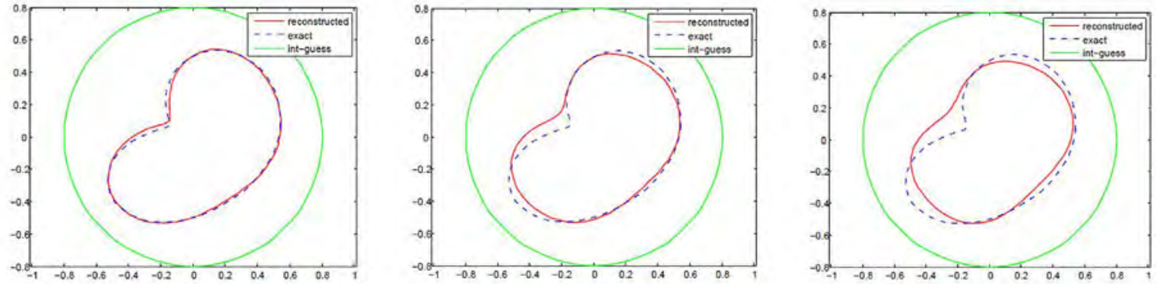

Figure 1. Reconstruction of the apple-shaped contour 5.2 for exact data (left), 3% noise (middle) and 5% noise (right)

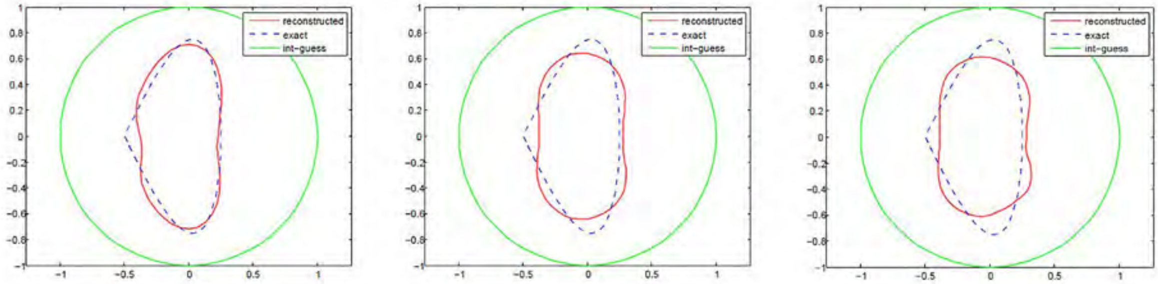

Figure 2. Reconstruction of dropped-shaped contour 5.2 for exact data (left), 3% noise (middle) and 5% noise (right)

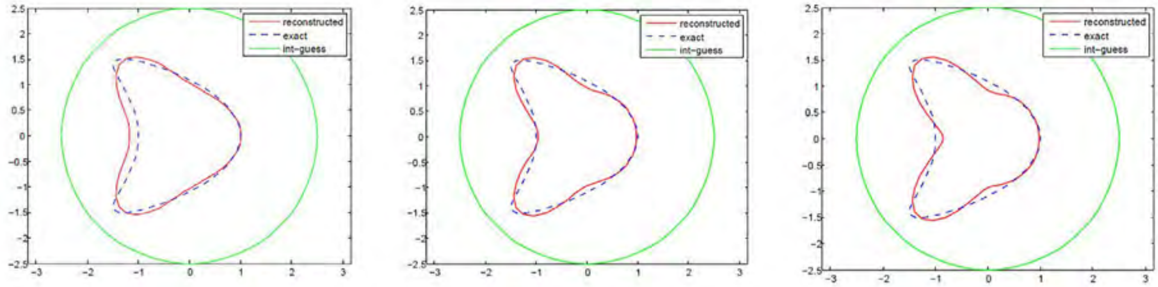

Figure 3. Reconstruction of kite-shaped contour 5.2 for exact data (left), 3% noise (middle) and 5% noise (right)

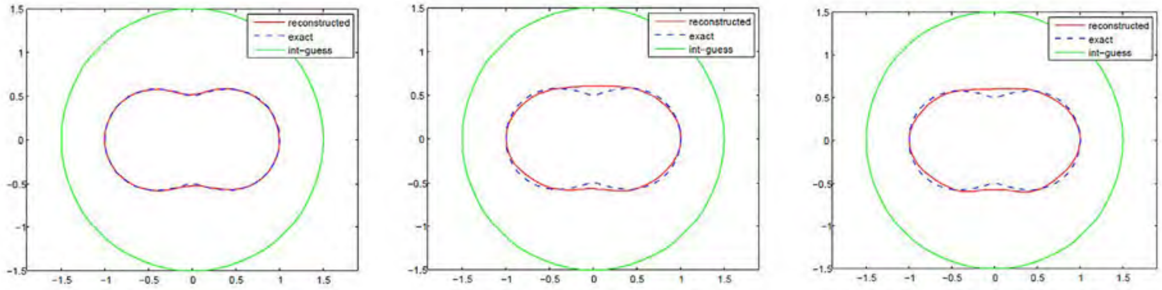

Figure 4. Reconstruction of peanut-shaped contour 5.2 for exact data (left), 3% noise (middle) and 5% noise (right)

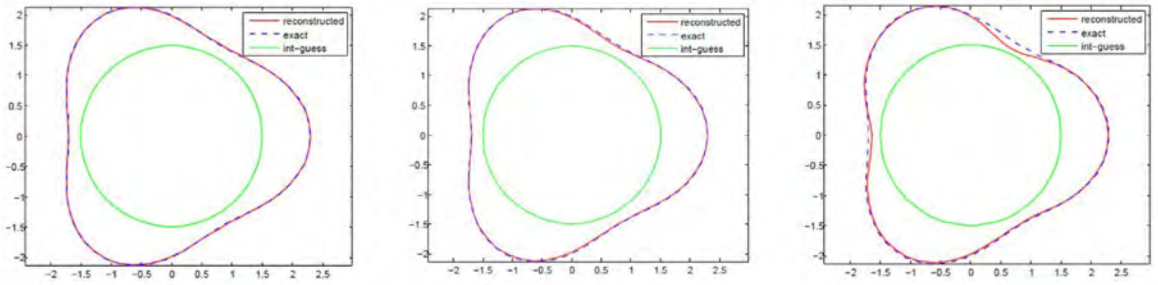

Figure 5. Reconstruction of rounded-triangle-shaped contour 5.2 for exact data (left), 3% noise (middle) and 5% noise (right)

REFERENCES

1. Altundag, A. : *On a two-dimensional inverse scattering problem for a dielectric*. Dissertation, Göttingen, February 2012.
2. Altundag, A. and Kress, R. : *On a two dimensional inverse scattering problem for a dielectric*. Applicable Analysis, , 757–771 (2012).
3. Altundag, A. and Kress, R.: *An Iterative Method for a Two-Dimensional Inverse Scattering Problem for a Dielectric*. Jour. On Inverse and Ill−Posed Problem , pp. 575–590 (2012).
4. Altundag, A. : *A hybrid method for inverse scattering problem for a dielectric*. Advances in Applied Mathematics and Approximation Theory, Springer, , pp. 185-203 (2013).
5. Altundag, A. : *Inverse obstacle scattering with conductive boundary condition for a coated dielectric cylinder*. J. Concrete And Applicable Mathematics, , pp. 11-22 (2015).
6. Burger, M., Kaltenbacher, B., and Neubauer, A. : *Iterative Solution Methods*. Handbook of Mathematical Methods in Imaging (Scherzer, ed.) Springer, Berlin 345–384 (2011).
7. Colton, D. and Kress, R.: *Integral Equation Methods in Scattering Theory*. Wiley−Interscience Publications, New York 1983.
8. Colton, D. and Kress, R.: *Inverse Acoustic and Electromagnetic Scattering Theory*. 2nd. ed. Springer, Berlin 1998.
9. Eckel, H. and Kress, R.: *Non-linear integral equations for the inverse electrical impedance problem*. Inverse Problems , 475–491 (2007).
10. Hettlich, F. and Rundell, W.: *A second degree method for non-linear inverse problem*. SIAM J. Numer. Anal. , 587–620 (2000).
11. Ivanyshyn, O. and Johansson, T.: Boundary integral equations for acoustical inverse sound−soft scattering. J. Inverse Ill−Posed Probl. , 1-14 (2007).
12. Ivanyshyn, O. and Kress, R.: Non−linear integral equations in inverse obstacle scattering. In: *Mathematical Methods in Scattering Theory and Biomedical Engineering* (Fotiatis, Massalas, eds). World Scientific, Singapore, 39−50 (2006).
13. Ivanyshyn, O., Kress, R. and Serranho, R.: Huygens' principle and iterative methods in inverse obstacle scattering. Advances in Computational Mathematics , 413–429 (2010).
14. Johansson, T. and Sleeman, B.: Reconstruction of an acoustically sound−soft obstacle from one incident field and the far−field pattern. IMA Jour. Appl. Math. , 96-112 (2007).
15. Kirsch, A. and Kress, R.: Uniqueness in inverse obstacle scattering. Inverse Problems , 285–299 (1993).
16. Kress, R.: On the numerical solution of a hypersingular integral equation in scattering theory. J. Comp. Appl. Math., 345–360 (1995).
17. Kress, R.: *Integral Equations*. 2nd. ed Springer Verlag, Berlin 1998.
18. Kress, R. and Lee, K.M. : *A second degree Newton method for an inverse obstacle scattering problem* J. Comp. Phys. 7661–7669 (2011).
19. Kress, R. and Roach, G.F.: Transmission problems for the Helmholtz equation. J. Math. Phys. , 1433-1437 (1978) .
20. Kress, R. and Rundell, W.: Non−linear integral equations and the iterative solution for an inverse boundary value problem. Inverse Problems , 1207-1223 (2005).
21. Kress, R. and Sloan, I.H.: On the numerical solution of a logarithmic integral equation of the first kind for the Helmholtz equation. Numerische Mathematik , 199–214 (1993).
22. Kress, R., Tezel, N., and Yaman, F. : A second order Newton Method for sound soft inverse obstacle scattering. J. Inverse and Ill−posed Problems , 173–185 (2009).
23. McLean, W.: Strongly Elliptic Systems and Boundary Integral Equations. Cambridge University Press 2000.

NATIONAL & INTERNATIONAL SCIENTIFIC EVENTS

2016 International Conference on Mechanical, Manufacturing, Modeling and Mechatronics (IC4M 2016)
Venue: Le Meridien Kuala Lumpur
Location: Kuala Lumpur, Malaysia

BEGINS: Feb 27, 2016 09:00 AM
Ends: Feb 29, 2016 05:00 PM

6th International Chemical and Environmental Engineering Conference

Venue: Hotel Royal
Location: Kuala Lumpur, Malaysia

BEGINS: Dec 27, 2015 08:00 AM
Ends: Dec 29, 2015 12:00 PM

Sixth Nanoscience and Nanotechnology Symposium (NNS 2015)
Venue: The Sunan Hotel Solo
Location: Solo, Indonesia

BEGINS: Nov 04, 2015 08:00 AM
Ends: Nov 05, 2015

Experimental Fluid Mechanics 2015

Venue: Kaiserstein Palace
Location: Prague, Czech Republic

BEGINS: Nov 17, 2015 05:00 PM
Ends: Nov 20, 2015 02:00 PM

International Conference on Structural Engineering, New Technology and Methods (ICSENM'16)
Venue: Clarion Congress Hotel Prague
Location: Prague, Czech Republic

BEGINS: Mar 30, 2016
Ends: Mar 31, 2016

Third International Conference on Mechanical Engineering (Meche-2015)

Venue: Dubai,UAE
Location: Dubai,, United Arab Emirates

BEGINS: Nov 06, 2015 08:00 AM
Ends: Nov 07, 2015 06:00 PM

Sixth International Conference on Metals in Genetics, Chemical Biology and Therapeutics (ICMG-2016)
Venue: Indian Institute of Science
Location: Bangalore, Karnataka, India

BEGINS: Feb 17, 2016 09:00 AM
Ends: Feb 20, 2016 04:00 PM

Interflam 2016

Venue: Royal Holloway College, Univ. of London
Location: Egham, Nr Windsor, Surrey, UK

BEGINS: Jul 04, 2016 09:00 AM
Ends: Jul 06, 2016 05:00 PM

Biotechnology for Better Tomorrow

Venue: DT by Hilton Tampa Airport Westshore
Location: tampa, Florida, United States

BEGINS: Oct 28, 2015
Ends: Oct 31, 2015

Second International Conference on Electrical and Electronics Engineering (ELEL 2015)

Venue: Dubai,UAE
Location: Dubai,, United Arab Emirates

BEGINS: Nov 06, 2015 08:00 AM
Ends: Nov 07, 2015 06:00 PM

ASME 2015 International Mechanical Engineering Congress Exposition
Venue: George R Brown Convention Center
Location: Houston, Texas, United States

BEGINS: Nov 13, 2015
Ends: Nov 19, 2015

3rd International Conference on Rehabilitation and Maintenance in Civil Engineering
Venue: Sahid Jaya Hotel
Location: Solo, Indonesia

BEGINS: Nov 19, 2015
Ends: Nov 21, 2015
